



January 10, 2003

## An International Muon Ionization Cooling Experiment (MICE)

### Abstract

A Neutrino Factory based on a muon storage ring is the ultimate tool for studies of neutrino oscillations, including possibly the discovery of leptonic CP violation. It is also the first step towards a  $\mu^+\mu^-$  collider. Ionization cooling of muons has never been demonstrated in practise but has been shown by end-to-end simulation and design studies to be an important factor both for the performance and for the cost of a Neutrino Factory. This motivates an international programme of R&D, including an experimental demonstration. The aims of the international Muon Ionization Cooling Experiment proposed in this document are:

- To show that it is possible to design, engineer and build a section of cooling channel capable of giving the desired performance for a Neutrino Factory;
- To place it in a muon beam and measure its performance in various modes of operation and beam conditions, thereby investigating the limits and practicality of cooling.

The MICE collaboration have designed an experiment in which a section of an ionization cooling channel is exposed to a muon beam. This cooling channel assembles liquid-hydrogen absorbers providing energy loss and high-gradient radio frequency (RF) cavities to re-accelerate the particles, all tightly contained in a magnetic channel. It reduces the beam transverse emittance by  $>10\%$  for muon momenta between 140 and 240 MeV/c. Spectrometers placed before and after the cooling section perform the measurements of beam transmission and emittance reduction with an absolute precision of  $\pm 0.1\%$ .

This proposal describes the principle of the measurements, the experimental set-up, the beam and infrastructure requirements and the proposed schedule and estimated cost for the experiment. New evaluations of the effect of possible backgrounds on the detectors due to radiation from the RF cavities show that the desired precision can be confidently achieved.

It is proposed to carry out the experiment at RAL. A scenario is proposed to satisfy the safety requirements related to the use of liquid hydrogen as cooling medium. A cost estimate is presented together with a number of possible cost reductions. Assuming proper funding and support, ionization cooling of muons will be demonstrated by 2007.



# The MICE Collaboration

G. Gregoire, G. Ryckewaert  
Institute of Physics and Cyclotron Research Center  
Universite Catholique de Louvain B-1348-Louvain-la-Neuve, Belgium

L. Chevalier, J.-M.Rey  
DAPNIA, CEA/Saclay, France

M. G. Catanesi, E. Radicioni  
INFN Bari, Italy

M. Castellano, M. Migliorati, C. Vaccarezza  
INFN Laboratori Nazionali di Frascati, Italy

P. Fabbriatore, S. Farinon, R. Musenich  
INFN Genova, via Dodecaneso 33, 16146 Genova, Italy

U. Gastaldi  
INFN, Laboratori Nazionali di Legnaro, Via Romea 4, I-35020 Legnaro (Pd), Italy

D. Batani, M. Bonesini, A. DeMin, F. Ferri, F. Paleari  
INFN Milano, Dipartimento di Fisica G. Occhialini Piazza Scienza 3, 20126 Milano, Italy

F. Ambrosino, D. Campana, G. Osteria, V. Palladino, G. Saracino  
INFN Napoli e Università Federico II, Napoli, Italy

D. Gibin, A. Guglielmi, M. Laveder, M. Mezzetto  
INFN Padova, Dipartimento di Fisica Galileo Galilei, Via Marzolo 8, 35131 Padova, Italy

D. Orestano, F. Pastore, A. Tonazzo, L. Tortora  
INFN Roma III and Physics Department of ROMA TRE University,  
Via della Vasca Navale 84, I-00146 Roma, Italy

M. Apollonio, G. Giannini, P. Chimenti  
University of Trieste and INFN, Trieste, Italy

S. Ishimoto, S. Suzuki, K. Yoshimura  
High Energy Accelerator Research Organization (KEK),  
Institute of Particle and Nuclear Studies, Tsukuba, Ibaraki, Japan

M. Aoki, Y. Kuno, A. Sato  
Osaka University, Graduate School of Science, Department of Physics,  
Toyonaka, Osaka, Japan

S. de Jong<sup>\*</sup>, F. Filthaut<sup>\*</sup>, F. Linde<sup>♦</sup>  
NIKHEF, Amsterdam, The Netherlands

N. Mezentsev, G. Silvestrov, A. N. Skrinsky  
Budker Institute of Nuclear Physics, Novosibirsk, Russian Federation

P. Gruber, H. Haseroth, F. Sauli  
CERN, Geneva, Switzerland

A. Blondel, M. Campanelli, A. Cervera, S. Gilardoni, V. Grichine<sup>♠</sup>, L. Malgeri  
DPNC, Section de Physique, Université de Genève, Switzerland

---

<sup>\*</sup> also at Katholieke Universiteit Nijmegen, the Netherlands

<sup>♦</sup> also at Universiteit van Amsterdam, the Netherlands

<sup>♠</sup> also at Lebedev Institute, Moscow, Russian Federation

M. Felcini, A. Rubbia  
Institute for Particle Physics, ETH-Zürich, Switzerland

C. Petitjean  
Paul Scherrer Institut, CH 5232 Villigen PSI, Switzerland

P. Kyberd  
Brunel University, Uxbridge, Middlesex UB8 3PH, United Kingdom

A. Khan, A. Walker  
School of Physics, University of Edinburgh, James Clerk Maxwell Building,  
Mayfield Road, Edinburgh EH9 3JZ, UK

F. J. P. Soler<sup>♥</sup>  
Department of Physics and Astronomy, Kelvin Building, The University of  
Glasgow, Glasgow, G12 8QQ, UK

P. Cooke, J. B. Dainton, J. R. Fry, R. Gamet, Ch. Touramanis  
Department of Physics, University of Liverpool, Oxford St, Liverpool L69 7ZE, UK

G. Barber, P. Dornan, K. Long, E. McKigney, D. R. Price, J. Sedgbeer  
Imperial College of Science, Technology and Medicine, Prince Consort Road,  
London SW7 2BW, UK

W. W. M. Allison, G. Barr, J. Cobb, S. Cooper, S. Holmes, H. Jones, W. Lau, H. Witte, S. Yang  
Department of Physics, University of Oxford, Denys Wilkinson Building, Keble Road, Oxford OX1  
3RH, UK

D. E. Baynham, D. Bellenger, T. W. Bradshaw, R. Church, P. Drumm, R. Edgecock, M. Ellis,  
I. Gardner, I. M. Ivaniouchenkov, A. Jones, H. Jones, R. Mannix, A. Morris, W. J. Murray,  
P. R. Norton, J. H. Rochford, K. Tilley, A. Weber  
CCLRC Rutherford Appleton Laboratory, Chilton, Didcot, Oxfordshire, OX11 0QX, UK

C. N. Booth, P. Hodgson  
Department of Physics and Astronomy, University of Sheffield, Sheffield S3 7RH, UK

J. Norem  
Argonne National Laboratory, 9700 S. Cass Avenue, Argonne, IL 60439, USA

R. B. Palmer, R. Fernow, S. Kahn, J. Gallardo, H. Kirk  
Brookhaven National Laboratory, Upton, NY 11973-5000, USA

D.R. Winn  
Fairfield University, 1073 North Benson Road, Fairfield, CT 06824, USA

K. Hoffman, M. Oreglia  
University of Chicago and Enrico Fermi Institute, 5640 S. Ellis Ave., Chicago, IL 60637-1433, USA

A. D. Bross, S. Geer, D. Neuffer, A. Moretti, M. Popovic, R. Raja, R. Stefanski, Z. Qian  
Fermilab, P.O. Box 500, Batavia, IL 60510-0500, USA

E. L. Black, D. M. Kaplan, T. J. Roberts, N. Solomey, Y. Torun  
Illinois Institute of Technology, 3101 S. Dearborn St., Chicago, IL 60616, USA

R. A. Rimmer  
Jefferson Lab, 12000 Jefferson Avenue, Newport News, VA 23606, USA

---

<sup>♥</sup> also at RAL

M. A. Green, D. Li, M. S. Zisman  
Lawrence Berkeley National Laboratory, Berkeley, CA 94720, USA

D. Cline, K. Lee, Y. Fukui, X. Yang,  
UCLA Physics Department, Los Angeles, CA 90024, USA

M. A. C. Cummings, D. Kubik  
Northern Illinois University, DeKalb, IL 60115, USA

Y. Onel  
University of Iowa, Iowa City, IA52242, USA.

S. B. Bracker, L. M. Cremaldi, R. Godang, D. J. Summers  
University of Mississippi, MS 38677, USA

G. G. Hanson, A. Klier,  
University of California, Riverside, Riverside, CA 92521-0413 USA

## **Acknowledgements**

We wish to acknowledge the essential contributions in the conceptual development of a muon cooling experiment made by our CERN colleagues, in particular R. Garoby, K. Hanke, E. B. Holzer, P. Janot, A. Lombardi and M. Vretenar.

# International Muon Ionization Cooling Experiment (MICE)

## Organization

### Steering committee:

A. Blondel\*<sup>1</sup> (Geneva)  
H. Haseroth (CERN)  
R. Edgecock (RAL)  
I. Ivaniouchenkov (RAL)<sup>3</sup>  
Y. Kuno (Osaka)  
S. Geer (FNAL)  
D. M. Kaplan<sup>2</sup> (IIT)  
M. S. Zisman (LBNL)  
Y. Torun<sup>4</sup> (IIT)

\*convener, <sup>1</sup>EU spokesperson, <sup>2</sup>U.S. spokesperson, <sup>3</sup>interim project engineer, <sup>4</sup>secretary

### Conveners of technical teams:

**Concept development:** R. B. Palmer (BNL)

**Experiment simulations:** M. G. Catanesi (Bari), Y. Torun (IIT)

**Hydrogen absorbers:** S. Ishimoto (KEK), M. A. C. Cummings (Northern Illinois)

**RF cavities, power sources:** D. Li (LBNL), R. Church (RAL), H. Haseroth (CERN)

**Magnetic system:** M. A. Green (LBNL), J.-M. Rey (CEA Saclay)

**Particle detectors:** V. Palladino (Napoli), A. Bross (FNAL)

**Beam line:** P. Drumm (RAL)

**RF radiation:** J. Norem (Argonne), E. McKigney (IC London)

**Engineering and integration:** I. Ivaniouchenkov (RAL), E. L. Black (IIT)

# Table of Contents

<b>1</b>	<b>General Motivation.....</b>	<b>10</b>
1.1	Introduction .....	10
1.2	Physics at a Neutrino Factory .....	12
1.3	Neutrino Factory accelerator complex.....	18
<b>2</b>	<b>Cooling.....</b>	<b>21</b>
2.1	Principle of ionization cooling.....	21
2.2	Cooling channel design.....	23
2.3	Other absorber materials.....	25
2.4	Possible extensions (gas cooling and ring coolers) .....	26
<b>3</b>	<b>The International Muon Ionization Cooling Experiment .....</b>	<b>28</b>
3.1	Layout of the experiment.....	28
3.2	Beam dynamics and quantities to be measured .....	30
3.3	Measurement technique .....	34
3.4	Simulations of the measurement precision .....	36
3.5	Possible experiments and time development of the apparatus.....	40
<b>4</b>	<b>The Magnetic Channel .....</b>	<b>43</b>
4.1	Layout and optics.....	43
4.2	Design of coils .....	44
4.3	Cryogenic services to the magnet and absorber.....	48
4.4	Magnetic measurements .....	52
4.5	Responsibilities, costs and time line .....	54
<b>5</b>	<b>The RF System .....</b>	<b>56</b>
5.1	Introduction .....	56
5.2	The cavity geometry .....	57
5.3	Terminations of the beam iris.....	57
5.4	RF and thermal analysis.....	60
5.5	Vacuum requirements.....	60
5.6	Cavity cooling.....	61
5.7	RF coupler .....	61
5.8	Cavity tuning requirements.....	62
5.9	Cavity integration .....	62
5.10	Cavity performance .....	63
5.11	RF transmitters .....	64
5.12	RF distribution system.....	64
5.13	RF control system.....	65

<b>6</b>	<b>LH<sub>2</sub> Absorbers</b> .....	<b>67</b>
6.1	General design .....	67
6.2	Windows.....	68
6.3	Thermal design .....	70
6.4	Responsibilities, costs and timelines .....	71
<b>7</b>	<b>Beam and Beam Line</b> .....	<b>73</b>
7.1	Layout and location .....	73
7.2	Expected performance and time structure .....	74
7.3	Time line.....	77
7.4	Interference with ISIS.....	77
<b>8</b>	<b>Detectors</b> .....	<b>78</b>
8.1	Overall description, functionality and redundancy.....	78
8.2	Scintillators for timing, trigger and upstream PID .....	78
8.3	Upstream PID Cherenkov.....	80
8.4	Tracking detectors .....	80
8.5	Downstream PID (e- $\mu$ separation).....	88
8.6	The electromagnetic calorimeter .....	89
8.7	The downstream Cherenkov e/ $\mu$ separator .....	92
8.8	DAQ, trigger, on-line monitoring.....	95
8.9	Conclusions .....	97
<b>9</b>	<b>Effects of Radiation on Detectors</b> .....	<b>98</b>
9.1	General understanding and characteristics .....	98
9.2	Measurement results .....	99
9.3	Projected effect on MICE tracker performance.....	103
9.4	Programme of further measurements.....	104
<b>10</b>	<b>Implementation of MICE at RAL and Engineering Integration</b> .....	<b>106</b>
10.1	Hall layout .....	106
10.2	Infrastructure and services .....	108
10.3	Safety .....	109
10.4	Engineering and installation plans .....	114
10.5	Costs and time-line of MICE installation at RAL .....	120
<b>11</b>	<b>Summary of Responsibilities, Costs, Funding and Schedule</b> .....	<b>122</b>
11.1	Cost.....	122
11.2	Schedule.....	126
<b>12</b>	<b>Summary and Conclusions</b> .....	<b>129</b>
	<b>References</b> .....	<b>132</b>



# 1 General Motivation

## 1.1 Introduction

Muon accelerators have received increasing attention in the past 10 years. In particular, with the observations of flavour oscillations of atmospheric neutrinos [Fukuda98], a Neutrino Factory based on a high-energy muon storage-ring [Geer98, Aut99] became the object of great interest as the ultimate tool to study the neutrino mixing matrix [Albright00, Apollonio02, Lindner02]. Recent results on neutrinos from the sun [SNO01, SNO02] and from nuclear reactors [KamLAND02] establish the Neutrino Factory as the best facility to discover, and study precisely, leptonic CP violation [Ruj99]. A Neutrino Factory would be the first of a new line of high-brilliance muon accelerators and an important first step towards a muon collider [Bud69], perhaps the route of choice to multi-TeV lepton-antilepton collisions. In addition, a Neutrino Factory complex will provide exceptionally intense beams of protons, pions and muons. These beams can be used to carry out a very broad spectrum of fundamental research in the fields of condensed matter physics and chemistry, materials science and medicine as well as nuclear and particle physics [Turner99, Pilaftsis99].

Two feasibility studies [StudyI, StudyII] have shown that a Neutrino Factory could be built using accessible technologies, with a performance matching the requirements of an exciting physics programme. Cost estimates, however, are quite high (\$1.9 billion in US Feasibility Study II [StudyII]), and several of the techniques envisaged have never been applied in practise. Several partially explored alternatives, with significant potential for cost reduction, exist for some of the subsystems. A sizeable programme of R&D is thus required.

Probably the largest novelty from the viewpoint of accelerator physics is ionization cooling. Proposed more than twenty years ago [Skrinsky81, Neuffer83, Pereved84] and generally considered sound, ionization cooling of muons at minimum-ionizing energy has never been realised in practise.<sup>1</sup> Yet it makes significant contributions to both the performance (up to a factor of 10 in neutrino intensity [Hanke00]) and cost (as much as 20% [StudyII]) of a Neutrino Factory. This motivates the proposal of a muon ionization cooling experiment, the importance of which has been recognised by both the US Muon Technical Advisory Committee (MUTAC) [MUTAC01] and the European Muon Coordination and Oversight Group [EMCOG02]. The aims of the proposed experimental programme are:

- to design, engineer, and build a section of cooling channel capable of giving the desired performance for a Neutrino Factory;
- to place this apparatus in a muon beam and measure its performance in a variety of modes of operation and beam conditions.

A successful demonstration is an important milestone in the R&D towards a Neutrino Factory. The point is not to demonstrate the *principle* of cooling, which is expected to result if all components work as specified, but to learn how to build and operate a device that performs as desired, and to prove this by measuring its performance in a beam. The experience gained from this experimental demonstration will provide input to the final design of the Neutrino

---

<sup>1</sup> “Frictional cooling” of very low-energy muons in solid absorbers has been demonstrated at PSI by M. Mühlbauer (see his PhD thesis, 1997) but appears to be inapplicable to a Neutrino Factory or Muon Collider.

Factory cooling channel, and allow the design of a Neutrino Factory Complex to be optimized with confidence. It is also important to study the cooling process by varying the relevant parameters so that an extrapolation can be made to a different cooling channel design, e.g., a ring, if this should be shown to be advantageous.

This approach is an essential complement to, and benefits from, the existing programmes of R&D on individual ionization-cooling-channel components that are already under way within the MUCOOL [MUCOOL98] programme and at CERN. An ionization-cooling channel combines low-Z absorbers, providing energy loss, with high-gradient RF cavities to re-accelerate the muons, all tightly packed within a magnetic focusing lattice. Practical, or perhaps fundamental, problems that would not necessarily show up in component R&D are bound to arise in such a combined system. Their discovery and solution could have a substantial impact on cooling-channel design and performance. The process of accumulating this irreplaceable experience will be long and should begin without delay.

The MICE collaboration has been created to carry out this programme. It consists of accelerator physicists and experimental particle physicists from Europe, Japan and the US. Through a series of workshops [WORK0001] and collaboration meetings [MICEweb], it has converged to a baseline scenario for a cooling experiment, presented in a preliminary form in the MICE Letter of Intent (LOI) [MICE01] which was submitted to CCLRC/PPARC towards the end of 2001. Encouraged by the positive report [MICEreview02] issued by the CCLRC/PPARC evaluation committee the MICE collaboration have prepared the present proposal to carry out the experiment at RAL. The goals of the experiment are:

- to build a section of a cooling channel that is long enough to provide a measurable cooling effect (up to  $\approx 10\%$  reduction in transverse emittance) but short enough to be affordable and flexible enough to allow a variety of beam momenta, optics and absorbers to be investigated.
- to use particle detectors to measure the cooling effect with high precision, achieving an absolute accuracy on the measurement of emittance of 0.1% or better.
- to perform measurements in a muon beam with momentum in the range 140–240 MeV/c. The beam intensity will be such that a single particle will pass through the experiment every 100 ns or so.

This proposal describes the experiment in detail. Since the submission of the LOI, further studies of the critical issue of the effect of RF-generated background on the detectors have been performed. A more precise costing and a more integrated technical design of the experiment have been carried out. The time development of the experiment has been studied and the critical-path items have been identified. The distribution of tasks within the collaboration and the milestones for the studies that will allow the remaining choices in the experimental design to be made have been established.

The proposal begins with a review of the physics case (the remainder of Section 1), followed by a discussion of ionization cooling (Section 2) and of the experimental technique to measure the effect (Section 3). The description of the cooling channel components can be found in Sections 4–6. It is shown in Section 7 that a muon beam line can be created at RAL with the characteristics required to carry out the experiment. The MICE particle detectors are described in Section 8. A discussion of the RF induced backgrounds and their effect on the tracking devices can be found in Section 9. Section 10 reviews the integration of the

apparatus, shows that there exists at least one possibility to satisfy the safety requirements related to the use of liquid hydrogen, and outlines the requests from the collaboration to the host laboratory. Section 11 describes the task assignments, the time-line and estimated cost. Section 12 provides a brief summary of the proposal.

## 1.2 Physics at a Neutrino Factory

### 1.2.1 Neutrino oscillations

It is now well established, from the observation of neutrino oscillations, that neutrinos have mass and mix. Taken together with the present limits on the absolute neutrino mass scale the results indicate that neutrinos are much lighter than all the other fundamental fermions [PDG02], while the values of the mixing angles are also very different from those of the quarks. These facts are difficult to understand in the context of the Standard Model, and it is quite possible that the mechanism that generates neutrino masses and mixing angles may be different to that which generates those of the other fermions [Murayama02]. The answer to this puzzle could possibly be found in grand unified theories, which provide a unified description of quarks and leptons at a very high energy scale and could make predictions for the parameters that describe neutrino oscillations. Precise measurements of the oscillation parameters can be used, therefore, to test the ideas of unification, and will perhaps lead to a deeper understanding of the nature of quark and lepton flavour.

The observation of neutrino oscillations also has far-reaching implications in astrophysics and cosmology. The small, but non-zero, neutrino mass may mean that neutrinos contribute as much mass to the universe as all the visible stars [Turner99]. Moreover, the recent KamLAND result strongly indicates that leptonic CP violation will be observable in neutrino oscillations, possibly leading to an understanding of the observed matter–antimatter asymmetry in the universe. The best, and possibly the only, machine that will allow this discovery is a Neutrino Factory.

None of these fundamental questions can find answers in the physics programme of either LHC or an  $e^+e^-$  collider, to which a Neutrino Factory would therefore be completely complementary.

Present results on neutrino oscillations can be readily understood if neutrinos have mass and there is mixing among the three known neutrino flavours; the three neutrino mass-eigenstates  $(\nu_1, \nu_2, \nu_3)$  are different from the three light-neutrino flavour-eigenstates  $(\nu_e, \nu_\mu, \nu_\tau)$  [Murayama02], and related to them by the neutrino mixing matrix:

$$U = \begin{pmatrix} c_{12} & s_{12} & 0 \\ -s_{12} & c_{12} & 0 \\ 0 & 0 & 1 \end{pmatrix} \begin{pmatrix} c_{13} & 0 & e^{-i\delta} s_{13} \\ 0 & 1 & 0 \\ -e^{-i\delta} s_{13} & 0 & c_{13} \end{pmatrix} \begin{pmatrix} 1 & 0 & 0 \\ 0 & c_{23} & s_{23} \\ 0 & -s_{23} & c_{23} \end{pmatrix} \quad (1.2.1)$$

The correspondence between the mass eigenstates and the weak eigenstates and the mixing angles that arise in equation 1.2.1 are depicted in Figure 1.1a. For three-neutrino flavour oscillations, there are six parameters: the three mixing angles shown in Figure 1.1a, a CP-violating phase parameter,  $\delta$ , and two mass-squared differences,  $\Delta m_{12}^2$  and  $\Delta m_{23}^2$ , where  $\Delta m_{ij}^2 = m_i^2 - m_j^2$ . Figure 1.1b shows schematically the two alternatives for the neutrino

mass spectrum that are allowed by the present data. Atmospheric neutrino measurements indicate that  $|\Delta m_{23}^2| \approx 2 \times 10^{-3} \text{ eV}^2$  while solar and reactor neutrino measurements indicate that  $\Delta m_{12}^2 \approx 5 \times 10^{-5} \text{ eV}^2$ . The atmospheric neutrino experiments indicate that  $\theta_{23}$  is nearly  $45^\circ$  (maximal mixing), while solar neutrino experiments require  $\theta_{12}$  in the range of  $25\text{--}40^\circ$ . Reactor experiments indicate that  $\theta_{13}$  is smaller than about  $10^\circ$ .

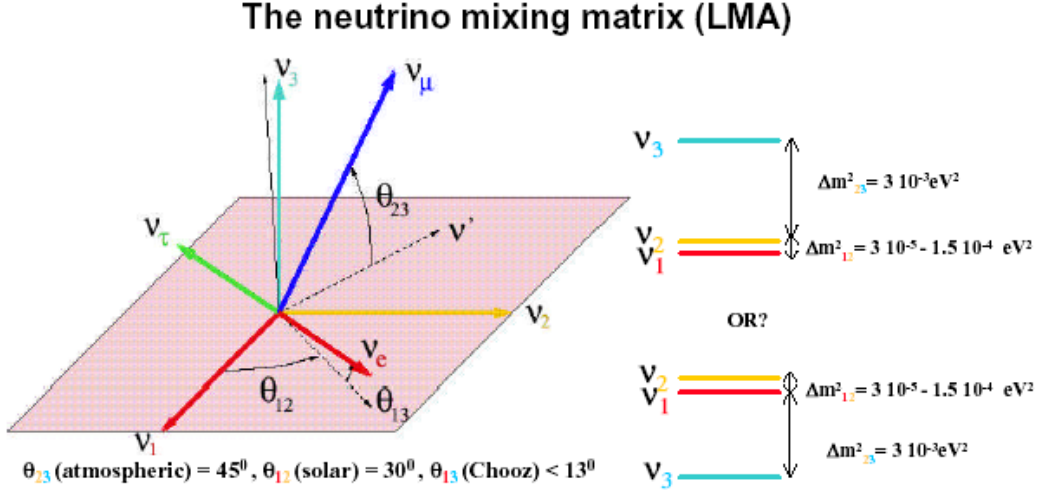


**Figure 1.1:** a) Rotation of the neutrino mass-eigenstates  $v_1, v_2$  and  $v_3$  into the flavour eigenstates  $v_e, v_\mu$  and  $v_\tau$  implied by equation 1.2.1. The definitions of the Euler angles  $\theta_{12}, \theta_{13}$ , and  $\theta_{23}$  are indicated. b) Neutrino mass spectra allowed by the present data.  $\Delta m_{12}^2$  is the mass-squared difference that relates to the solar neutrino data,  $\Delta m_{23}^2$  the one that relates to the atmospheric neutrino data.

### 1.2.1.1 Forthcoming measurements of the oscillation parameters

The next few years should produce major improvements in the knowledge of the neutrino oscillation parameters. Further results from SNO and KamLAND are expected soon. The combination of these measurements should, in particular, refine the knowledge of the small mass difference  $\Delta m_{12}^2$ . In addition, several new experiments, SIREN, LENS and HELLAZ, have been proposed to measure the  $pp$  solar neutrino spectrum [SIREN, Lasserre02, Gorodetzky02]. These experiments should further improve the accuracy with which the solar parameters can be determined.

Over the next ten years, long baseline experiments such as K2K (which has already reported results from its first two years of running), MINOS and the CERN to Gran Sasso (CNGS) experiments will report results [Lang01, Aprili02, Guler01]. These experiments are expected to confirm the neutrino oscillation interpretation of the Super-Kamiokande atmospheric neutrino results and determine the parameters  $\theta_{23}$  and  $\Delta m_{23}^2$  with an accuracy of about 10%. MINOS and ICARUS will also be sensitive to  $\sin^2 2\theta_{13}$  values as low as 0.04. In addition to these long baseline experiments there is a proposal to build an off-axis neutrino beam line at the recently approved Japanese Proton Accelerator Research Complex (J-PARC, formerly known as JHF [JPARC]) to illuminate the Super-Kamiokande detector. Discussions have also begun on building such a high-flux beam line using the NuMI beam line at Fermilab [NuMIOffAxis]. In addition, it is proposed to use the proton driver for an eventual CERN Neutrino Factory, the superconducting proton linac (SPL), initially to provide a low energy super neutrino beam, pointing at the International Frejus Laboratory in the Alps [Blondel01]. This would form the first stage of a CERN-based Neutrino Factory complex. These super neutrino beam experiments are likely to bring an improvement of about a factor of 5–20 on

the  $\theta_{13}$  sensitivity that will be achieved by the MINOS experiment. Such superbeam projects are natural stepping-stones to a Neutrino Factory.

Despite all the improvements in the knowledge of the neutrino parameters that these future experiments will bring, much will remain unresolved. In particular:

- i. It will be necessary to determine whether three-flavour mixing is the correct framework or whether sterile neutrinos, neutrino decay or CPT violation also contribute;
- ii.  $\sin^2 2\theta_{13}$  will still be poorly determined (or perhaps unmeasured);
- ii. the CP violating phase  $\delta$  will be unmeasured;
- iii. the sign of the 23 mass splitting  $-\text{sign}(\Delta m_{23}^2)$  is unlikely to be known.

### 1.2.1.2 Neutrino oscillation measurements at a Neutrino Factory

Physics with the Neutrino Factory has been discussed in several articles [NuFactPhys] and at the Neutrino Factory (NuFact) workshops that have taken place annually since 1999. It is the subject of active investigations by study groups in Europe, Japan and the US, and during the forthcoming workshops of the NuFact series.

The primary objective of physics at the Neutrino Factory will be the precise measurement of the elements of the neutrino mixing matrix. A neutrino beam derived from the decay of an intense stored-muon beam is the optimum tool for this purpose because it offers substantial advantages over conventional neutrino beams:

- i. The energy spectrum of the neutrino beam may be calculated precisely given the muon-beam energy, divergence and polarization.
- ii. The flavour composition of the neutrino beam is precisely known. Furthermore, the lepton numbers of the neutrino flavours that make up the beam are opposite, so that there is no ‘pollution’ of the oscillation signals.
- iii. The neutrino beam is unique in that it contains high-energy electron neutrinos. Not only will this allow the  $\nu_e \rightarrow \nu_\mu$  oscillations to be tagged using an experimentally clean ‘wrong-sign’ muon tag, but, since the beam energy will be above the  $\tau$ -production threshold, the important oscillation channel  $\nu_e \rightarrow \nu_\tau$  can be studied. The ability to study  $\nu_e \rightarrow \nu_\tau$  oscillation is unique to the Neutrino Factory.
- iv. Changing the polarity of the stored muon beam yields a charge-conjugate neutrino beam.
- v. In the immediate vicinity of the muon storage ring, the neutrino beams are very small and extremely intense.

The Neutrino Factory data set will be diverse, yielding six distinct sub-samples containing events tagged by the appearance of: (i) a right-sign muon; (ii) a wrong-sign muon; (iii) an  $e^+$  or an  $e^-$ ; (iv) a  $\tau^+$ ; (v) a  $\tau^-$ ; or (vi) the absence of a lepton. Measurements can be made with  $\mu^+$  and then with  $\mu^-$  stored in the ring. The most important event samples are those tagged by wrong-sign muons, which provide evidence for oscillations between electron neutrinos and muon neutrinos. For this signal the background rates at a Neutrino Factory are very low, about two orders of magnitude lower than the corresponding rates using conventional neutrino beams. This results in an improvement in experimental sensitivity of about two orders of magnitude. In addition, since the Neutrino Factory will provide intense high-energy

beams, oscillation baselines can be very long (thousands of km). The muon storage ring can serve two experiments located at significantly different long baselines.

The major physics measurements that will be made with this wealth of data are:

- i. Precise determination of  $\Delta m_{23}^2$  and of the mixing angle  $\theta_{23}$ ;
- ii. Measurement of the small mixing angle  $\theta_{13}$  with a precision of better than half a degree;
- iii. Observation of the matter effects incurred by electron neutrinos in their passage through the earth. The resulting asymmetry between the rates for  $\nu_e \rightarrow \nu_\mu$  and  $\bar{\nu}_e \rightarrow \bar{\nu}_\mu$  will allow a decisive determination of the sign of  $\Delta m_{23}^2$ ;
- iv. The search for leptonic CP violation through the precise measurement of the  $\nu_e \rightarrow \nu_\mu$ ,  $\bar{\nu}_e \rightarrow \bar{\nu}_\mu$  rate asymmetry as a function of energy and baseline.

The superiority of the Neutrino Factory compared with conventional sources of neutrino beams will be demonstrated by considering the determination of  $\sin^2 2\theta_{13}$  and the CP violating phase,  $\delta$ .

The calculated  $\sin^2 2\theta_{13}$  sensitivities (90% CL) of various long baseline neutrino facilities have been estimated in e.g. [Lindner02] and are shown in Figure 1.2. The sensitivity of a Neutrino Factory is compared with that of the J-PARC–SuperKamiokande project, a higher-energy off-axis project (NUMI off axis), a future high-intensity J-PARC neutrino beam illuminating a megaton water Cherenkov detector (HyperKamiokande) and an ‘entry level’ Neutrino Factory (one without cooling) of modest intensity. The leftmost ends of the bars indicate the purely statistical sensitivity and demonstrate the analysis power of a Neutrino Factory. Note that the sizes of the systematic errors (indicated by the dark-shaded regions) are well matched to the statistical sensitivities. The Neutrino Factory performance is about two orders of magnitude better than that of either the J-PARC–Super-Kamiokande or the NuMI project and about one order of magnitude better than the sensitivity expected if the J-PARC neutrino beam is used to illuminate Hyper-Kamiokande. The range of values of  $\sin^2 2\theta_{13}$  allowed by the data increases when correlations with other oscillation parameters are taken into account or the analysis is performed allowing multiple solutions to remain [Lindner02]. This limits the Neutrino Factory  $\sin^2 2\theta_{13}$  sensitivity to  $O(10^{-3})$ . However, the effect of correlations and degeneracies can be addressed by combining the results of different, complementary, experiments [Burget02], or by using the complementary  $\nu_e \rightarrow \nu_\tau$  transitions [Donini02]. The full sensitivity of a few times  $10^{-5}$  can be recovered in such analyses. Hence, Neutrino Factories can achieve sensitivities that are about two orders of magnitude better than can be achieved with conventional high-intensity neutrino beams (‘superbeams’).

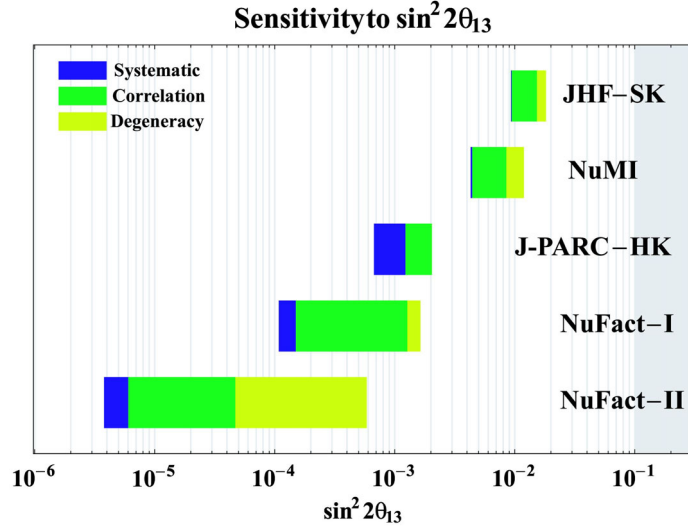


**Figure 1.2:** Sensitivity of ‘entry-level’ and high-performance Neutrino Factory (NuFact I and II respectively)  $\sin^2 2\theta_{13}$  compared with that of other proposed facilities. For the Neutrino Factory scenarios a single baseline of 3000 km,  $10^{19}$  (NuFact I) or  $2.6 \times 10^{20}$  (NuFact II) muon decays per year at a muon beam energy of 50 GeV are assumed. The correlations and multiple solutions can be addressed at a Neutrino Factory by combining data with those from previous results or by combining complementary measurements.

If present, CP violation (CPV) and matter effects will modify the measured  $\nu_e \leftrightarrow \nu_\mu$  oscillation probabilities. These modifications are different for neutrinos and antineutrinos. The predicted ratio of event rates  $N(\bar{\nu}_e \rightarrow \bar{\nu}_\mu) / N(\nu_e \rightarrow \nu_\mu)$  at a Neutrino Factory experiment with equal  $\mu^+$  and  $\mu^-$  running is shown as a function of baseline in Figure 1.3. With no CPV and no matter effects ( $L = 0$ ) the ratio is 0.5, reflecting the different neutrino and antineutrino cross sections. As  $L$  increases the ratio is enhanced (suppressed) by matter effects if the sign of  $\Delta m_{32}^2$  is negative (positive). At sufficiently long baselines the matter effects are much larger than effects due to possible CPV (indicated by the bands in the figure). The sign of  $\Delta m_{32}^2$  and the CP phase  $\delta$  can therefore be determined by precise measurements of  $N(\bar{\nu}_e \rightarrow \bar{\nu}_\mu) / N(\nu_e \rightarrow \nu_\mu)$ . However, in this analysis the values of  $|\Delta m_{32}^2|$ ,  $\Delta m_{21}^2$ , and  $\sin^2 2\theta_{13}$  have been fixed. A fit to determine all these parameters including the effects of correlations and ambiguities shows that the Neutrino Factory sensitivity exceeds that of the superbeam projects by  $\sim 1$ – $2$  orders of magnitude.

If the LSND oscillation result is confirmed, the simple three-flavour mixing framework will need to be modified to include, for example, additional light neutrinos that are sterile and/or CPT violation. Some information on  $\nu_\mu \leftrightarrow \nu_e$  and  $\nu_\mu \leftrightarrow \nu_\tau$  oscillations will already be available. It seems likely that there will be a premium on searching for and measuring  $\nu_e \rightarrow \nu_\tau$  oscillations, a programme unique to the Neutrino Factory. It has been shown [Barger02] that there are viable regions of four-neutrino mixing parameter space in which both CPV and thousands of  $\nu_e \rightarrow \nu_\tau$  events could be seen at a Neutrino Factory delivering only  $O(10^{18})$  decays/yr.

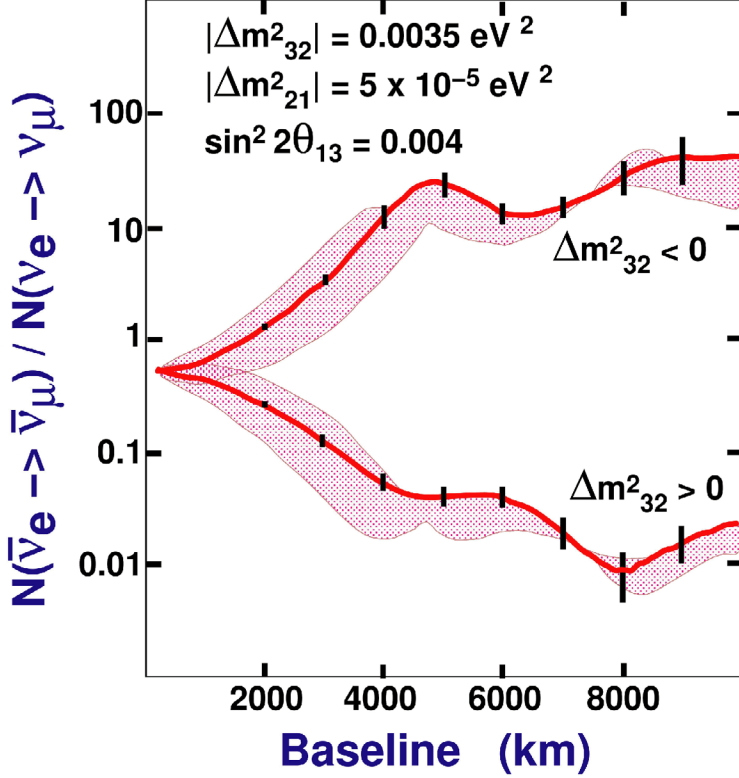


**Figure 1.3:** Predicted ratios of wrong-sign muon event rates when  $\mu^+$  and  $\mu^-$  are stored in a 20 GeV Neutrino Factory, shown versus baseline. The two bands correspond to the two signs of  $\Delta m_{23}^2$ . The widths of the bands show the variation as the CP phase  $\delta$  changes from  $-\frac{\pi}{2}$  to  $+\frac{\pi}{2}$ . The thick lines are for  $\delta = 0$ . The statistical errors correspond to a Neutrino Factory providing  $10^{21}$  muon decays with a 50 kt detector.

### 1.2.2 High-intensity neutrino deep inelastic scattering

There is a long and rich history of neutrino deep inelastic scattering (DIS) experiments, and structure function measurements from the current generation of experiments are routinely used in ‘global fits’ for parton distribution functions, sum-rule tests,  $\alpha_S$  determinations etc. However, *precision* neutrino DIS physics is more difficult: with neutrino beams from pion decay, large, dense nuclear targets are required (giving unknown heavy-target effects), the energy spectrum of the neutrino beams is relatively poorly determined, and there is an imbalance in the flux of neutrinos and antineutrinos.

At a Neutrino Factory, neutrino DIS would become a high-precision science [Albright00, Mangano01].  $O(10^{20})$   $\mu$ -decays/year would deliver high-intensity, collimated neutrino and anti-neutrino beams. Even with compact liquid hydrogen and deuterium targets, the expected event rates would be typically an order of magnitude more than is available from current experiments. The spread in accurately determined (neutrino) beam energies would allow the different structure functions to be disentangled and thus a complete flavour decomposition of the nucleon structure to be performed [Ball00]. The precise determination of the strong coupling constant,  $\alpha_S$ , will be possible from the scaling violations of the structure functions. The ‘EMC effect’ can be studied using a combination of heavy and light nuclear targets. The ability to tag charm in the final state would allow the CKM matrix elements  $|V_{cd}|$  and  $|V_{cs}|$  to be measured with a precision comparable to the present precision on  $|V_{us}|$  using processes such as  $(d,s)+W^+ \rightarrow c$ . A measurement of  $D^0\bar{D}^0$  mixing could also be made. Finally, with polarized targets, a new realm of high-precision *spin physics* would open up. The high event

rate would allow the determination of the individual flavour components with accuracies of a few percent.

In addition to precision QCD measurements, the electroweak sector of the Standard Model can also be tested at a Neutrino Factory. Particularly important is the extraction of  $\sin^2 \theta_W$  from  $\nu_e$  and  $\nu_\mu$  cross sections. For the former, the most accurate current measurements come from the NuTeV experiment. Studies suggest that the current (NuTeV) error of  $\Delta \sin^2 \theta_W \approx 0.002$  could be improved by about a factor of 20 at a future Neutrino Factory, with corresponding implications for indirect determinations of the Higgs mass, etc.

Finally, it is important to assess the existing state of knowledge of proton structure at the time when the Neutrino Factory measurements will be made. The HERA  $e^\pm p$  collider can access a similar range of information from charged current and neutral current cross sections, over a similar range of the Bjorken scaling-variable,  $x$ , but typically at much higher four-momentum-transfer squared,  $Q^2$ . The advantages of the Neutrino Factory are: (i) much higher statistics; (ii) target type flexibility; (iii) target polarization. The two machines are clearly complementary in terms of the various types of structure functions that can be measured and the  $x$ ,  $Q^2$  range that can be covered.

### 1.2.3 Non-neutrino science at a Neutrino Factory

The Neutrino Factory can be used to produce intense beams of muons with momenta of a few hundred MeV/ $c$  or less and a variety of time structures [Aysto01]. These can be used for ‘slow-muon’ physics studies and will have a flux that will exceed any existing or proposed muon source by 3–4 orders of magnitude (for the breadth of physics opportunities provided by slow muon sources see, for example, the reviews [Blundell99, Cox87, Dalmas97]). This large flux of stopped muons will allow exquisitely sensitive searches for rare muon decays to be carried out, providing stringent tests of the consistency of the Standard Model. In addition, precise determinations of the muon magnetic moment, high statistics studies of muonium and precise measurement of the muon lifetime will allow many parameters of the Standard Model to be determined with unprecedented precision, thus allowing sensitive searches for physics beyond the Standard Model.

Slow muon beams are also of great importance in the study of the atomic and molecular properties of matter. The current intensity of the muon sources available for condensed matter physics research is rather low (typically  $\sim 10^4$  to  $\sim 10^5$  muons per second) at ISIS (RAL) and PSI (Switzerland) for experiments measuring time-dependence, although  $\sim 10^6 \text{ s}^{-1}$  is available at PSI in the most intense beam. The provision of a high intensity muon beam via the Neutrino Factory will allow:

- the study of problems in surface magnetism, polymer and liquid crystal films;
- the study of small samples and time dependent phenomena;
- the elucidation of dynamical effects through the use of high magnetic field level-crossing resonance.

## 1.3 Neutrino Factory accelerator complex

As the neutrino beams at a Neutrino Factory will be produced from the decay of muons circulating in a storage ring, the primary aim of the accelerator complex is to store as high a

muon intensity as possible. This will be achieved using a high power proton source to create intense bunches of protons which are fired into a target. As many of the pions created in this collision as possible will be captured and transported along a decay channel, where they will decay to muons. The resulting muon beam will have a large size and a large spread in longitudinal and transverse momentum, i.e., a large emittance, which must be reduced to avoid a large fraction of the muons being lost during acceleration and subsequent injection into the storage ring. The reduction of the momentum spread and transverse emittance takes place in two stages, called respectively phase rotation and cooling. The muons are then accelerated to a final working energy in a series of accelerators, before being injected into the storage ring.

A number of different designs exist for the Neutrino Factory. Although there are substantial differences between them, each design consists of the same basic components. Figure 1.4 shows how these components are laid out in the CERN design. A proton driver produces the very high proton-beam-power (4 MW) necessary to achieve the neutrino intensity required for the neutrino oscillation studies. To minimize the longitudinal emittance of the initial muon beam, the proton bunches must be no more than a few nanoseconds long.

Due to the high beam-power and small size, the power density in the target far exceeds that of any comparable facility. Building a target that can withstand the mechanical and thermal stresses that such a beam will create is a major challenge and is the subject of an active R&D programme [BNL-E951, CERN-targetry]. Three different mechanisms have been suggested for focusing and capturing the pions produced in the target: a 20 T combined superconducting and warm magnet system, a magnetic horn or a wide-aperture bending magnet.

Once captured, the pions decay to produce muons in a decay channel that is 30–40 m long. To attain the highest muon flux, this channel must have large acceptance for the pions, which implies a combination of wide aperture and strong magnetic field. The most likely way to satisfy these requirements is to use solenoidal magnets, rather than the magnetic quadrupoles that are usually employed for such purposes.

The large momentum spread of the decay muons will be reduced using phase rotation in which early (high energy) particles are de-accelerated and late (low energy) particles are accelerated using, for example, a system of RF cavities. The muons can then be captured into RF bunches, and the transverse emittance reduced using an ionization cooling channel. Ionization cooling is discussed in detail in Section 2, but to summarize: the muons are passed through a material, called an absorber, where they lose both longitudinal and transverse momentum. The lost longitudinal momentum is restored using RF cavities following the absorber. The result of this process is a net reduction in transverse momentum spread. However, as well as the cooling coming from the energy loss, there is also heating coming from multiple scattering and the net cooling is a delicate balance between these two effects.

The muons are accelerated to the final working energy, e.g., 20 or 50 GeV, using a series of linear accelerators and re-circulating linear accelerators. In the latter, the beam is accelerated through the same RF cavities a number of times, getting the same acceleration in each pass.

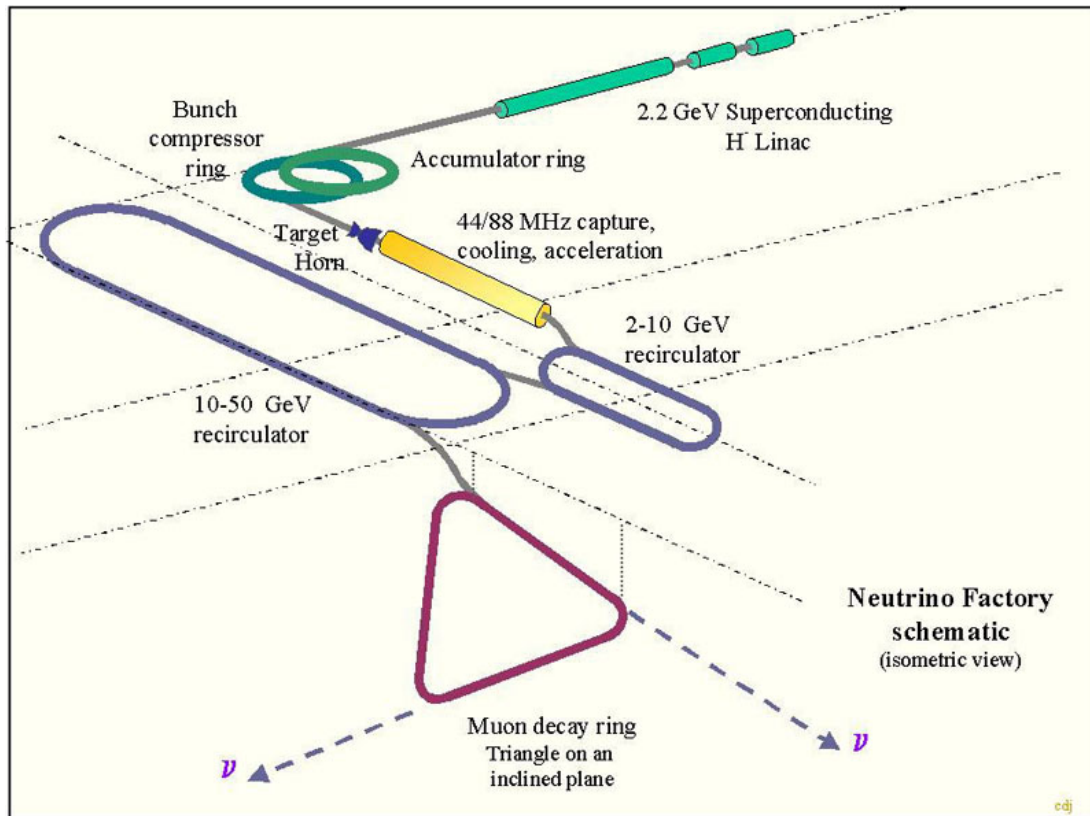


**Figure 1.4:** Conceptual layout of the various components of a Neutrino Factory complex (CERN scenario).

Once at the working energy, the muons are injected into the storage ring. It is desirable that the ring satisfy two main requirements. First, as much of the ring as possible should be in the form of straight sections since the decay of the high-energy muons will produce intense neutrino beams primarily in the directions in which these are pointing. Second, the straight sections should point at two or more experiments in different underground laboratories. As shown in Figure 1.4, the favoured method of doing this is to make the storage ring a 'triangular' shape.

## 2 Cooling

### 2.1 Principle of ionization cooling

The physics performance of a Neutrino Factory is based not only on the clean composition and precisely known flux of the neutrino beam, but also and importantly on the available intensity. The use of ionization cooling increases the density of muons within the volume of phase-space that can be accelerated [Hol03a] and improves the performance of the Neutrino Factory by a factor that ranges from 4 to 10 depending on the design [StudyII, Hanke00]. Although it saves considerably on the cost of the accelerating devices, cooling as is presently envisaged is itself expensive, representing as much as 20% of the Neutrino Factory cost, as can be seen from Table 2.1, extracted from US StudyII [StudyII].

**Table 2.1:** Bare construction-cost estimate (in \$M, not including engineering design, escalation, overhead, or contingency) for the Study-II Neutrino Factory.

<b>System</b>	<b>Total</b>
Proton Driver	184.4
Target Systems	100.8
Decay Channel	5.1
Induction Linacs	351.0
Bunching	75.5
Cooling Channel	348.7
Pre-accel. Linac	207.8
RLA	391.0
Storage Ring	118.1
Site Utilities	139.6
<b>TOTAL</b>	<b>1922.0</b>

As noted in Section 1, cooling of the transverse phase-space coordinates of a muon beam can be accomplished by passing the beam through energy-absorbing material and accelerating structures, both embedded within a focusing magnetic lattice; this is known as ionization cooling [Skrinsky81, Neuffer83]. Other cooling techniques (electron, stochastic, and laser cooling) are far too slow to yield a significant degree of phase-space compression within the muon lifetime. Ionization of the absorbing material by the muons decreases the muon momentum while (to first order) not affecting the beam size; at the same time, multiple Coulomb scattering of the muons in the absorber increases the beam divergence, heating the beam.

Cooling is discussed quantitatively in terms of emittance  $\varepsilon$ , defined as the volume occupied by a beam in phase space. This can be expressed as  $\varepsilon = \sqrt{|D|}$ , where  $D$  is the determinant of the 6-dimensional covariance matrix of the beam particles in the 6D coordinates  $(x, y, t, dx/dz, dy/dz, dt/dz)$ . Normalized emittance  $\varepsilon_n$  is obtained by using the coordinates  $(x, y, t, p/mc \cdot dx/dz, p/mc \cdot dy/dz, p/m \cdot dt/dz)$ .<sup>2</sup> The same calculation performed in the 4D space of spatial

---

<sup>2</sup> With the last three phase-space coordinates scaled with momentum, normalized emittance takes account of the natural decrease of beam size with acceleration, which does not constitute cooling.

coordinates yields the transverse 4D emittance. The transverse emittance is defined as the emittance in one 2D plane ( $x, dx/dz$ ); in a solenoid channel, the cylindrical symmetry argues for this to be calculated as the square-root of the transverse 4D emittance. The longitudinal emittance is defined similarly in the time-energy dimensions.

Within an absorber, normalized transverse emittance  $\varepsilon_n$  behaves approximately as [Neuffer87]

$$\frac{d\varepsilon_n}{ds} = -\frac{1}{\beta^2} \left\langle \frac{dE_\mu}{ds} \right\rangle \frac{\varepsilon_n}{E_\mu} + \frac{1}{\beta^3} \frac{\beta_\perp (0.014)^2}{2E_\mu m_\mu X_0}, \quad (2.1)$$

where  $s$  is path length, angle brackets denote mean value, muon energy  $E_\mu$  is in GeV,  $X_0$  is the radiation length of the absorber medium in m,  $\beta_\perp$  is the optical beta-function in the magnetic channel in m, and  $\beta$  is the particle velocity. This expression is appropriate to the cylindrically-symmetric case of solenoid focusing, where  $\beta_x = \beta_y = \beta_\perp$ . The first term in this equation is the cooling term and the second is the heating term.

To minimize the heating term, which is proportional to  $\beta_\perp$  and inversely proportional to radiation length, it has been proposed [Anken99] to use liquid hydrogen as the energy-absorbing medium, with  $dE/ds = 30$  MeV/m and  $X_0 = 8.7$  m, and to use superconducting solenoid focusing to give a small value of  $\beta_\perp \sim 10$  cm, rather than quadrupoles; this corresponds to large beam divergence at the location of the absorbers, so that scattering in the absorbers gives a relatively small contribution to the emittance. Key issues in absorber R&D include coping with the large heat deposition by RF dark currents and the intense ( $10^{14}$  muons per second) muon beam of the Neutrino Factory, while minimizing scattering in absorber-vessel windows, which are by necessity of higher- $Z$  material.

An additional technical requirement is high-gradient re-acceleration of the muons between absorbers to replace the lost energy, so that the ionization-cooling process can be repeated many times. Ideally, the acceleration should exceed the minimum required for momentum replacement, allowing ‘off-crest’ operation. This gives continual rebunching, so that even a beam with large momentum spread remains captured in the RF bucket. Even though it is the absorbers that actually cool the beam, for typical accelerating gradients (around 10 MeV/m), the RF cavities dominate the length of the cooling channel (see e.g. Figure 2.1). The achievable RF gradient determines how much cooling is practical before an appreciable fraction of the muons have decayed or drifted out of the bucket.

It follows from the above equation that the percentage decrease in normalized emittance is proportional to the percentage energy loss. Low beam energy is favoured because it requires less re-accelerating voltage. The negative slope of  $(dE/dx)/E$  [PDG02] at low energies leads to longitudinal heating, while the positive slope at high energies comes with an increase in straggling. So, most muon-cooling designs and simulations to date have used a momentum near the ionization minimum, between 150 and 400 MeV/ $c$ . This is also the momentum range in which the pion-production cross-section of thick targets tends to peak, and is thus optimal for muon production as well as cooling.

Intuition, calculations using linear ionization cooling theory and detailed simulations indicate that the process, if effected in a homogeneous magnetic field, will decrease the transverse momentum of the muons, but not the beam size itself. In order to convert the reduction of angles into a reduction of beam size, a change in optical functions is necessary. This can be done in various ways, the most drastic one being to perform a magnetic field reversal, which

can also be used as a way to reduce the beta function. The beta function can be squeezed in a periodic way by repeated field reversals (FOFO or SFOFO cooling cells), or only a few times during the cooling process (single- or double-flip cooling channel [Balbekov00]). The difficulty in the design of a cooling channel is to integrate the three basic elements – low-Z absorbers, RF cavities and solenoid focusing – in the most compact and economical way. The engineering rendering of a section of cooling channel is shown in Figure 2.1 for the periodic design of US Muon Collaboration Study-II [StudyII], which envisages use of 201-MHz cavities. The proposed CERN scheme, which envisages 88-MHz cavities [Lombardi01, Franchetti02] is largely similar with two main differences: i) the lower frequency cavities being much larger, the solenoids are inserted in the neck of the cavities; the lower frequency also leads to a lower average electric field of 4 MV/m; ii) the combination of a lower frequency and of a selection of muons with higher velocity (kinetic energy 200 MeV) allows particles originating from one single proton bunch to be kept in one single muon bunch throughout the front-end of the Neutrino Factory.

## 2.2 Cooling channel design

There have been many iterations of cooling section designs, both in the US and European studies. A cooling device desirable for experimental test is a section of a cooling channel from a viable high-performance Neutrino Factory design. It is defined by a few important characteristics:

1. The cooling factor. The transverse emittance reduction in a short cooling section is at best a factor  $\Delta\varepsilon/\varepsilon = \Delta E/E$ , where  $\Delta E$  is the average energy loss in the absorbers (and restored in the RF cavities) and  $E$  is the average particle kinetic energy. For muons of 200 MeV/c, a ‘10% cooling experiment’ requires an energy loss of about 20 MeV and a similar gain in the RF system.

2. The RF system, characterized in particular by its frequency. There are several existing scenarios: in the scheme developed for the US Study II [StudyII], cooling is performed with 201 MHz cavities; in the scheme developed at CERN the cooling is performed at 88 MHz. These differences in Neutrino Factory design are motivated by the different preparation of the beam prior to the cooling section. Another crucial parameter to consider for the cooling channel is of course the gradient that can be achieved with such RF systems. Cooling experiment designs have been developed in which the frequency is 88 MHz or 201 MHz. While the choice for the cooling experiment proposed here (201 MHz) has been made on the basis of performance and practicality [88-vs-201], the experience gained will be beneficial for any of the schemes currently contemplated.

3. The beam to be cooled. It is characterized by its average energy, energy spread, beam size and angular divergence. In a Neutrino Factory design, the beam has properties that vary along the cooling channel. One should vary the beam characteristics in a test experiment to reproduce this variety of conditions all the way down to the equilibrium emittance. Here is an example of typical beam properties:

- Momentum 200 MeV/c
- Momentum spread  $\pm 10\%$
- Beam size 5 cm rms in both projections
- Beam angular divergence 150 mrad rms in both projections

4. The magnetic field and diameter of the magnetic channel, typically 4 T field with an aperture of 15 cm radius.

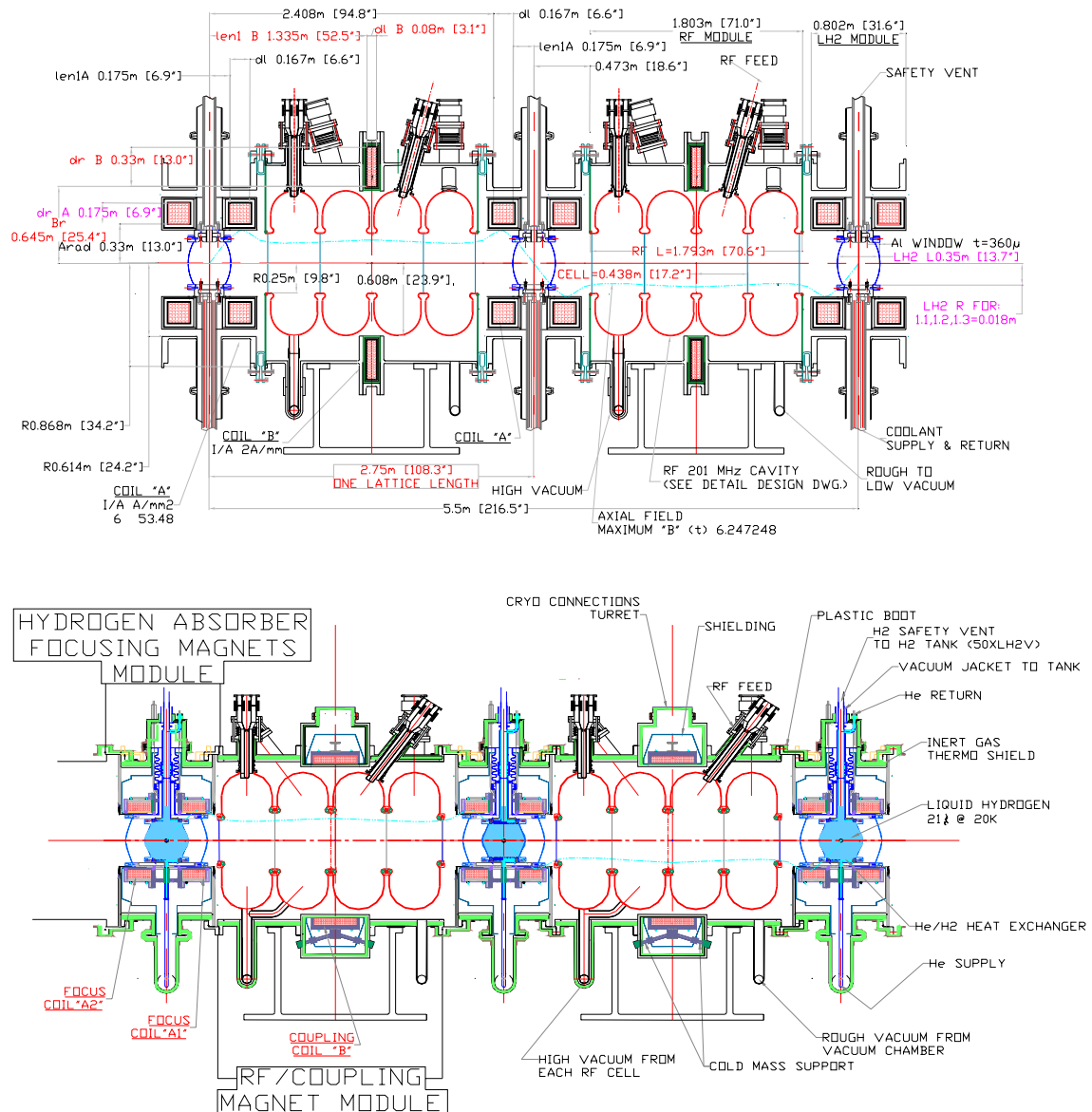


**Figure 2.1:** Top: Engineering rendering of the 201 MHz cooling channel (from US Neutrino Factory Feasibility Study II [StudyII]). Shown in cross section are three liquid-hydrogen absorbers, each enclosed within a pair of ‘focusing’ solenoids, interspersed with two 4-cavity 201 MHz RF assemblies, each encircled by a ‘coupling’ solenoid. Bottom: engineering rendering of the cooling section of MICE. The radius of the coils is reduced to save cost, while the safety windows and argon jacket are motivated by compliance with safety requirements (see Section 10).

One of the characteristics of a cooling channel is the equilibrium emittance. A beam at equilibrium emittance would traverse the channel without net reduction or increase of its emittance. A precise measurement of this quantity for various configurations of magnetic field and beam momentum, and comparison with that expected from simulation, given approximately by

$$\epsilon_n^{(equ.)} = \frac{\beta_{\perp} (0.014)^2}{2\beta m_{\mu} \frac{dE_{\mu}}{ds} X_0}, \quad (2.2)$$

is one of the quantitative aims of the experiment.

A detailed, integrated simulation of the beam line, instrumentation and cooling apparatus is essential for the success of the Muon Ionization Cooling Experiment. The performance measured with MICE will be compared with the performance calculated from the detailed simulations. Three distinct computer codes are used: ICOOL [Fernow99], developed at BNL, a beam line simulation toolbox [BeamTools] based on Geant4 [Geant4], developed at FNAL, and PATH [PATH], developed at CERN. These codes have been used extensively in ionization cooling design studies and their results are in excellent agreement.

## 2.3 Other absorber materials

Besides hydrogen, other candidate absorber materials include helium, lithium, lithium hydride, methane, and beryllium. All other things being equal, these will all give a worse cooling performance than hydrogen. For fixed  $\beta_{\perp}$ , a possible figure of merit is  $(X_0 \langle dE/ds \rangle_{\min})^2$ . This is proportional to the four-dimensional transverse-cooling rate, or to the density of particles in the core of the beam at equilibrium emittance. Table 2.2 shows this figure of merit for various materials, normalized to that of liquid hydrogen. Hydrogen is best by a factor  $\approx 2$  or more over any of them. For liquid hydrogen, metallic windows, necessary for containment and safety, might compromise this advantage (this is partially true also for liquid helium and lithium hydride). Substantial design and prototyping work [Kaplan-NuFact01, Kaplan-PAC01, Cummings-NuFact02] has shown that liquid-hydrogen absorbers can be safely realised with thin aluminium windows; depending on the precise absorber length and details of window design and material (see Section 6.2), the figure of merit is reduced to values situated between 0.65 and 0.8, which is still substantially superior to any other material. These calculations take into account the fact that, due to the low density of hydrogen, the absorber may sample  $\beta_{\perp}$  values somewhat larger than the minimum. The advantage of hydrogen is fully felt when the muon beam nears equilibrium emittance, towards the end of a linear cooling channel or in a cooling ring. For the Neutrino Factory cooling channel, this means that either the performance will be worse if hydrogen is not used, with potential cost implications for other parts of the project, or a more expensive channel will be required to attain the same performance.

Because hydrogen is the material with the best cooling performance, and is the most challenging to handle, it is essential that it be tested in MICE. Liquid hydrogen is thus the baseline absorber material for this proposal. The design of MICE is such that the easier options of performing measurements with liquid helium or with a thin disc of solid material (such as lithium hydride, pure lithium or plastic) can also be implemented. This will allow systematic studies of absorber issues.

**Table 2.2:** Comparison of ionization-cooling merit factor (see text) for various possible absorber materials, without windows.

<b>Material</b>	$\langle dE/ds \rangle_{\min}$ [MeV g <sup>-1</sup> cm <sup>-2</sup> ]	$X_0$ [cm]	<b>Merit</b>
Gaseous H <sub>2</sub>	4.103	61.28	1.03
Liquid H <sub>2</sub>	4.034	61.28	1
He	1.937	94.32	0.55
LiH	1.94	86.9	0.47
Li	1.639	82.76	0.30
CH <sub>4</sub>	2.417	46.22	0.20
Be	1.594	65.19	0.18

## 2.4 Possible extensions (gas cooling and ring coolers)

Another absorber approach under consideration is gaseous hydrogen at high pressure. Although RF accelerating cavities have always been operated in vacuum, the literature on the effects of high-pressure gas on high-voltage breakdown [Meek78] suggests that pressurized cavities could be feasible, and may even have advantages for muon acceleration and cooling. In this concept, the absorbers are integrated into the cavities, avoiding the deleterious effects of windows, shortening the cooling channel, and bringing about a more adiabatic behaviour of the beam (constant average momentum rather than the ‘saw-tooth’ characteristic of a cooling channel with liquid absorbers). In addition, if the hydrogen is cooled to (say) liquid-nitrogen temperature, the reduced resistivity of the copper cavity walls may allow operation at substantially higher accelerating gradient. The pressurized RF cavity concept was the subject of a successful 2002 STTR proposal to the US Dept. of Energy by a small Illinois company (Muons, Inc., R. Johnson, PI) in collaboration with IIT. If prototype bench tests are successful, Muons, Inc. plan to submit further grant proposals to fund construction of a pressurized-gas cooling cell for testing in a future phase of MICE.

So far, the cooling channels that could be successfully simulated and engineered are linear, i.e., the muons traverse each cell only once. As a muon beam passes through such an ionization-cooling lattice, its longitudinal emittance tends to grow, due to such effects as energy-loss straggling. If not controlled, this leads to beam losses and limits the degree of transverse cooling that is practical to achieve. There is hope that a ring system could allow the same cooling cells to be used several times, allowing substantial economy, with the added benefit that longitudinal emittance can be reduced in the process, via ‘emittance exchange’ [Neuffer99, Kaplan01]. Significant progress has been made in this direction [Palmer02]. The design of the ring cooling sections tends to be very similar to those proposed for the linear, single-pass channel, and involves similar components (see Figure 2.2). Thus what will be learned from the cooling experiment will apply to a ring system, if a successful design is found. Components specifically engineered for a ring cooler might also be tested in a future, emittance-exchange phase of MICE.

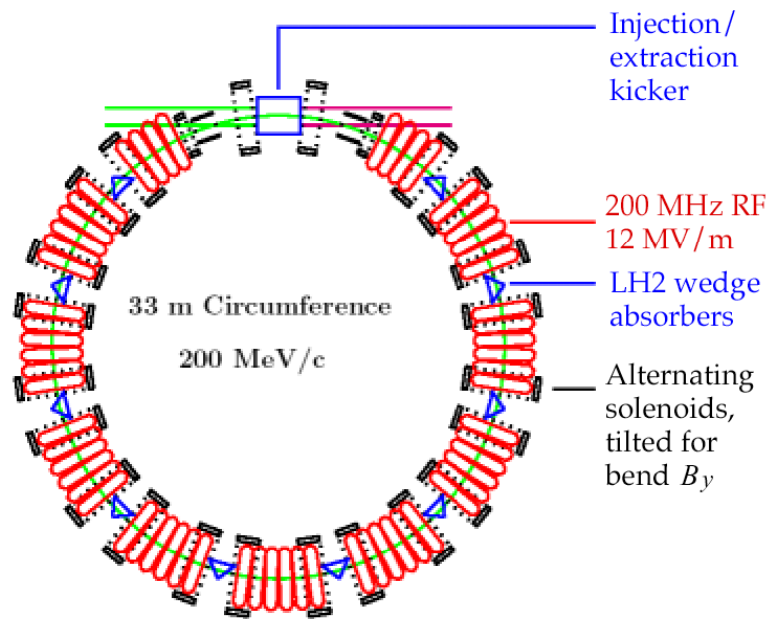


**Figure 2.2:** Schematic sketch of a ring cooler based on 201-MHz cavities, liquid-hydrogen-wedge absorbers, and superconducting solenoids [Palmer02].

### 3 The International Muon Ionization Cooling Experiment

#### 3.1 Layout of the experiment

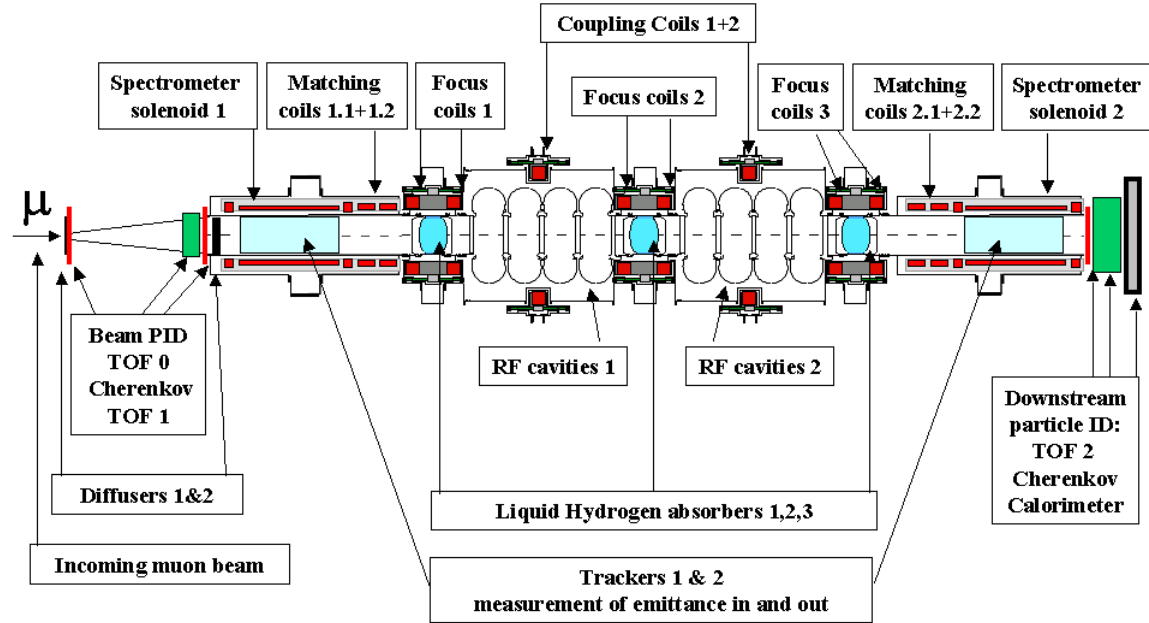


**Figure 3.1:** Artist's view of the International Muon Ionization Cooling Experiment (MICE), with the beam entering from the left.

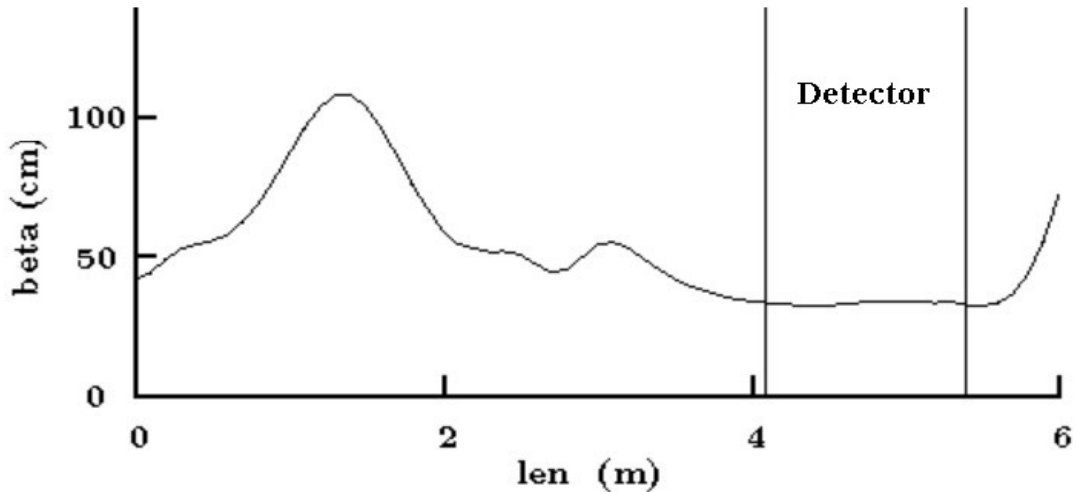
The main components of MICE are outlined in Figure 3.1. Cooling is provided by two cells from the first part of the 201 MHz cooling channel of the US StudyII [StudyII]. Some components of these cells have been modified to reduce cost and comply with RAL safety requirements. The incoming muon beam encounters first a beam preparation section, where a pair of high-Z (lead) diffusers generates a tuneable input emittance. In this section, a precise time measurement is performed and the incident particles are identified. There follows a first spectrometer, in which momentum, position and angles of each incoming particle are measured by means of tracking devices embedded in a uniform-field solenoid. Next comes the cooling section itself, with hydrogen absorbers and RF cavities, the focusing optics being provided by superconducting coils. The default magnetic configuration is such that the magnetic field changes sign at the centre of each absorber. The momentum, position and angles of the outgoing particles are measured in a second spectrometer, identical to the first one. At the downstream end of the experiment, another time-of-flight (TOF) measurement is performed, and particle identification by means of a Cherenkov counter and a calorimeter eliminates muons that have decayed in the apparatus. Details are given in Section 4 for the magnet system, in Section 5 for the RF, in Section 6 for the hydrogen absorbers and in Section 8 for the detectors.

The positions and operating parameters of the elements of MICE are summarized in Table 3.1. All simulations in this section have been performed based on these values.

**Table 3.1:** Position along the beam line and operating parameters of the elements of MICE

Item	$z_0$ [mm]	$\Delta z$ [mm]	Properties
Diffuser 1	-10000	1.4	lead
TOF 0	-9950	50	plastic scintillator $\sigma(t) = 50$ ps
TOF 1	-50	50	plastic scintillator $\sigma(t) = 50$ ps
Diffuser 2	0	22.4	lead
Correction coil 1.1	500	120	
Spectrometer solenoid 1	680	1260	
Tracker 1	810	1000	uniform-field region, $B = 4$ T
Correction coil 1.2	2000	120	
Matching coil 1.1	2269	202	
Matching coil 1.2	2519	202	
Focus coil 1.1	3042	200	
Hydrogen absorber 1	3187	350	energy loss 11 MeV
Focus coil 1.2	3482	200	
RF 1	3877	1720	4 201-Mhz cavities separated by Be windows; accelerating gradient 8.3 MV/m
Coupling coil 1	4567	350	
Focus coil 2.1	5792	200	
Hydrogen absorber 2	5937	350	energy loss 11 MeV
Focus coil 2.2	6232	200	
RF 2	6627	1720	4 201-Mhz cavities separated by Be windows; accelerating gradient 8.3 MV/m
Coupling coil 2	7317	350	
Focus coil 3.1	8542	200	
Hydrogen absorber 3	8687	350	energy loss 11 MeV
Focus coil 3.2	8982	200	
Matching coil 2.2	9503	202	
Matching coil 2.1	9753	202	
Correction coil 2.2	10104	120	
Spectrometer solenoid 2	10284	1260	
Tracker 2	10414	1000	uniform-field region, $B = 4$ T
Correction coil 2.1	11604	120	
Cherenkov	11824	560	aerogel $n = 1.02$
TOF 2	12390	50	plastic scintillator $\sigma(t) = 50$ ps
Calorimeter	12900	150	scintillating-fibre lead spaghetti calorimeter

As noted, the cooling experiment consists of two complete cooling channel cells. One additional absorber finishes the cooling section, both for reasons of symmetry and to protect the trackers against dark currents emitted by the RF cavities. To avoid emittance growth, the magnets in these two cells must be matched to the spectrometer solenoids. This is done using two sets of matching coils situated between the solenoids and the focus pairs. Correction coils around each spectrometer solenoid ensure a uniform field of 4 T for a length of 1 m.



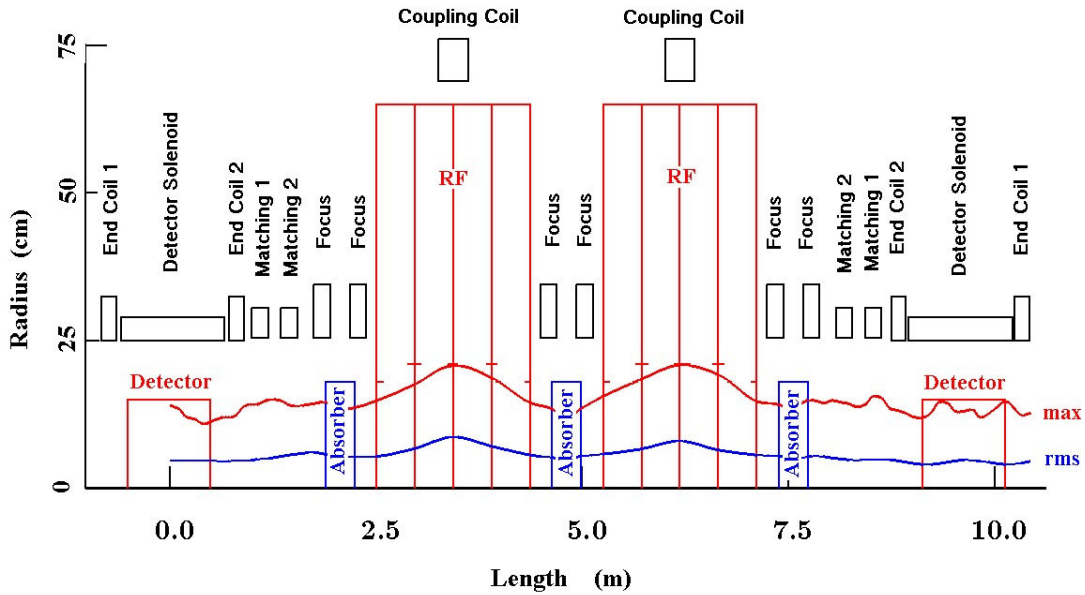
**Figure 3.2:** Beta function vs length through the match. The coordinate  $z = 0$ , around which this function is symmetrical, is at the middle of the central hydrogen absorber 2.

Figure 3.2 shows the matched beta function for the central momentum of  $200 \text{ MeV}/c$ . It is essentially constant in the detector, indicating that the required matching is achieved. As will be seen in Section 3.5, the experiment can be matched within a momentum range from  $140$  to  $240 \text{ MeV}/c$ , and the beta function at the absorbers can be tuned down to a few centimetres.

## 3.2 Beam dynamics and quantities to be measured

This section describes the behaviour of the beam in the channel and delineates the quantities that could be measured to characterize it. Following earlier simulations of the cooling experiment with PATH both for the  $88 \text{ MHz}$  and the  $201 \text{ MHz}$  designs [Aleksa02, Franchetti02], the simulations presented here were performed with ICOOL [Fernow99, Hol03a], which includes energy loss, multiple scattering, straggling in the hydrogen absorbers and realistic descriptions of all magnetic fields.

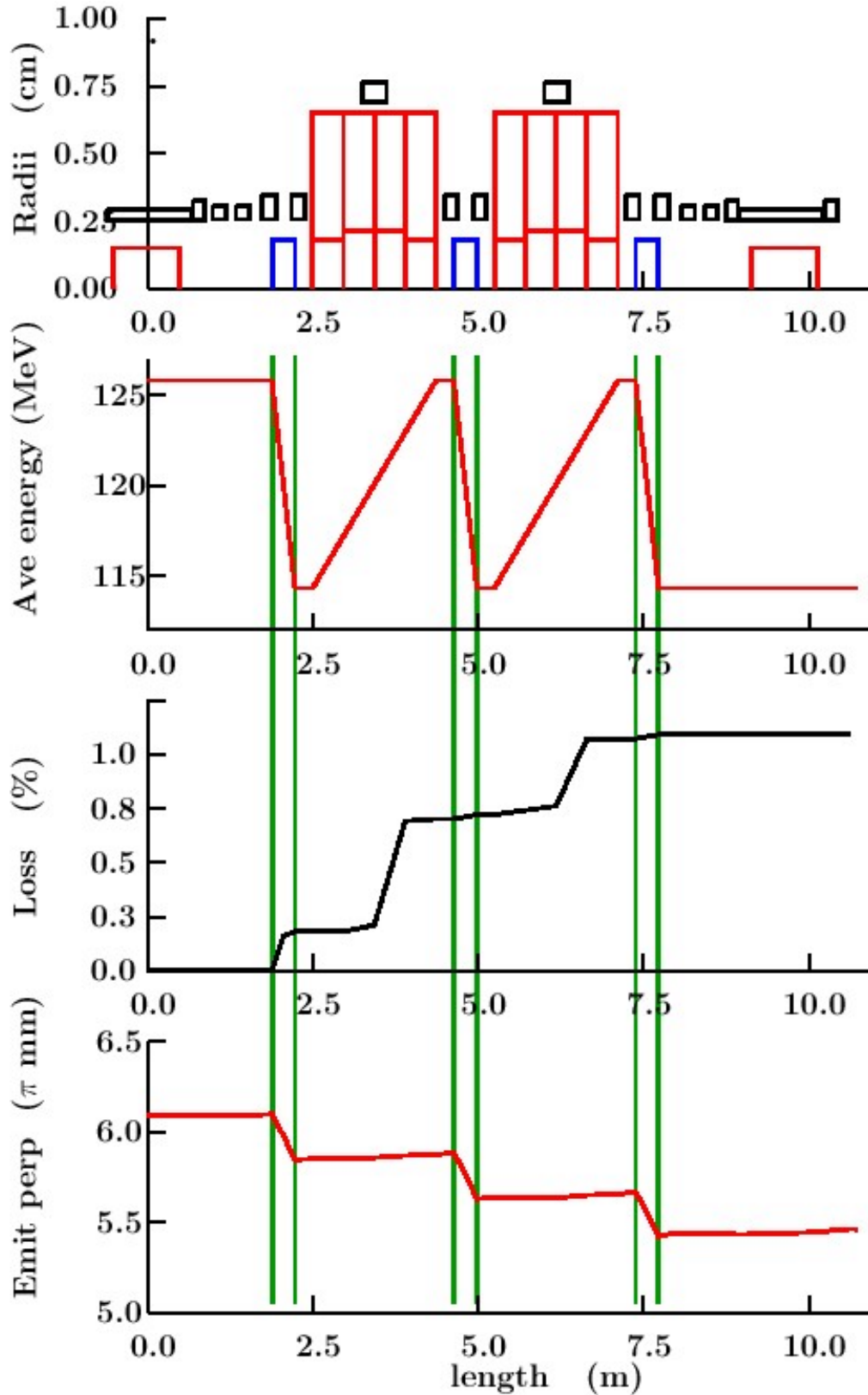
The simulation includes  $0.5 \text{ mm}$  thick aluminium absorber windows (their thickness has been increased with respect to that of Study II to mimic the effect of safety windows), and stepped beryllium RF windows (see Section 5.3). The RF fields used are those from perfect pillbox cavities. The limiting apertures are found to be located at the central iris of each 4-cavity RF assembly. The RF gradients are  $8.3 \text{ MV/m}$  and the phase is such that maximum acceleration is obtained in each cavity. An illustration of the elements of the experiment is given in Figure 3.3.



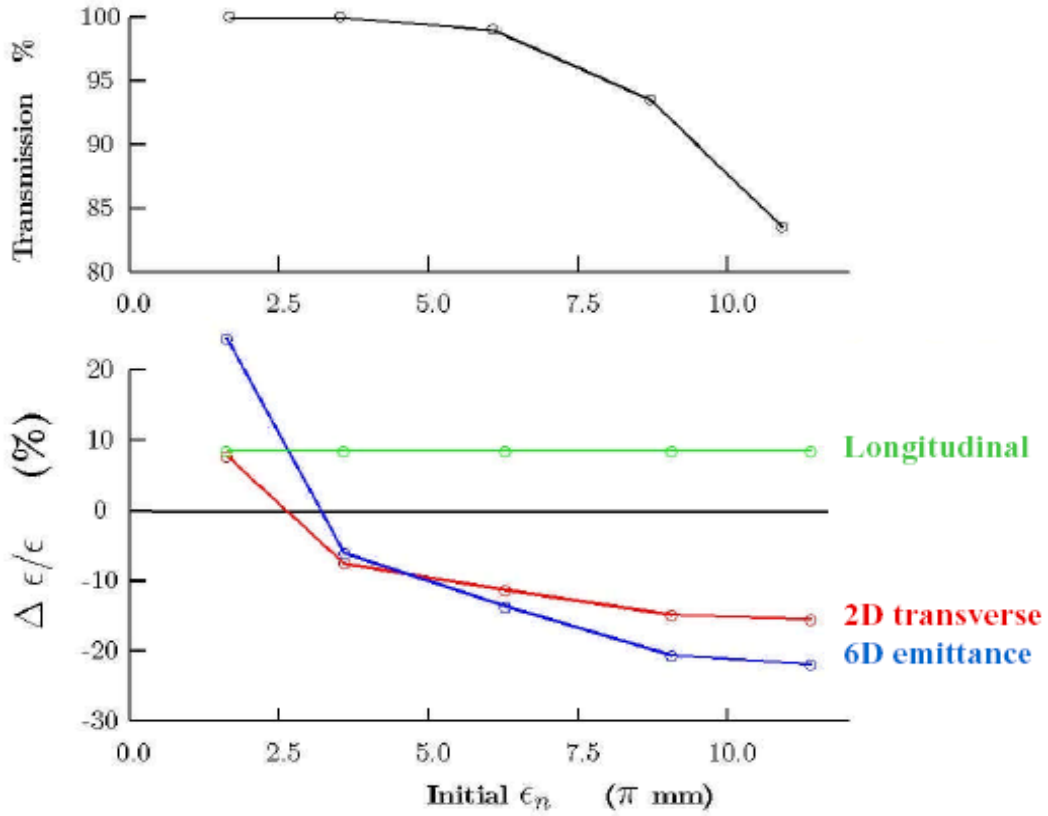
**Figure 3.3:** Description of the essential optical elements of MICE. Also shown are the rms beam radius and beam envelope for a beam of the same emittance as at the entrance of the cooling channel in Study-II.

Figure 3.4 shows the expected behaviour of the beam for a large input emittance. The kinetic energy of the beam is reduced at each passage through an absorber, and increased in the RF cavities. At the location of each of the absorbers, the normalized emittance decreases. (It does not decrease through the accelerating section, but the un-normalized emittance would.) As an extra absorber has been included, the momentum of the outgoing beam is reduced with respect to the incoming. This could be avoided by emptying the central absorber. The experiment must measure the emittances of the incoming and outgoing beams and, most importantly, their ratio, with a precision much better than the expected 10% reduction in emittance.

Figure 3.5 shows how the output emittance varies with that of the input beam. For very large input emittance, the output emittance is reduced substantially, but the transmission decreases, large-amplitude particles being lost in the channel. Nevertheless, this may not be a sign of poor performance of the device: what really matters is the variation of the number of particles within a desired acceptance. This is shown in Figure 3.6, where the cooling performance is defined by comparing the number of particles in a given acceptance (here the acceptance of a subsequent muon accelerator) before and after the cooling section. In both figures it can be seen that, as the input emittance falls, so does the cooling performance. At very low input emittance, the beam is heated rather than cooled. The equilibrium emittance is the boundary between the two cases, the value for which the input and output emittances are equal. Ideally the equilibrium emittance should be as small as possible, and the acceptance as large as possible.



**Figure 3.4:** Properties of the beam along the experiment. The narrow vertical lines depict the locations of the hydrogen absorbers. From top to bottom: the experiment layout, the average muon kinetic energy showing the typical saw-tooth, the particle losses which occur mostly at the central RF cavity iris and the 2D normalized transverse emittance, which is seen to decrease in the absorbers. These are all plotted for an input emittance of  $6.1\pi$  mm rad and muons of 200 MeV/c average momentum.



**Figure 3.5:** Transmission and decrease of emittance vs input normalized emittance. The equilibrium emittance is around  $2.5 \pi$  mm rad. The transmission plot shows that scraping becomes significant above an input emittance of  $6\pi$  mm rad.

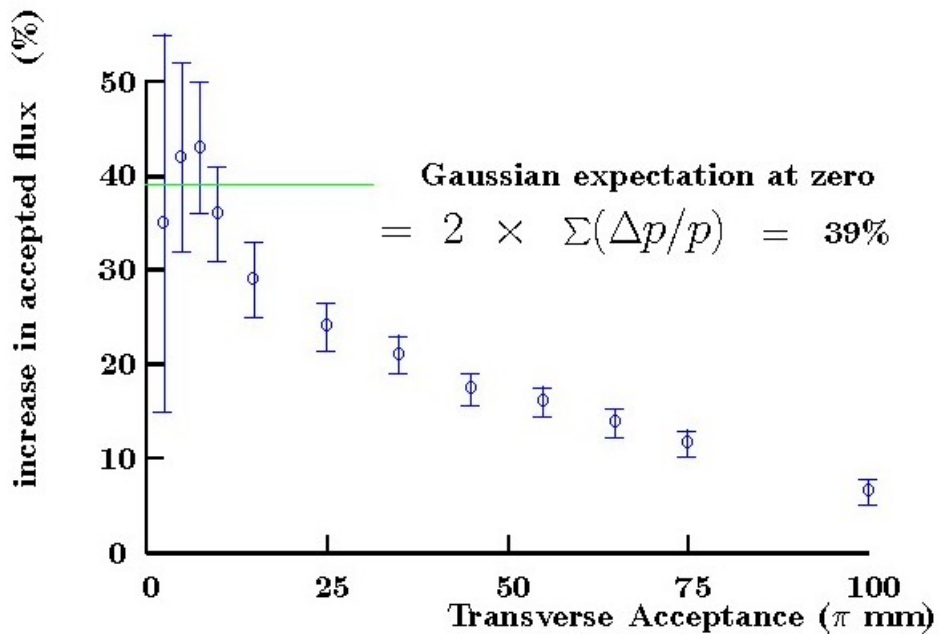


**Figure 3.6:** Cooling channel efficiency, measured as the increase in the number of muons inside a given transverse normalized acceptance, for an input beam of large emittance. For the acceptance of the Neutrino Factory muon accelerator, which is  $15\pi$  mm rad (normalized) the increase in the number of accepted muons when going through MICE would be  $\geq 30\%$ . The acceptance is 3 times larger than the rms beam size, which is proportional to the square-root of emittance; this implies a scale factor of 9 in the abscissa compared to that of Figure 3.5.

### 3.3 Measurement technique

The diagnostic devices of MICE are principally aimed at measuring, before and after the cooling channel, the volume occupied by the muon beam in six-dimensional phase space. The measurement system must not only measure emittances, but also count particles. Two techniques have been considered: i) the multi-particle method, where emittance and number of particles in any given area of phase space are determined from the global properties of a bunch; ii) the single-particle method, in which the properties of each particle are measured. The full determination of the covariance matrix in six dimensions is a delicate task in a multi-particle experiment, and the desired diagnostics would have to be developed specifically; for these reasons, the single particle-method was preferred. This technique, typical of particle physics experiments, is also one for which experimental methods already exist. Furthermore it follows exactly P. Lapostolle's definition of the rms emittance [Lap71].

In a particle-by-particle experiment, the properties of each particle are measured before and after the cooling channel in a magnetic spectrometer. Each detector measures, at given  $z$  positions, the coordinates  $x$  and  $y$  of every incident particle, and possibly the time. Momentum and angles are reconstructed by using more than one plane of measurement. For the experimental resolution not to affect the measurement of the emittance by a significant factor, the rms resolution of the measurements must be better than about 10% of the rms beam size at the equilibrium emittance in each of the six dimensions. An essential aim of MICE is to measure the equilibrium emittance precisely.

There will be only one particle travelling through the apparatus within the time window of the system. For each incident particle it will be possible to determine whether it was lost in the channel, or if it went through successfully, by the presence at an appropriate time (taking account of the travel time and fluctuations thereof) of a particle in the downstream spectrometer. In this case the losses can be very cleanly separated, particle-by-particle, from the effect of cooling.

Except for possible collective effects such as space charge, this particle-by-particle technique is equivalent to full-beam measurements, but offers several advantages:

- Correlations between parameters can be easily measured if the 6 parameters are measured on a particle-by-particle basis.
- The detailed understanding of the role of each beam parameter, and in particular of the energy, transverse momentum and RF phase (=time) of the particles, can easily be studied by making selection cuts in the ensemble of particles without making changes to the beam parameter settings.
- Software cuts based on the incoming beam make it furthermore possible to derive a variety of results with different input beam conditions from a single data set.
- Any desired input beam conditions can be reconstructed by appropriate weighting or culling of the observed particles. The weights or cuts can be determined by comparing the distribution in phase space of particles observed in the first spectrometer to the desired distribution.

Energy measurement requires a magnetic spectrometer, which could be designed in a variety of ways. Simplicity in the matching with the cooling section and the need to keep a large-emittance beam in a small physical volume led to the choice of solenoid magnets coaxial to

the cooling channel. The particle tracking inside the solenoid, obtained by measuring successive points along the trajectory, allows position, angles and the momentum of each charged particle to be determined as depicted in Figure 3.7.

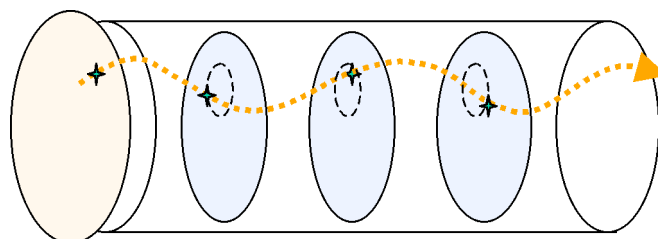


**Figure 3.7:** The space coordinates at three (or more) planes within the magnetic field and the TOF information provide a complete reconstruction of the 6D phase space coordinates for each particle.

Three  $(x,y)$  measurements in each spectrometer with particle detectors placed perpendicular to the muon beam and at three different  $z$  values are sufficient to determine the muon position, angles and momentum at the entrance and exit of the cooling channel. To obtain the best resolution and the largest dynamic range, the spectrometer length should be such that the average muon makes about  $2/3$  of a turn from the beginning to the end, i.e., about 1 m for 200 MeV/ $c$  muons in a 4 T solenoid. To avoid reconstruction ambiguities, more than three planes of detectors will be used. As indicated in Figure 3.1, the time coordinate is determined with precise time-of-flight measurements at the entrance and at the exit of the channel. Measurement of the RF phase of each incoming particle with a precision of  $5^\circ$  requires a time measurement resolution of 70 ps or better for the 201 MHz RF system, making precision time-of-flight counters compulsory.

The design of MICE, with spectrometer solenoids matched directly to the cooling cells, allows a small spectrometer to measure a large phase space and introduces no artificial energy dispersion. It has, however, one major drawback. The single-particle detectors will be exposed almost directly to a large dark current and x-ray background generated by the nearby high-gradient RF cavities. The understanding of this problem is well underway and described in Section 9. Several factors contribute to protect the tracking detectors: i) the RF cavities will be operated at a moderate gradient of 8.3 MV/m, due to the limited availability of RF power; ii) the dark-current electrons must pass through the liquid-hydrogen absorbers, which are thick enough to absorb them completely, letting through x-rays only; iii) the detectors are built of low- $Z$  material and are well able to distinguish hits from muons from those generated by x-rays. Thus, it appears that, at the RF voltage at which the MICE cavities will be operated, the performance of the detectors will not be affected. Studies of this critical issue are presented in Sections 8 and 9; these will continue with high priority.

In addition to the primary goal of measuring the space-time coordinates and the momenta of incoming and outgoing muons, the diagnostic devices should also be capable of identifying and rejecting (i) residual undecayed pions and (ii) decay electrons, in order to restrict the emittance measurement to that of the muon beam exclusively. Due to the different kinematics, even a small fraction of these backgrounds,  $> 0.1\%$ , has a detrimental effect on the emittance resolution. Pion identification can be achieved by means of a precise time-of-flight measurement over a 10 m distance prior to the first spectrometer solenoid. A 50 ps time resolution, associated with an  $(x,y)$  measurement, leads to a 99% pion rejection. The decay electrons can be identified from their specific kinematic properties with 80% efficiency. A

larger rejection is needed and requires specific electron identification with, e.g., a Cherenkov detector or a range measurement.

### 3.4 Simulations of the measurement precision

Both a fast simulation [Janot01] of the tracking process and a more complete GEANT4 simulation (G4MICE) of the diagnostic devices and of the cooling channel, as sketched in Figure 3.1, have been developed. The studies that were performed with the fast simulation were presented in the MICE Letter of Intent and only their main results are summarized here. The emittance generation, the incident particle identification, the tracking and the electron identification were studied and designed using the fast simulation, all assuming homogeneous electric and magnetic fields and perfect detectors. The fast simulation of cooling was quite approximate, but took into account most of the processes involved in the particle tracking along the cooling channel, in particular multiple scattering, energy loss in the materials with corresponding Landau fluctuations, Bremsstrahlung (for electrons), tracking in the solenoid magnetic field and decays in flight. It is considered adequate for the evaluation of statistical errors and the effects of particle mis-identification.

The G4MICE simulation has been developed as the long-term foundation of MICE software. In addition to a precise description of the material and of the electric and magnetic fields in the cooling channel, it includes a complete description of the detectors, of the generation and digitization of detector signals, and of the reconstruction algorithms. It also includes a primitive RF background generator and can be used to simulate the effects of misalignments and inefficiencies. The software is still under development and only the most essential quantities have been evaluated at present, in particular the sensitivity of the tracker to RF background as described in Section 9. An event display in which a single muon traverses the apparatus is shown in Figure 3.8.

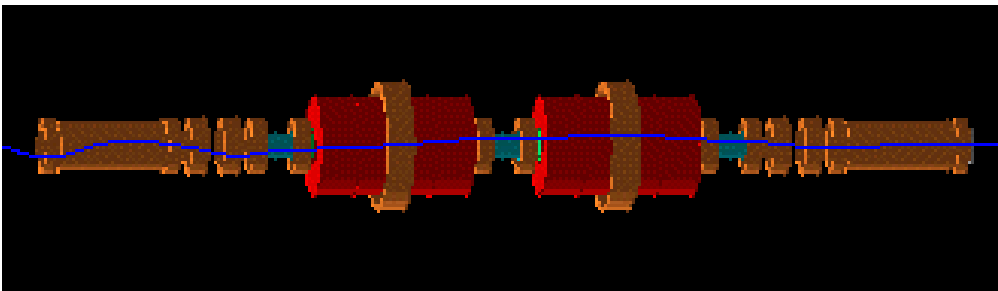


**Figure 3.8:** A single muon travelling through MICE, as seen in G4MICE.

#### 3.4.1 Statistical precision of the emittance measurement

##### *A) Transmission*

Two types of losses lead to a significant reduction in the number of particles transmitted. In the transverse plane, the requirement to fill the acceptance of the cooling channel uniformly makes it necessary to create a much larger emittance than can be transported through the

channel. Consequently, after the emittance-generating section, only about 20% of the incoming muons remain within the acceptance of the cooling section.

In the longitudinal plane, in order to emulate a real bunch, only those muons entering the first RF cavity within  $\pm 30^\circ$  of the optimal phase are considered in the emittance reduction measurement. The particles are uniformly distributed in phase, so only 16% are accepted. On the whole, about 4% of the total number of muons delivered by the beam line is actually useful for the emittance reduction measurement at full gradient.

### B) Momentum reconstruction

The resolutions in position, longitudinal and transverse momentum were estimated using the G4MICE simulation of the resolution of the scintillating fibre tracker described in Section 8. These are shown in Figures 3.9, 3.10 and 3.11. The longitudinal momentum resolution is relatively poorer for particles with a low transverse momentum, but the resolution in the longitudinal variable  $t' = E/p_z$  remains very good. The resolutions are  $\sigma(p_t) \approx 0.11$  MeV/c or  $\sigma(p/p_z) \approx 0.06\%$ , and  $\sigma(E/p_z) \approx 0.06\%$ , which are both smaller by a factor of more than 10 than the actual widths of these distributions at equilibrium emittance. This is also the case for the  $\approx 100$   $\mu\text{m}$  spatial resolution.

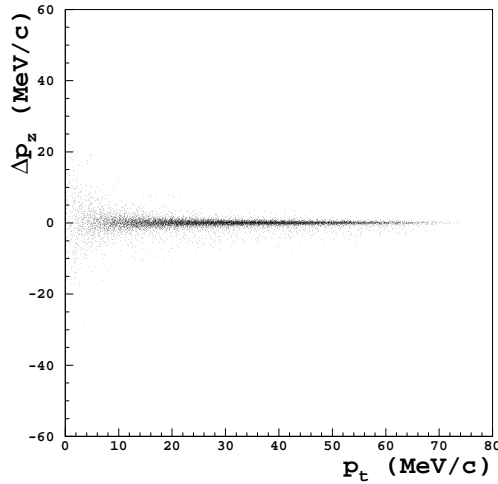


**Figure 3.9:** The measurement resolution in  $p_z$ , which varies from 1 up to 25 MeV/c rms, exhibits a strong dependence on  $p_t$ .

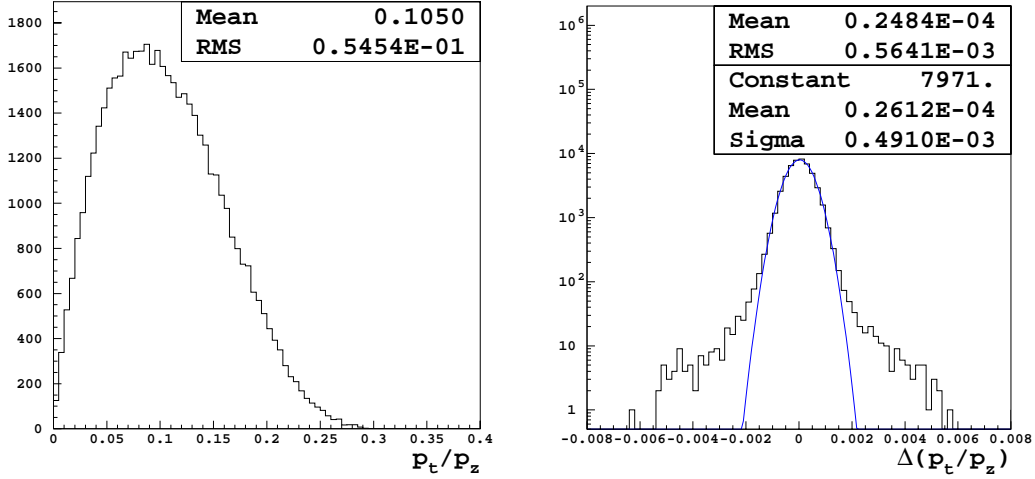


**Figure 3.10:** Resolution in transverse coordinates: (left) the distribution of transverse coordinates,  $p_t/p_z$ ; (right) the resolution in this variable  $\sigma(p_t/p_z) \approx 0.056\%$ , or  $\sigma(p_t/p_z) \approx 0.12$  MeV/c.

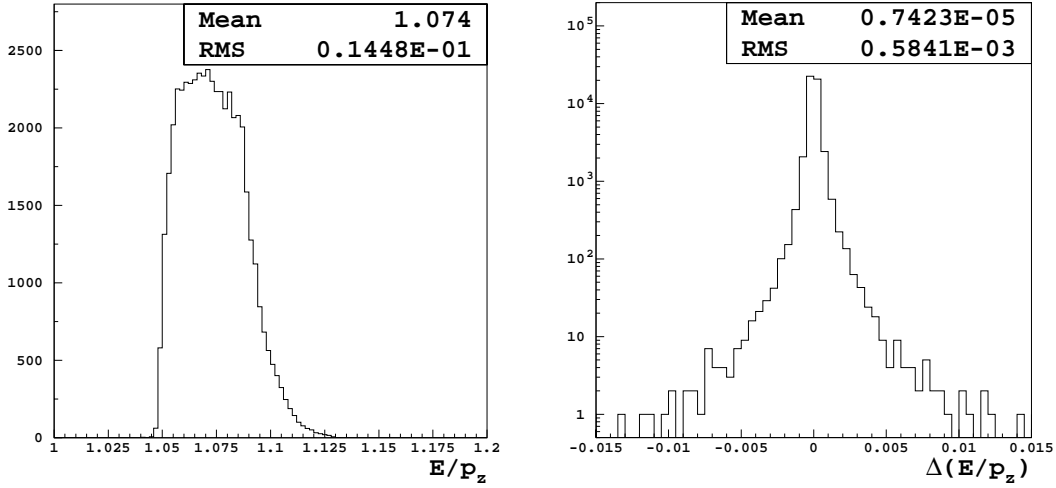


**Figure 3.11:** Resolution in longitudinal coordinates: (left) the distribution of longitudinal coordinates,  $E/p_z$ ; (right) the resolution in this variable,  $\sigma(E/p_z) \approx 0.058\%$ .

As described in Sections 7 and 8, taking into account the time structure of ISIS, the achievable RF power, the rate limitation of the detector, the losses due to the emittance generation section and the losses due to the cuts in the RF phase, one is led to a rate of good muons of about 100/s. The fast simulation has shown that a statistical precision of  $\pm 3\%$  on the ratio of the output to input 6D emittances can be performed with 1000 useful muons. The precision is even better for the transverse emittance for which a resolution of the order of 1% on the ratio of 4D transverse emittances is obtained with 1000 muons. This good performance is due to the relatively short length of the cooling channel, which ensures a strong correlation of phase-space parameters between the incoming and outgoing particles on a muon-by-muon basis. Thus the input and output emittances are strongly correlated statistically and the error on their ratio is much smaller than the relative error on each of them.

The measurement quality remains unchanged as long as the pion contamination in the accepted muon sample remains below  $10^{-3}$ . Since the TOF provides a pion rejection of 99%, this places a requirement that the pion contamination in the muon beam be kept below 10%.

Despite the limitation of the RF power source to 1 Hz, a statistical precision of  $10^{-3}$  in the ratio of emittances, which requires  $10^5$  good muons, should be achievable in less than an hour of operation.

### 3.4.2 Systematic errors

Since one of the goals of MICE will be to compare, for each configuration, the measured performance to the expected one, the systematic error sources can be divided into two categories:

- A. Errors pertaining to the prediction of the cooling effect in the cooling cell
- B. Errors stemming from a systematic difference between the incoming and outgoing measurements

The errors of class A must not affect the expected 10% cooling effect by more than  $10^{-3}$  absolute, i.e., 1% of its value. Errors in this category include:

- Uncertainties in the thickness or density of the liquid-hydrogen absorbers and other material in the beam
- Uncertainties in the value and phase of the RF fields
- Uncertainties in the value of the beta function at the location of the absorbers
- Misalignment of the optical elements
- Uncertainty in the beam energy scale

It should be stressed that the absorber thickness and RF fields only influence the energy loss or regeneration and should be measurable directly in the experiment, by comparing the energy and transverse emittance for particles on crest to those that are at the wrong RF phase. Data taken outside a MICE RF pulse will show exclusively the effect of the materials and will be of crucial relevance.

More critical is the control of the magnetic fields. For this reason MICE will be equipped with a set of magnetic measurement devices, described in Section 4, that will measure the magnetic field with a precision much better than  $10^{-3}$ . All errors of type A become more important near the equilibrium emittance.

Systematic differences between incoming and outgoing measurement devices lead to errors of class B, e.g., efficiency differences, different misalignments and possible differences in the magnetic field. The foreseen measurement of the magnetic fields with a precision well below  $10^{-3}$  will be adequate. The other errors can be measured by running the experiment with empty absorbers, or better, in a preliminary configuration with just the two spectrometers cross-checking each other (see Section 3.5).

It is believed that the systematic errors on the ratio of output to input emittance can be kept at a level of  $\pm 10^{-3}$  or better.

## 3.5 Possible experiments and time development of the apparatus

### 3.5.1 Exploration of other momenta and other optics.

Many different cooling experiments can be performed with the proposed apparatus. One of the first parameters to be varied will be the incident beam momentum. The magnets have been designed to allow exploration of momenta as high as 240 MeV/c. It will be possible to use higher momentum, but the minimum beta function obtainable will be too large to achieve the ultimate cooling performance. The limitation comes from the pairs of focusing coils, in which the current density is limited to 140 A/mm<sup>2</sup>.

MICE offers quite a bit of flexibility to vary the optics and, in particular, to decrease the value of the beta function at the absorbers. The Super-FOFO lattice used here, and in Study-II, has the property that the beta function at the absorber can be changed by adjusting the currents in the focusing and coupling coils. Figure 3.12 shows the beta functions at the absorber, as a function of momentum, for various current choices.

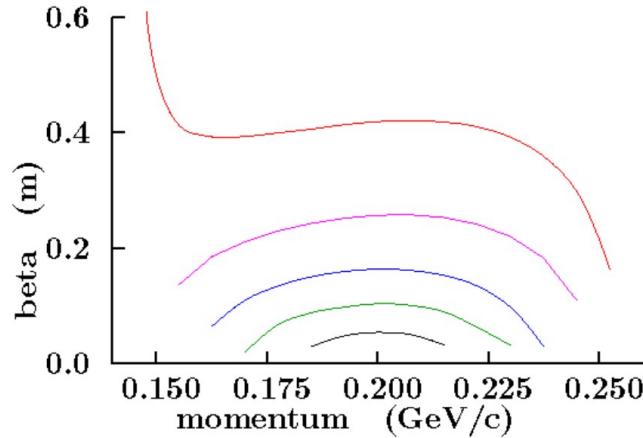


**Figure 3.12:** Beta functions at the absorber vs momentum for different current cases. The colours are explained in Table 3.2.

**Table 3.2:** Focus and coupling coil current densities for different beta functions

Focusing (A/mm <sup>2</sup> )	Coupling (A/mm <sup>2</sup> )	$\beta_{\perp}$ (cm)	$\Delta p/p$ (%)	Ref Mom (MeV/c)	Colour in Fig. 3.12
107	105	44	25	200	Red
126	93	26	20	200	Purple
<u>140</u>	67	16	17	200	Blue
<u>154</u>	50	10	14	200	Green
<u>177</u>	0	5.5	8	200	Grey

Table 3.2 shows the current densities for several different cases. At the nominal momentum the current densities for cases 3, 4, and 5 (underlined) are too high for the superconductor in the coils. However, such low beta values can still be studied if lower momenta, and correspondingly lower currents, are used. If such cases are to be studied in the experiment, the optics must be matched in each case. Having two matching coils per spectrometer solenoid allows this to be done by adjusting the currents.

**Table 3.3:** Current densities for different beta examples (for historical reasons the coil dimensions and currents differ slightly in these optical calculations from those given in Section 4)

	$p$ (MeV/c)	$\beta_{\perp}$ (cm)	$B_{\text{sol}}$ (T)	$\Delta$ (%)	Focusing (A/mm <sup>2</sup> )	Coupling (A/mm <sup>2</sup> )	Match 1 (A/mm <sup>2</sup> )	Match 2 (A/mm <sup>2</sup> )	End 1 (A/mm <sup>2</sup> )	Sol. (A/mm <sup>2</sup> )	End 2 (A/mm <sup>2</sup> )
1a	200	42	4	12	117.8	90	65.0	97.2	100	80.9	128.9
1b	240	42	4	11	141.3	108	74.3	103.6	97.9	80.9	128.9
2	200	25.4	4	12	139.7	79.3	66.7	74.4	104.4	80.9	128.9
3	175	16.7	3.5	14	136.2	58.9	53.1	47.8	97.2	70.8	112.8
4	150	10.5	3	13	128.7	37.5	40.9	14.0	89.7	60.7	96.7
5	140	5.7	2.8	10	137.2	0	20.8	-18.9	91.8	56.7	90.2

Matching has been achieved for each of these cases, with the currents and average momentum reduced where needed. The current densities in the different coils for a number of examples are given in Table 3.3. Examples 1 and 1a have the standard beta value at the absorber, but are operated at different momenta and lattice fields. To keep the spectrometer fields the same, a different match was devised for each case. Example 2 is tuned to a lower  $\beta_{\perp}$  at the standard momentum of 200 MeV/c. Examples 3, 4 and 5 have successively lower  $\beta_{\perp}$ , at momenta sufficiently reduced to remain within the capability of the coils. These examples are typical of what can be obtained using the two matching coils; other choices of beta function or momentum can also be matched.

Besides the momentum and lattice choices discussed above, different RF voltages and phases as well as different absorbers and fillings can be used. Maximum cooling will be obtained if all three absorbers are full. The experiment would reproduce the long cooling lattice most faithfully if the RF were operated at 16 MV/m (as in Study II), at a phase angle of close to 60° off crest.

The magnetic channel described above involves a total of three magnetic field flips, since the three focus coil assemblies are operated with opposite polarities. The focus pairs have been designed to be able to operate in ‘solenoid mode’ where both coils of the pair have the same polarity. This should allow the study of configurations with zero, one or two magnetic field flips along the cooling channel. The zero flip configuration, in particular, has been studied in [Franchetti02] and shown to have excellent acceptance and cooling properties over a large energy range. A full study of this configuration, in particular of the stray fields, will be needed before it can be tested.

### 3.5.2 Exploration of different absorber materials

As already mentioned, another important part of the experimental programme will be the test of different absorbers. It will be straightforward to replace the liquid hydrogen with liquid helium. The mechanical assembly of the liquid hydrogen absorbers will allow replacement of one of the absorber windows (see Section 6) by a structure supporting solid absorbers. This changeover will require a few weeks but will allow the precise measurement of cooling with different materials. The purely experimental systematic errors on the measurement of the cooling performance will largely cancel out in the comparison among different materials.

### 3.5.3 Evolution of the apparatus in time

Given that all detectors and parts of the equipment will not be ready at the same time, one can foresee a development of the experiment in time, to allow a number of preparatory stages. This leads to the scenario presented in Figure 3.12. First (step I) the beam can be tuned and characterized using a set of TOF and particle ID detectors. In step II the first spectrometer solenoid allows a first measurement of 6D emittance with high precision and comparison with the beam simulation. This should allow a systematic study of the tracker performance.

Step III is fundamental for the understanding of a broad class of systematic errors in MICE. The two spectrometers work together without any cooling device in between and should measure the same emittance value (up to the small predicted bias due to scattering in the spectrometer material). Step IV, with one focusing pair between the two spectrometers, should give a first experience with the operation of the absorber and a precise understanding of energy loss and multiple scattering in it. Several experiments with varying beta-functions and momentum can be performed with observation of cooling in normalized emittance. Starting from step V, the real goal of MICE, which is to establish the performance of a realistic cooling channel, will be addressed. Only with step VI will the full power of the experiment be reached.

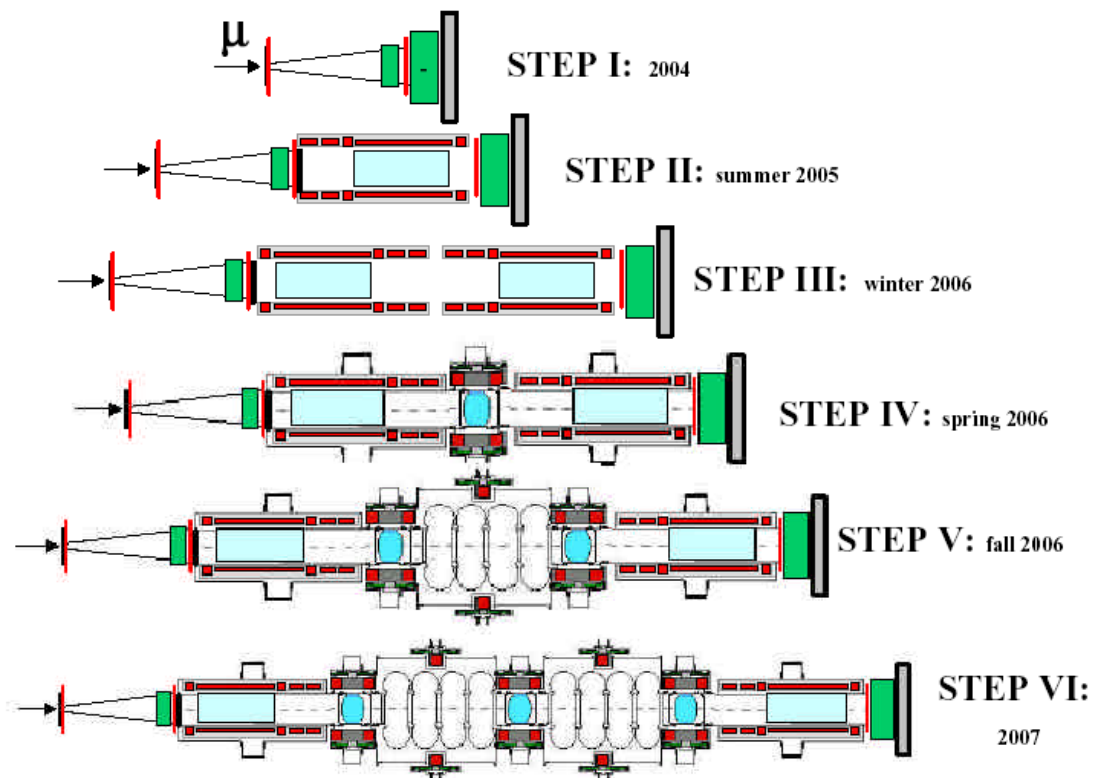


Figure 3.13: Six possible steps in the development of MICE

## 4 The Magnetic Channel

### 4.1 Layout and optics

The MICE magnetic channel [Palmer02-2] consists of seven magnet assemblies composed of eighteen superconducting solenoid coils spread over a length of nearly 11.5 m. The solenoid channel is physically symmetric about its centre, which is defined as  $z = 0$ . For the baseline operating mode of the channel, the current densities of the coils exhibit a symmetry such that  $J(-z) = -J(z)$ . The centre of the channel is the centre of a pair of focusing solenoid coils around an absorber. As one moves away from the centre, there are a coupling coil around an RF assembly, a pair of focusing coils around an absorber, a pair of matching coils, and three coils that produce a 4.0 T uniform-field region ( $\Delta B/B < 0.01$ ) for the detectors that is at least 300 mm in diameter and 1000 mm long (see Figure 3.1). Table 4.1 shows the physical parameters of the solenoid coils in half of the channel starting at the centre ( $z = 0$ ).

**Table 4.1:** Physical locations of the MICE coils in relation to the channel centre. Note that the coils at  $z < 0$  are symmetric with respect to those at  $z > 0$ .

MICE Coil	$z_1$ (m)	$z_2 - z_1$ (m)	$r_1$ (m)	$r_2 - r_1$ (m)
Focus coil #1	0.120	0.200	0.255	0.090
Coupling coil	1.195	0.360	0.690	0.071
Focus coil #2	2.430	0.200	0.255	0.090
Focus coil #3	2.870	0.200	0.255	0.090
Match coil #1	3.391	0.202	0.255	0.050
Match coil #2	3.641	0.202	0.255	0.073
Spectrometer end coil #1	3.992	0.120	0.250	0.116
Spectrometer centre coil	4.172	1.260	0.250	0.050
Spectrometer end coil #2	5.492	0.120	0.250	0.149

Note:  $z_1$  is the location of the coil end closest to the centre ( $z = 0$ );  $z_2 - z_1$  is the coil length;  $r_1$  is the coil inner radius; and  $r_2 - r_1$  is the coil thickness.

The coils listed in Table 4.1 are for the full MICE configuration. In addition MICE will be operated in the modes indicated in Figure 3.13:

1. one or two spectrometer magnets;
2. two spectrometer magnets plus a single focusing module (no RF cavities);
3. two spectrometer magnets plus two focusing modules plus a coupling coil (one 4-cavity RF assembly).

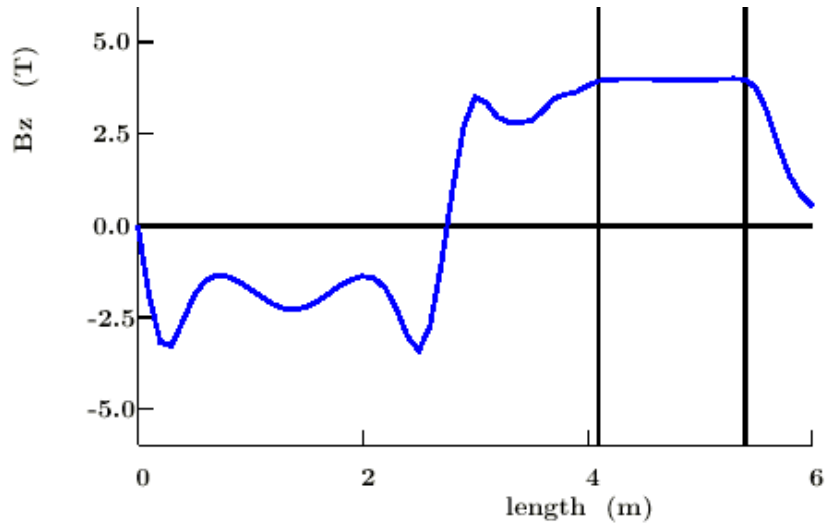
As summarized in Table 3.3, the baseline MICE channel (case 1a) operates with muons at an average momentum  $p = 200$  MeV/c and  $\beta_{\perp} = 42$  cm at the centre of the absorber (the focusing module centre). Other operating cases studied for the full MICE channel include: 1b)  $p = 240$  MeV/c,  $\beta_{\perp} = 42$  cm; 2)  $p = 200$  MeV/c,  $\beta_{\perp} = 25.4$  cm; 3)  $p = 175$  MeV/c,  $\beta_{\perp} = 16.7$  cm; 4)  $p = 150$  MeV/c,  $\beta_{\perp} = 10.5$  cm; and the final case, 5)  $p = 140$  MeV/c,  $\beta_{\perp} = 5.7$  cm. The factor that limits the momentum for cases 1b, 3, 4, and 5 is the peak field at the focusing coil superconductor. Table 4.2 shows the average current density across the coil cross section for all of the cases above and the baseline case 1a.

Figure 4.1 shows the magnetic field  $B(z)$  on axis vs distance along the channel for  $z > 0$ . The beam dynamics and simulation of the MICE channel have been described in Section 3.2. Cases that have fewer or no field flips in the focusing coils have not been studied in detail, but may be interesting to test; this possibility has been retained.

**Table 4.2:** Average muon momentum, beta at the absorber, the spectrometer field and the average current density,  $J$ , in the coils in the full MICE channel under various operating conditions.

Parameter	Case 1a	Case 1b	Case 2	Case 3	Case 4	Case 5
Average $p$ (MeV/c)	200	240	200	175	150	140
Absorber $\beta_{\perp}$ (cm)	42	42	25.4	16.7	10.4	5.7
Spectrometer $B$ (T)	4.0	4.0	4.0	3.5	3.0	2.8
Focusing $J$ (A mm <sup>-2</sup> )	107	128	127	123	117	124
Coupling $J$ (A mm <sup>-2</sup> )	106	127	93	69	44	0
Match 1 $J$ (A mm <sup>-2</sup> )	63.4	72.5	65.1	51.8	39.9	20.3
Match 2 $J$ (A mm <sup>-2</sup> )	67.1	71.5	51.4	33.0	9.66	-13.0*
End 1 $J$ (A mm <sup>-2</sup> )	64.6	63.2	67.4	62.8	57.9	59.3
Centre $J$ (A mm <sup>-2</sup> )	64.7	64.7	64.7	56.6	48.5	45.3
End 2 $J$ (A mm <sup>-2</sup> )	64.9	64.9	64.9	56.8	48.7	45.4

\*Note: In this case, this coil carries a negative current when the coils next to it carry positive currents and vice versa.



**Figure 4.1:** The magnetic field on axis in MICE for the baseline case. The field flips at  $z = 0$  and  $z = \pm 2.75$  m.

## 4.2 Design of coils

Eighteen superconducting coils generate the magnetic field for MICE. These coils are grouped in magnet assemblies of three distinct types. The cooling section consists of three focusing coil assemblies and two coupling coil assemblies. The two matching and spectrometer solenoid assemblies at the ends of the experiment each consist of two matching coils and three coils that generate a uniform solenoid field (better than 1%) that is 1000 mm long and 300 mm in diameter [Green02].

Each focusing magnet assembly consists of a pair of superconducting coils, separated by 240 mm along the beam. The coils are 200 mm long, 90 mm thick and have an inside diameter of 510 mm. Since the two coils are normally powered at opposite polarity to produce a magnetic field flip, they are assembled as a single unit, so that the magnetic forces (up to 2.3 MN) can be carried by the cold support structure that holds them in the correct position. Since the experiment may be operated with these coils operating at the same polarity, the coil support structure must also be capable of carrying forces (up to 1 MN) that will pull the two coils together. The design of these coils is further complicated by the fact that they must be assembled around the liquid-cryogen (hydrogen or helium) absorber. Piping for the absorber will go between the coils and through the coil support structure. Design parameters of the focusing solenoids are given in Table 4.3. A schematic representation of the focusing coils, the absorber, the RF cavity vessel and the coupling coils is shown in Figure 4.2. Each coil in the focus pair will have its own leads, so that each focusing coil can be operated at either polarity. It has been assumed that all three focusing sets will be operated in series from a single 300 A, 10 V power supply. The maximum longitudinal forces that must be carried by the cold-mass support system are 0.88 MN during the expected operating and off-normal modes of the experiment.

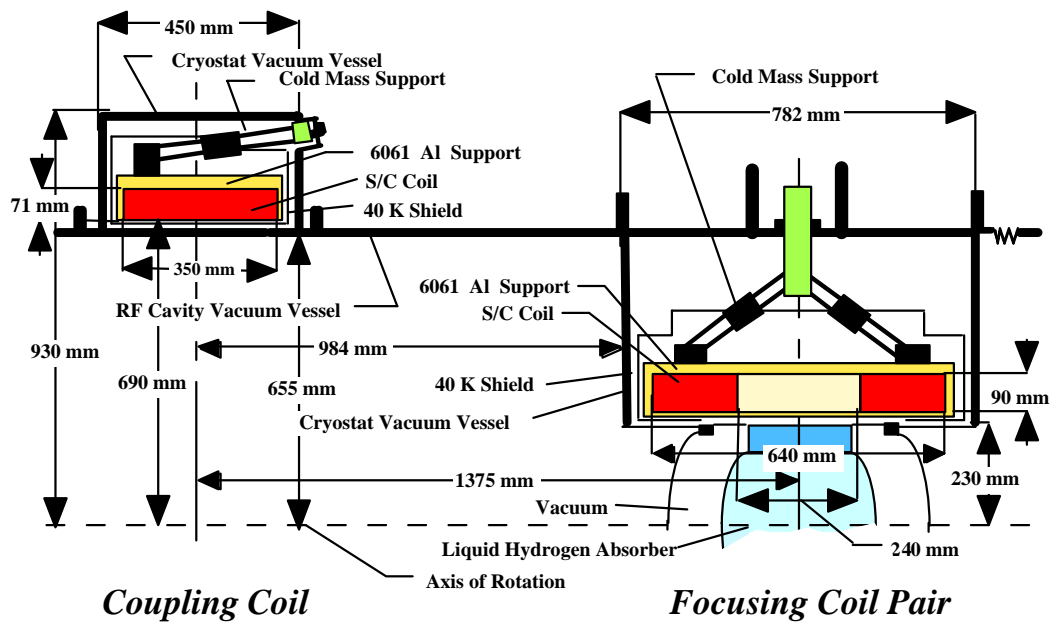


**Figure 4.2:** Schematic representation of the focusing and coupling coils with respect to the cryogenic absorber assembly.

The liquid-cryogen absorber and the focusing coil superconducting magnet will share a common insulating vacuum vessel. As a result, the cryostat vacuum vessel must be designed to the same safety standards required for the vacuum vessel for a liquid-hydrogen cryostat. The cryostat vacuum vessel for the absorber will be surrounded by an inert gas atmosphere (on the outside surface of the focusing magnet cryostat vacuum vessel) or a separate vacuum (the RF cavity vacuum), so that small air leaks in the cryostat vacuum vessel do not cause oxygen to freeze on the 20 K and 4 K surfaces within the cryostat. The outer window of the absorber will have vacuum on both sides and will be at a temperature above 50 K, so that oxygen does not freeze on this window. As a result, the potential for freezing oxygen on the absorber and the superconducting magnet will be entirely eliminated.

**Table 4.3:** Focusing and coupling coil parameters

Parameter	Focusing coil	Coupling coil
Inner coil radius (mm)	255	690
Coil thickness (mm)	90	71
Coil length (mm)	200	360
Coil average $J$ ( $A\ mm^{-2}$ )*	106.67	105.63
Number of coils	2	1
Distance between coils (mm)	240	-NA-
Number of layers	66	52
Number of turns per layer	121	218
Design current (A)*	240.3	238.2
Self inductance (H)*	~45	~230
Stored energy (MJ)*	~1.3	~6.5
Peak field in the coil (T)*	6.27	5.45
Design temperature margin (K)	~1.4	~1.8
Cold inter-coil force (MN)*	1.55	-NA-
Peak warm-to-cold force (MN)	<0.75	<0.10

\*For the standard channel (case 1a) with  $p = 200\ MeV/c$  and  $\beta_{\perp} = 42\ cm$

The coupling solenoid assembly consists of a single superconducting coil that surrounds the 201 MHz RF cavities. The coupling coil cryostat surrounds the large vacuum vessel that contains the four RF cavities. Its vacuum vessel is separate from that of the RF cavities. The coupling coil has inner diameter 1380 mm, length 350 mm and thickness 71 mm. The RF cavity vacuum vessel connects the coupling coil vacuum vessel to the focusing coil vacuum vessel at each end of the RF cavity assembly. Design parameters of the coupling solenoids are shown in Table 4.3, and the coupling coil and its supports are indicated in Figure 4.2. It has been assumed that both coupling solenoids will be operated in series from a single 300 A, 10 V power supply. The maximum longitudinal forces that are to be carried by the cold-mass support system are 0.12 MN during the expected operating and off-normal modes of the experiment.

The superconductor proposed for the focusing and coupling coils has the following parameters [Green00]:

1. the conductor is a standard MRI magnet conductor with a copper-to-superconductor ratio of four;
2. the copper in the conductor has a minimum residual resistance ratio (RRR) of 75;
3. each conductor consists of 55 filaments that are 78  $\mu m$  in diameter;
4. the conductor twist pitch is 12.7 mm;
5. the dimensions of the insulated conductor are  $1.0 \times 1.65\ mm$ , and the conductor is rounded to prevent insulation cracking;
6. the design critical current for the conductor is 760 A at 4.2 K and 5.0 T.

Each matching and spectrometer coil assembly consists of five coils that fit into a cryostat that is 2650 mm long [Farinon02]. The two matching coils adjust the magnetic field profile between the spectrometer and focusing coils to match the muon beam. The three spectrometer solenoid coils generate a uniform magnetic field (good to better than 1%) in the detector volume, which is 1000 mm long and 300 mm in diameter. The matching and spectrometer

magnet coils shown in Figure 4.3 (parameters given in Table 4.4) are designed to operate using a single 300 A, 10 V power supply when MICE operates in the baseline configuration. When MICE runs in other experimental modes as many as four 300 A power supplies will be needed to operate a single matching and spectrometer coil set. The longitudinal forces that must be carried by the matching and spectrometer magnet cold-mass support system are less than 0.80 MN during the expected operating and off-normal modes of the experiment.

The superconductor proposed for the matching and spectrometer coils has the following parameters:

1. the conductor is a standard MRI magnet conductor with a copper-to-superconductor ratio of six;
2. the copper in the conductor has a minimum RRR of 75;
3. each conductor consists of 92 filaments that are 80  $\mu\text{m}$  in diameter;
4. the conductor is twisted;
5. the dimensions of the insulated conductor are  $1.65 \times 2.40$  mm, and the conductor ends are rounded to prevent insulation cracking;
6. the design critical current for the conductor is 950 A at 4.2 K and 5.0 T.

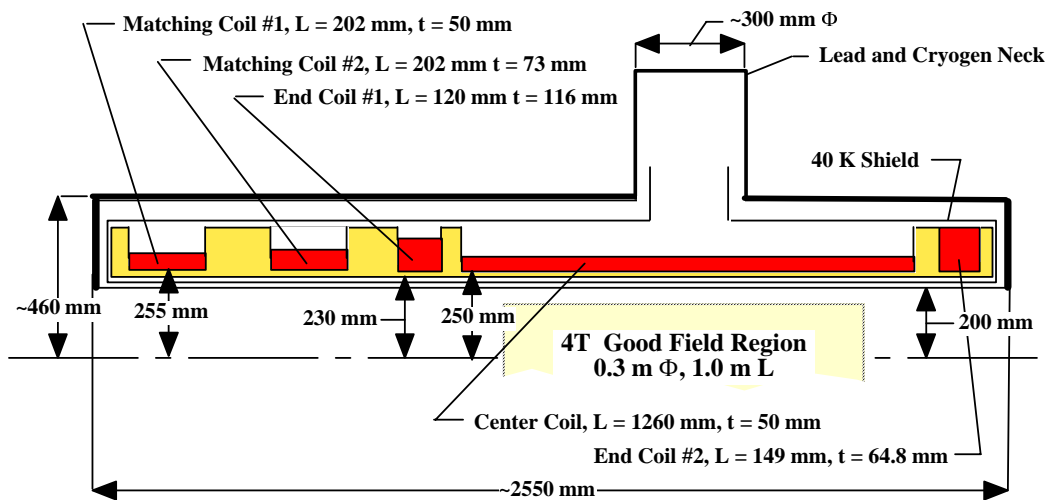


**Figure 4.3:** A cross section of the matching and spectrometer solenoid showing the positions of the five coils.

**Table 4.4:** Matching and spectrometer magnet parameters

Parameter	Match 1	Match 2	End 1	Solenoid	End 2
Inner coil radius (mm)	255	255	250	250	250
Coil thickness (mm)	50	73	116	50	149
Coil length (mm)	202	202	120	1260	120
Coil average $J$ (A mm <sup>-2</sup> )	63.4	67.1	64.6	64.7	64.9
Number of layers per coil	30	44	70	30	90
Number of turns per layer	84	84	50	525	50
Design current (A)*	254.1	267.8	257.0	258.9	257.9
Coil self inductance (H)*	3.9	8.8	8.9	46.2	14.9
Coil stored energy (MJ)*	0.13	0.32	0.29	1.55	0.50
Peak field in coil (T)*	3.4	4.4	4.9	4.2	5.0
Temperature margin (K)*	>2.5	>2	>1.8	>2	>1.8

The peak inter-coil force within the cold mass is 1.35 MN. The peak cold to warm force is about 0.76 MN.

\* For the standard case 1a with  $p = 200$  MeV/c and  $\beta_{\perp} = 42$  cm

Quench protection of the MICE magnets is designed to be passive. Where applicable, there are diodes and resistors across the coils to shunt current out of the coil as it turns normal. Quench-back is an important part of the quench protection of the coupling and focusing coils. Since the magnets are tied together inductively, a quench in one MICE magnet coil will likely trigger a quench in the other magnets of the string.

### 4.3 Cryogenic services to the magnet and absorber

The proposed cryogenic cooling system for MICE uses a single liquid-helium refrigerator to cool both the superconducting magnets and the liquid-hydrogen absorbers [Green02-1]. It is proposed that the helium refrigerator cold box deliver two-phase helium at 4.4 K at the saturated-liquid condition and 14 K helium at a pressure of 14 to 18 bar. The 4.4 K helium will be used to cool the seven superconducting magnets in the MICE magnet string. The 14 K helium will be used to cool the liquid-hydrogen absorbers, the magnet shields, and the gas-cooled electrical leads that go from about 50 K to room temperature. Helium returns to the refrigerator from the magnet string at 4.3 K. The helium gas from the absorbers returns to the refrigerator as a gas at 18 K or lower. The helium that will be used to cool the magnet shields and leads will bypass the refrigerator cold box and return to the refrigerator compressor at about 300 K. Table 4.5 shows the projected heat loads for the magnets, the absorbers, and the cryogenic VLPC photodetectors for the scintillating fibre detectors (see Section 8.4.1).

The superconducting coils for the MICE magnets will be cooled by conduction from the magnet coil support structure. The coil support structure will be cooled by two-phase helium in cooling tubes having an inner diameter of about 10 mm. All of the solenoid magnets will be cooled in series using a single cooling circuit that goes from the refrigerator control cryostat through the magnets and back to the refrigerator (see Figure 4.4). The volume of liquid helium in the solenoids will be very low (a few litres). The advantages of two-phase helium cooling of the magnets are: 1) the cool-down of the magnet string is straightforward and well controlled; 2) the overall mass of a tubular-cooled magnet and its cryostat is less than the mass of a magnet with helium-bath cooling; 3) the amount of helium in contact with the magnet coil during a quench is limited to the amount of helium in the cooling tube; 4) helium services to the superconducting magnets can come into the cryostat from any

direction. The total refrigeration at 4.3 K is estimated to be about 40 W (including the helium transfer lines). The mass flow in the two-phase flow circuit is about  $5 \text{ g s}^{-1}$ .

The hydrogen absorbers are cooled in parallel from a header that contains helium gas at 14 K. The gas used to cool the absorber returns to the refrigerator cold box at a temperature no higher than 18 K. The control valves that go onto each of the absorbers will control the helium flow depending on the desired temperature of the cryogen in the absorber and the heat entering the absorber fluid. In addition to cooling the absorber, the 14 K helium cools the magnet shields, the cold-mass-support thermal intercepts, and the upper end of the high-temperature-superconductor (HTS) leads that supply current to the magnet coils. Since the flow in the shield circuit is rather low, the same gas is used to cool the gas-cooled leads that carry current from room temperature to the top of the HTS leads. This gas is returned to the refrigerator compressor intake at 300 K. A schematic of the cooling system for a liquid hydrogen absorber and its focusing magnet is shown in Figure 4.5.

The refrigerator that cools the superconducting magnets and the absorbers also provides cooling at 5 K for the VLPC photodetectors for the scintillating fibre tracker. From 100 to 150 W of cooling at 5 K is required to cool the VLPC system.

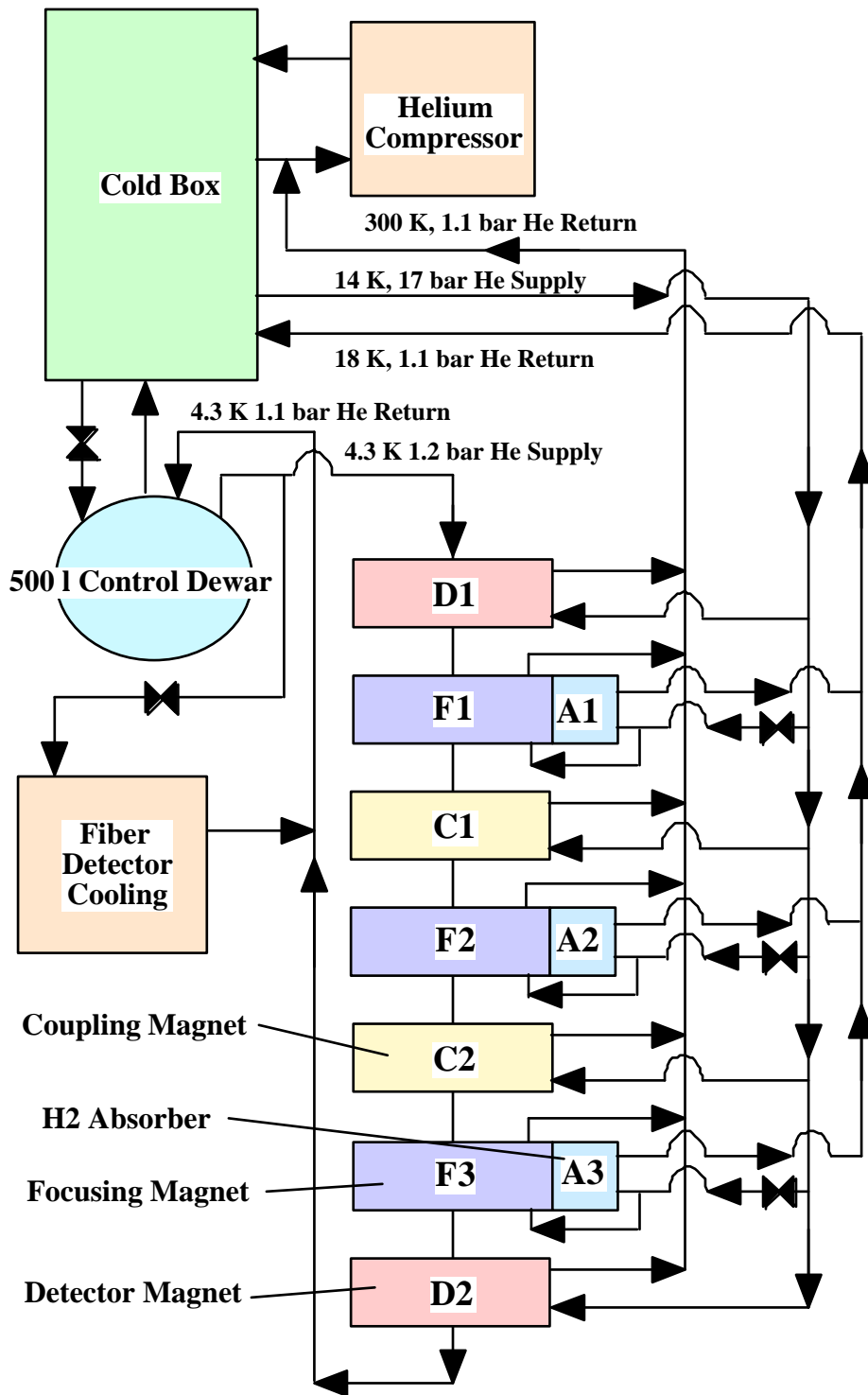


**Figure 4.4:** A simplified schematic diagram of the helium cryogenic cooling system for MICE. The boxes labelled D1 and D2 are spectrometer magnets; the boxes labelled F1, F2 and F3 are focusing magnets; and the boxes labelled C1 and C2 are coupling solenoids. The absorbers A1, A2 and A3 are shown in the same cryostat vacuum vessel as the focusing solenoids. A liquid helium absorber would be cooled from the 4.4 K two-phase cooling circuit, which is not shown. A separate 4.4 K circuit cools the scintillating fibre VLPC photodetectors to about 5 K

**Table 4.5:** Heat loads to the MICE cold box at various temperatures for the liquid-hydrogen absorbers

Parameter	Heat load at 4.4 K [W]	Heat load at 14 K [W]	Lead He flow at 14 K [g s <sup>-1</sup> ]*
<b>Superconducting magnets</b>			
Two coupling magnets	3.2	30.3	0.14
Three focusing magnets	5.2	21.9	0.22
Two spectrometer magnets	2.8	13.8	0.30
Liquid-helium transfer line	27.4	—	—
Total heat load and mass flow	38.6	66.6	0.66
<b>Liquid-hydrogen absorbers</b>			
Radiation and conduction load	—	99	—
Beam and dark current heating allowance	—	60	—
Convection heaters	—	90	—
Helium transfer lines	—	41	—
Heat load to the 14 K helium gas	—	290	—
Sensors for the scintillating fibre detector sensors	~150 W**	—	—

\* Gas flowing up the magnet leads and returning to the refrigerator at 300 K.

\*\* This leads to a heat load of 1 kW at 80 K, which is removed by 20 litres / hour of LN<sub>2</sub>.

**Table 4.6:** Heat loads for the fibre readout

Liquid-nitrogen cooling for the fibre detectors =	1000 W @ 80 K = ~20 l/hr
Equivalent refrigeration at 4.4 K and refrigerator input power	
Equivalent 4.4 K refrigeration needed [W]	307
Design size of the equivalent 4.4 K refrigerator [W]	≈420
Total installed input power for the compressors [kW]	≈300

The calculated refrigeration load for MICE is 190 W at 4.4 K (including the heat load to the scintillating fibre photodetectors), plus 290 W from 14 to 18 K plus 0.66 g/s of helium gas taken from the cold box at 14 K and returned to the compressor intake at 293 K. This refrigeration is equivalent to about 307 W at 4.4 K. To allow for errors and additional margin, a 420 W, 4.4 K helium refrigerator should be installed. The installed power needed for the MICE refrigeration system should be about 300 kW.

If liquid helium is used in the absorbers instead of liquid hydrogen, the required minimum 4.4 K helium refrigeration plant capacity will go up from 307 W to about 360 W. It would be prudent, therefore, to increase the size of the helium refrigerator cold box from 420 W at 4.4 K to about 450 W at 4.4 K to allow the option of operating the MICE absorbers with liquid helium in place of liquid hydrogen. The refrigerator currently costed in Section 11 is a Linde TCF50, which has 500 W of cooling at 4.4 K and hence is suitable for either absorber. As most of the power that goes into the compressor is extracted as heat, the required water-cooling capacity for the refrigerator compressors will equal the installed power for the refrigeration system.



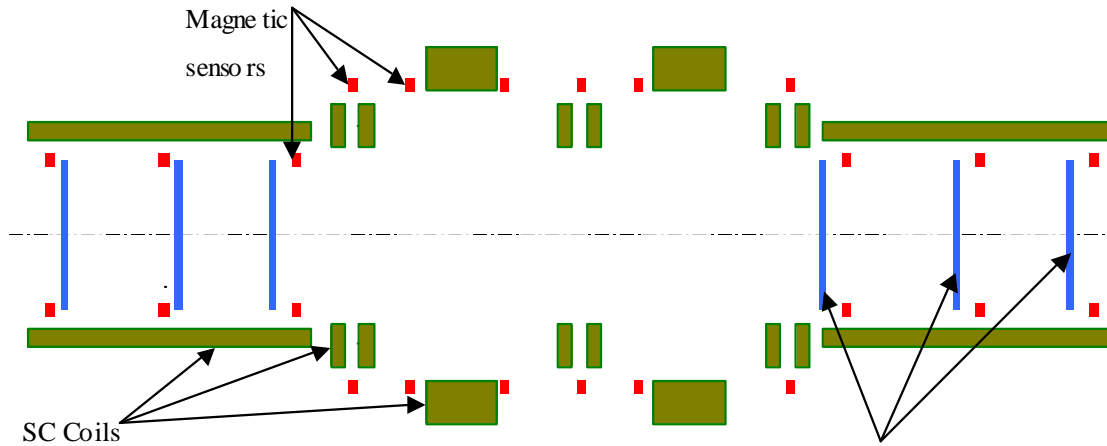


**Figure 4.6:** A schematic of the positions of magnetic sensors with respect to the magnet coils in MICE.

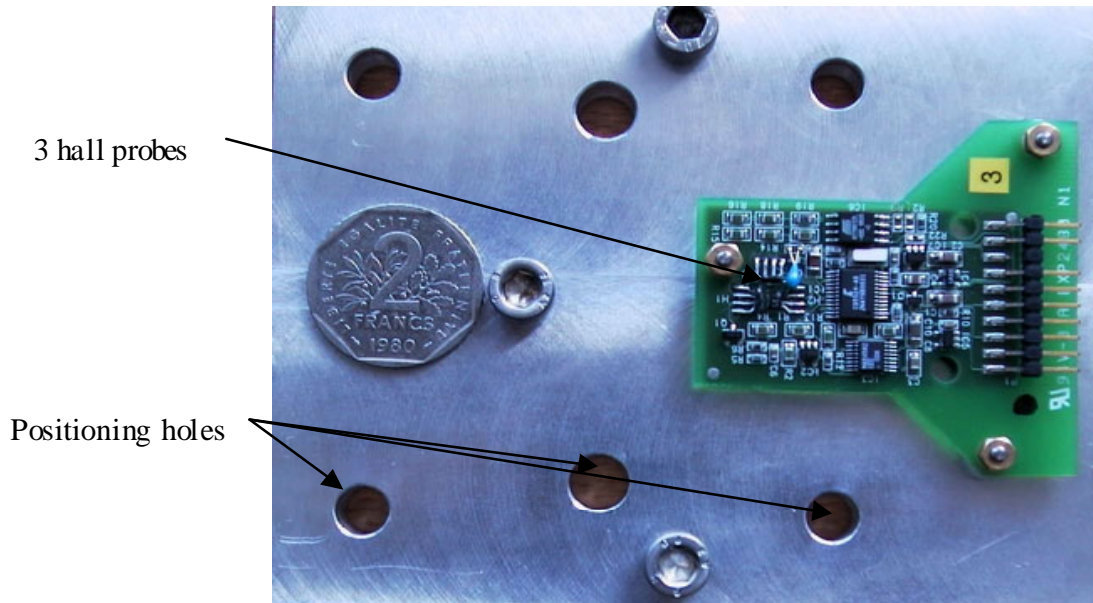
The magnetic measurement scheme proposed for MICE has already been developed for the ATLAS experiment at CERN [Chevalier02] and most of the components exist. The sensors have been developed by CERN and NIKHEF and are based on 3D Hall probes with their associated electronics. Figure 4.7 is a picture of such a sensor. The sensors for MICE must operate in magnetic fields up to 4.5 T. This requires an upgrade of the present ATLAS design, following a development already under way for the CMS experiment.

Table 4.7 summarizes the characteristics of the probes and gives the level of precision needed in their positioning. To reach the maximum precision, calibration of the sensors will be performed against NMR probes, for all three spatial orientations, in a 4 T field having a homogeneity of  $10^{-5}$  T over  $0.1 \text{ m}^3$ . In such a case, if one knows the position of the superconducting coil within 1 mm, the axis of the magnetic system can be determined with an accuracy of around 0.2 mm.

The method for making the magnetic measurement once the magnet system is assembled is as follows: 1) survey the position of each sensor around the experiment with a theodolite; 2) power each coil separately to reconstruct its respective position in space knowing its current and geometrical shape; 3) power the whole experiment and make the field reconstruction in the experiment knowing the currents, the positions of the sensors and magnets, and the relative displacements of the magnets due to their attraction or repulsion.

**Table 4.7:** Characteristics of the Hall Effect sensors

	<b>MICE requirement</b>
Magnetic field (T)	4.5
Precision ( $\Delta B/B$ )	$2 \times 10^{-4}$
Positioning precision (mm)	1
Angular positioning precision (mrad)	2



**Figure 4.7:** A picture of one ATLAS magnetic sensor with its electronics.

## 4.5 Responsibilities, costs and time line

A summary of the cost and schedule for the magnet fabrication can be found in Section 11 of this proposal. The assumptions that went into the magnet cost estimate and time line are as follows:

- 1) Three different groups will build the magnets. The coupling magnets will be fabricated in the United States; the focusing magnets will be fabricated in the United Kingdom; the matching/spectrometer solenoids will be fabricated in Italy. The three types of magnets will use similar but not identical superconductor. It is expected that the current needed to power all of the coils is less than 300 A. The magnet time line assumes that each step will take the time allotted. In that sense the time line is 'success oriented'. It assumes that the fabrication contracts for all three focusing magnets will be released at the same time, so that superconductor and parts can be purchased simultaneously.
- 2) The focusing magnet cost estimate includes 150 k€ to integrate and install the hydrogen absorbers into the superconducting coil package. The cost estimate also includes the installation of the inert gas shield on the outside of the focusing magnet cryostat, but not onto the rest of the MICE vacuum vessel. Included in the focusing coil cost is the cost of a cold-mass support system that can carry an 80 tonne force along the axis of the magnet. The focusing coil cryostat shall have flanges that allow it to be connected to the RF cavity vacuum vessel and the spectrometer solenoid cryostat. Longitudinal magnetic forces shall be carried through this flange. Included in the focusing magnet cost estimate are two sets of HTS and gas cooled leads so that the focusing coils can either be operated in the solenoid mode (with no field flip) or the gradient mode (with a field flip). The cost of the absorbers and the absorber features that permit a solid absorber to be used in place of a liquid absorber will be borne by the absorber fabrication group.

- 3) The coupling coil cost estimate includes the flanges for integrating the coupling solenoid cryostat with the RF cavity vacuum vessel. The cost of the RF cavity vacuum vessel is not included in the cost of the coupling solenoids. Longitudinal magnetic forces shall be carried through this flange to the adjacent focusing coil cryostats. The coupling cold-mass support system is designed for a 20 tonne force in any direction.
- 4) The spectrometer magnet cost includes the cost of the five coils, the coil support, and four sets of HTS and gas-cooled leads to supply the five coils with current. The cold-mass support system shall be designed for a longitudinal force of 115 tonnes and a transverse force of at least 15 tonnes. The spectrometer magnet cryostat shall have a flange that allows it to be connected to the focusing coil cryostat. The longitudinal magnetic forces shall be carried through this flange.
- 5) The refrigeration system cost includes the helium refrigerator cold box, all helium transfer lines, all helium control and shut-off valves, a refrigeration control system, the two-phase-helium cryogenic system control cryostat and all helium bypass piping. The refrigeration system cost does not include any component for the liquid-hydrogen system, the hydrogen safety system, or the hydrogen gas-handling system. The costs associated with handling hydrogen are part of the absorber and hydrogen safety system costs. The costs of providing the absorber with helium gas at 14 K or two-phase helium are included in the helium cryogenic system cost. It is assumed that the helium refrigerator, the helium cryogenic transfer line system, and the helium gas-handling system will be provided by RAL.
- 6) The cost estimate for the magnet power supplies assumes that the two coupling coils will be powered with the same power supply (300 A at 10 V). The three focusing solenoid systems will be powered primarily with a single 300 A power supply. However, small power supplies (<100 A) may be used to tune the focusing solenoids at the ends of the experiment. Each spectrometer solenoid is assumed to require four 300 A, 10 V power supplies. The power supply estimate includes the power supply cables and cable trays. The power supply system cost includes eleven 300 A power supplies, four 100 A power supplies, and the controllers that control the magnet charge rate and maintain a constant current once the magnets have been charged. The power supplies will be purchased by the groups who supply the magnets from a common specification that applies to all of the magnet power supplies.
- 7) Magnetic measurement costs include the 36 three-axis magnetic field measuring sensors good to 4.5 T, the magnetic sensor fixtures, the computer for storing and analysing the field measurement data, and the costs associated with surveying the magnetic field probe position and doing the magnetic measurements. The probes will be provided by NIKHEF, and the measurement strategy and analysis by CEA/Saclay.
- 8) Magnet safety, cryogenic system safety, and electrical safety systems associated with powering the magnets, cooling the magnets and absorbers, and measuring their magnetic fields will be the responsibility of RAL.

## 5 The RF System

### 5.1 Introduction

Eight 201-MHz RF cavities, in two 4-cavity assemblies, are needed in the cooling section for the MICE experiment. The cavity design is based on that for the Study-II cooling channel, a 2.75-m lattice with four cavities per cell. Due to the (financial) limitation of having only 8 MW of RF power available, the MICE cavities will be operating at a gradient of about 8 MV/m (compared with the 16 MV/m specification for the Study-II cooling channel), and thus provide a maximum RF voltage of 21 MV. As the cavities must operate in a strong magnetic field, normal conducting technology must be used. In addition, to accommodate the large transverse size of the muon beam, a large beam aperture is needed. These somewhat conflicting requirements make it very inefficient to use a conventional open-iris cavity geometry, as the cavity shunt impedance decreases significantly with increasing beam iris size. The cavity shape chosen is based on a slightly reentrant rounded profile with a very large beam aperture and a small nose cone. To achieve high shunt impedance, the beam aperture is terminated electromagnetically using thin beryllium foils ('windows') or thin-walled Al tubes ('grids'). These Be windows or grids can be almost transparent for the muons, while presenting a conducting boundary for the RF fields.

The two 4-cavity assemblies are shown installed in a representation of the MICE cooling section in Figure 5.1, where the locations for superconducting solenoid magnets and absorbers are also indicated. The electrical, mechanical and thermal requirements of the cavities and possible iris structures are described in this section.

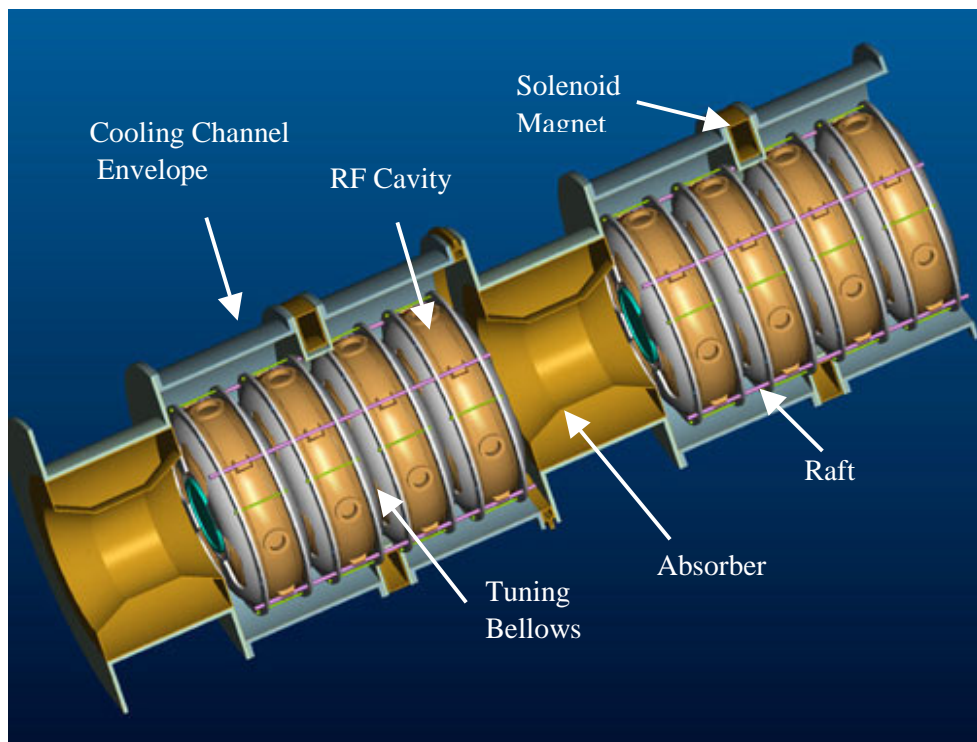


**Figure 5.1:** A pair of 4-cavity assemblies in the MICE cooling section.

## 5.2 The cavity geometry

The MICE cavity has the same shape as that for the Study-II design, with a slightly reentrant rounded profile and a large beam aperture, as shown in Figure 5.2. The cavity geometry is optimized in terms of minimizing peak surface field and in terms of accommodating either windows or grids. The cavity length is chosen to give the maximum shunt impedance for a given space. As noted, thin beryllium foils or grids of thin-walled aluminium tubes will be used to close the beam iris. In the Study-II design, the central cavities in each cooling cell had 21 cm radius beam irises, while the end cavity irises were reduced to 18 cm radius to take advantage of the lower beta function close to the absorbers. By design, the irises are thick enough to accommodate either a pair of foils or a grid of tubes. For MICE, all cavities will have the same beam iris dimension, 21-cm radius, and they are terminated by Be foils (foils with stepped thickness may be used to minimize scattering of the core of the beam).

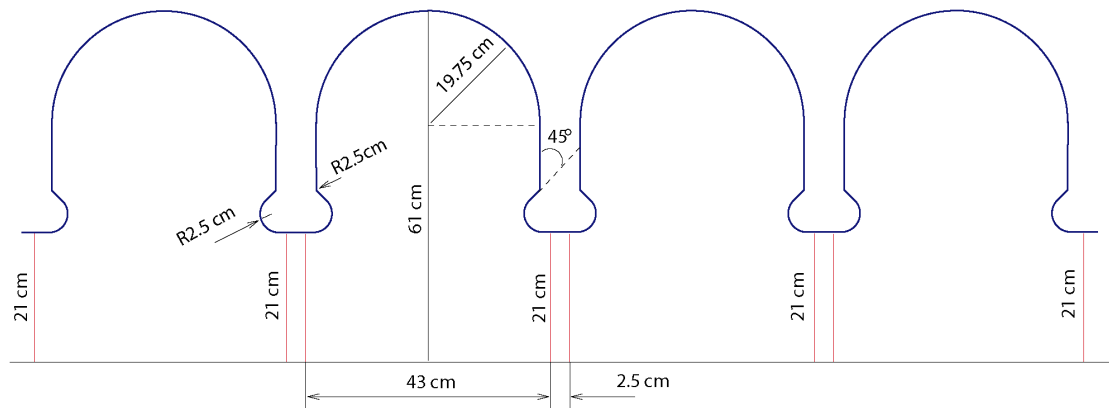


**Figure 5.2:** 201-MHz RF cavity profile for MICE.

The cavity profile allows space between the cavities for the tuner mechanism and for mounting the Be windows. Any practical assembly of foils (or grids) requires some space for installation and access. A minimum spacing of 25 mm between cavities is used, as indicated in Figure 5.2. This is, in fact, the minimum required annular frame thickness for the pre-stressed Be windows. Based on previous experiments with pre-stressed Be foils in an 805-MHz cavity, the thickness of the foils was chosen such that the temperature rise at the centre of the foil is below the point at which the foil starts buckling. Table 5.1 lists the main cavity parameters, and Table 5.2 gives dimensions of the stepped foils and the thermally equivalent flat-foil thickness.

**Table 5.1:** Main calculated cavity parameters for the 201-MHz cavity.

Parameter	Value	Unit
Radius	61.0	cm
Length	43.0	cm
$RT^2$	22	MΩ/m
Quality factor, $Q_0$	55,000	

## 5.3 Terminations of the beam iris

Due to the short lifetime of muons, the cooling channel length must be kept to a minimum. This calls for use of a high-gradient RF accelerating structure in the channel. As already

noted, given the large transverse size of a muon beam, it is obvious that accommodating it using conventional open-iris RF structures would be very inefficient for acceleration. However, a great improvement in shunt impedance of the cavity can be made if the beam iris is electromagnetically closed, by using either a thin metal foil or thin-walled tubes. To minimize scattering of the muons by the cavity terminations, one needs low- $Z$  and thin, high-conductivity (both electrically and thermally) materials. In the baseline design pre-stressed thin beryllium windows cover the iris. The requirement on thickness is that the windows must be sufficiently thick to conduct away the heat generated by the RF currents, keeping the temperature below a level determined by the pre-stress so the foils remain in tension and flat.

### 5.3.1 Be windows

The flat Be window is made of a thin high-purity beryllium sheet that is bonded to two thicker annular rings of a slightly lower grade Be material. Figure 5.3 shows a drawing of a 21-cm radius window and the ring thickness required to maintain the pre-stress or thermal gradient. The support ring is 25 mm wide by 25 mm thick. The window is 1.152 mm thick. The exact details of this process are proprietary, but the combination of materials used results in a small but significant difference in the thermal expansion of the foil relative to the ring assembly. This produces a tensile pre-stress on cool down from the joining operation, which helps to keep the foil flat.

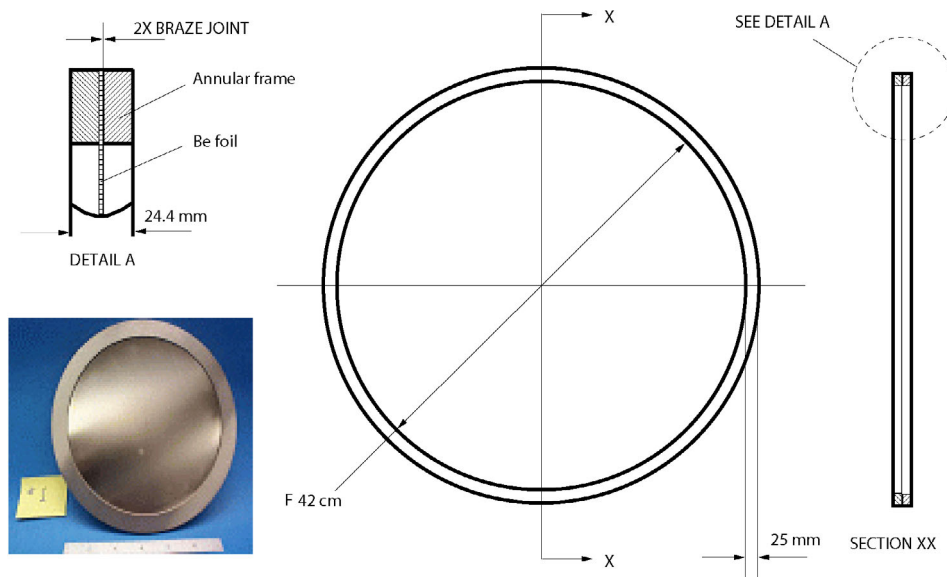


**Figure 5.3:** A pre-stressed 21 cm radius and 1.152 mm thick flat beryllium window design. (The insert photo shows an example of an 8-cm radius Be window made by Brush Wellman Company for 805-MHz RF cavity tests.)

### 5.3.2 Thermal performance

When the foil is heated by RF power, the only significant cooling mechanism for the window is thermal conduction within the foil from centre to edge. In such a case, the temperature distribution assumes an approximately fourth-power profile versus window radius. Detailed FEA and experimental studies have been carried out to understand the behaviour of pre-stressed windows in such a circumstance [Corlett2001].

Figure 5.4 shows the ANSYS-calculated temperature distribution in a 1.152 mm thick, 21-cm radius window. The window remains flat until the thermal expansion exceeds the tensile pre-

stress. At this point compressive stress is generated in the foil, and it starts to deflect by buckling into a gently bowed shape. The maximum allowed temperature difference is about 35°C and is approximately independent of the radius and thickness. Of course, a thicker foil takes more power before reaching the buckling temperature. For larger windows, such as the 21-cm radius needed for the 201-MHz cavity, the foils become quite thick and the scattering of the muons may become significant. One way to reduce the scattering is to use stepped windows, which take advantage of the power density profile ( $\propto r^2$ , with  $r$  the window radius), and make the windows thinner in the middle, where the core of the beam passes, and thicker towards the outside, where there are fewer particles. It is thus possible to reduce the scattering while maintaining the same temperature rise in the foil.

Table 5.2 lists the foil dimensions of the stepped foils used in Study II, and the equivalent flat-foil thickness that would keep the temperature below the critical point. For now the simpler flat foil approach is adopted, but the alternative stepped foil approach is under study.

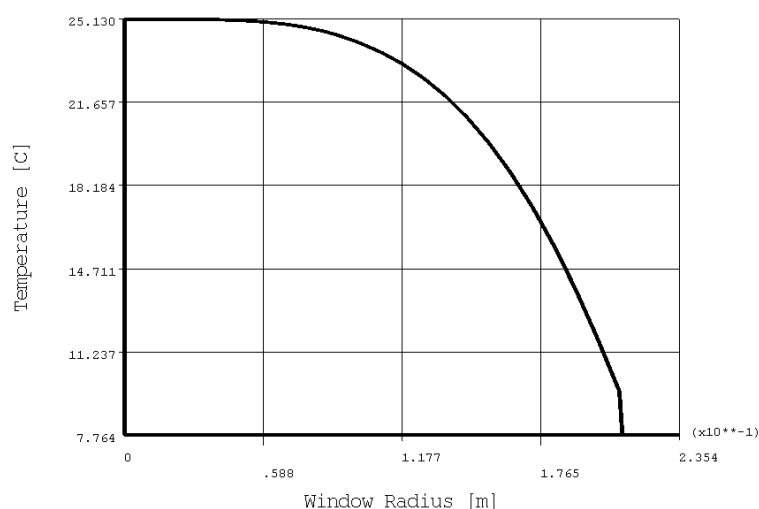


**Figure 5.4:** Temperature distribution of a 21-cm-radius Be window simulated using ANSYS by assuming a 10 kW average power on the 201 MHz MICE cavity.

**Table 5.2:** Stepped Be foil dimensions for 201 MHz RF cavities at the ends (upper) and centres (lower) for Study-II.

End foil radius (inner/outer) [cm]	12/18
End foil thickness (inner/outer) [mm]	0.2/0.4
Equivalent flat foil thickness [mm]	0.325
Middle foil radius (inner/outer) [cm]	14/21
Middle foil thickness (inner/outer) mm]	0.7/1.4
Equivalent flat foil thickness [mm]	1.152

The cavity body needs active cooling to handle the average power losses (about 1 kW average power, i.e., about 1 MW peak power at 0.1% duty cycle) and thus stabilize the frequency. The cooling design is based upon room-temperature operation, although the option of operating at lower temperature (e.g., LN<sub>2</sub> temperature) has been kept open. This option would reduce the

cavity surface resistance and offers higher acceleration gradient for the same peak RF power, at the expense of an additional refrigeration system and tuner complexity.

## 5.4 RF and thermal analysis

Preliminary RF design of the cavity was performed using the URMEL and MAFIA codes running in the frequency domain. The cavity fields and frequency were recalculated using a finite-element analysis (FEA) code, ANSYS. Good agreement was achieved among these codes. Nevertheless, the ANSYS simulations give a more accurate RF power density distribution on the cavity surfaces, as is necessary for a proper thermal analysis. For MICE, the anticipated peak power per cavity (limited by available RF power) is 1 MW at a duty factor of about 0.1% (i.e., 1 ms at a 1 Hz repetition rate). The average power is then only 1 kW, quite modest for a 201 MHz copper cavity and well below the 10 kW assumed for the Study-II cavity. A simple scheme using external cooling tubes gives sufficient cooling for the MICE cavity (see Figure 5.5).

Figure 5.6 shows the temperature profile of the cavity calculated by ANSYS assuming 10 kW average power. The maximum temperature rise is 25°C and the temperature rise across the foil is about 17°C, which is safely below the temperature gradient that results in deformation.

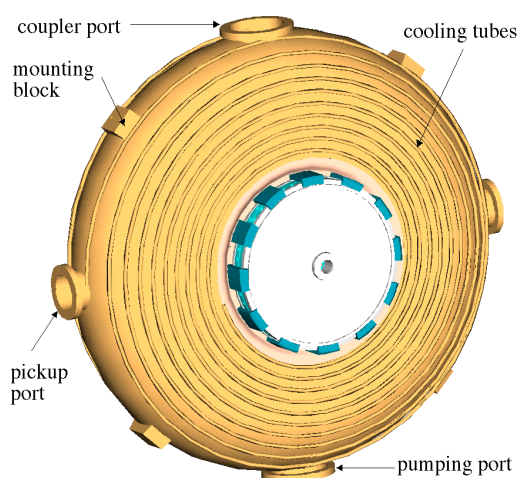


**Figure 5.5:** Cavity model showing external cooling tubes.

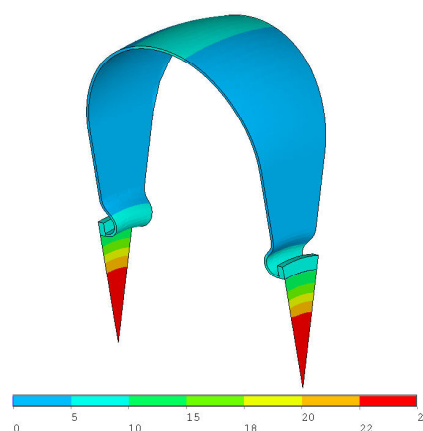


**Figure 5.6:** ANSYS temperature calculation with 10 kW average power.

## 5.5 Vacuum requirements

Two vacuum systems are required. The first system is for the cooling section, which will operate in the  $10^{-7}$  Torr range and provide a guard vacuum for the RF cavities. The second system provides a vacuum in the high-gradient cavities in the  $10^{-9}$  Torr range. To ensure sufficiently high vacuum, each cavity will have its own dedicated vacuum pump and port. Due to the presence of strong solenoidal magnetic fields, cryo-pumps will be used close to the cavities. Ion pumps could be used for initial pump-down and at locations without magnetic field, but these are not currently included in the design.

The RF cavity connections between Be windows present a dead space that requires venting to the cavity body to avoid differential pressure across the window that could cause permanent damage. A possible vent scheme for the windows is shown in Figure 5.7.

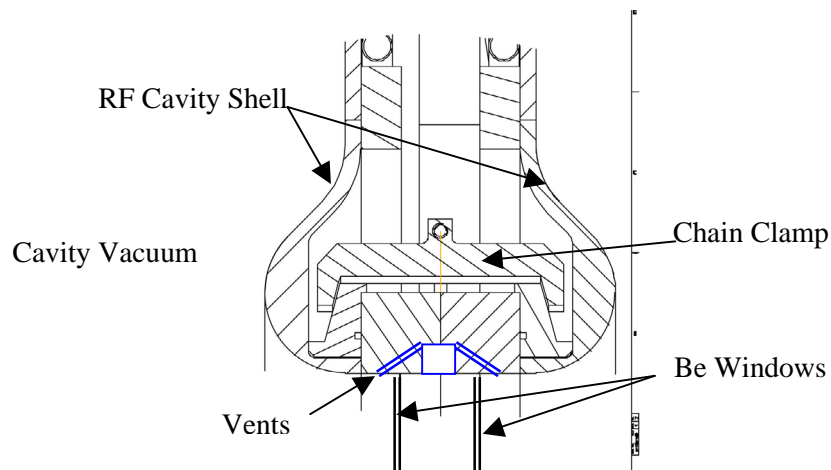


**Figure 5.7:** Vent connection between the cavity and space between the Be windows is realised through vacuum channels drilled on the annular frames of the Be windows.

A thorough bake-out to above 120°C after assembly would be advantageous, but may be incompatible with the nearby superconducting components. If so, the individual components would be baked separately before final assembly into the cryostat.

## 5.6 Cavity cooling

The cavities are subjected to ohmic losses on cavity surfaces due to currents induced by the RF fields. To keep the cavity in resonance with the RF source, active cooling is required. As shown in Figure 5.5, the water-cooling lines are brazed to the cavity body. These lines are 10-mm diameter copper tubing. The cooling water will be provided by the chilled water (LCW) system. This will be a closed-loop system with the LCW system providing circulation. A secondary cooling system will be needed locally in series with the LCW system for more precise temperature control. This secondary system is required to control the cavity temperature to within  $\pm 1^\circ\text{C}$ . ANSYS simulations show that the proposed water-cooling system provides adequate cooling of the cavity body. The temperature rise is only a few °C, even in the cavity locations far from the cooling section. The cooling system is, by design, also compatible with cooling at liquid nitrogen temperature.

## 5.7 RF coupler

RF power is fed into the cavity using a conventional coaxial type loop coupler. A disc-type RF window will be integrated into the coupler. For MICE, the coupler must provide critical coupling and transmit 1 MW peak RF power at 1 kW average power. The MICE coupler design is based on the coaxial loop coupler designed for the Spallation Neutron Source (SNS) project, although modifications are needed to make it work at 201 MHz. At the peak and average RF power available for MICE, no serious technical difficulty should arise. However,

operating the couplers in strong magnetic fields raises concerns about multipacting, gas discharge, etc. Coating the couplers with a thin TiN layer should prevent multipacting. The coupler will be tested and conditioned separately. A coupler from SNS will be available for tests at Lab G of Fermilab.

## 5.8 Cavity tuning requirements

As beam loading is negligible, the tuning requirement for the cavities is simply to compensate for temperature variations due to water supply changes, RF heating, and Lorentz detuning forces. Each cavity is powered individually and its phase can be adjusted independently for optimum performance of the cooling section. Due to the high quality factor of the cavity ( $Q \approx 55,000$ ), the unloaded cavity bandwidth is only 3.7 kHz and the loaded bandwidth is 7.4 kHz at critical coupling.

Tuning will be accomplished using a combination of a fast and a slow tuner, each cavity requiring one of each type. The fast tuner could be a conventional, off-the-shelf moving plunger tuner; a dedicated port in the cavity would be needed for this. A piezo-electric fast tuner is an alternative approach. However, further investigation is needed to justify its application for MICE operating conditions. The slow tuner uses a tuning scheme similar to that used for superconducting cavities, e.g., those at CEBAF at Jefferson Laboratory (JLab), in which the cavity is mechanically stretched or compressed within elastic limits. Simple two-dimensional calculations show that if the length of the MICE cavity is varied from its nominal value of 43 cm, the frequency sensitivity is about 236 kHz/mm, so a small range of motion suffices to achieve the required tuning range. For MICE cavities, the slow tuner is required to deform the cavity over a range of  $\pm 250 \mu\text{m}$  ( $\pm 59 \text{ kHz}$ ) with better than  $1 \mu\text{m}$  precision. (Given the cavity's  $Q$  value, 236 Hz of detuning corresponds to approximately  $3^\circ$  of RF phase shift, or 1 part in  $10^3$  in accelerating gradient, which is the level of stability required for a  $10^{-3}$  emittance measurement.) Experience from CEBAF operations and examination of the literature indicate that mechanical schemes using micro-drive stepping motors can easily achieve this range of motion with the required accuracy. This tuner will accommodate the small changes in the cooling water temperature. Bulk water temperature fluctuations of the order of  $1^\circ\text{C}$  or less have been assumed. The thermal expansion coefficient of copper is  $17 \times 10^{-6} \text{ K}^{-1}$  at room temperature, so the frequency variation would be about 3.4 kHz for a  $1^\circ\text{C}$  temperature change of the cavity. In principle, it would be possible to tune each cavity temperature slowly over a limited range simply by controlling the water temperature, but the water stability would have to be a fraction of a degree, and a separate water temperature control system would be required for each cavity. This is viewed as workable, but unattractive.

## 5.9 Cavity integration

Integration of the cavities into the cooling section requires four separate connections: cavity-to-cavity, cavity-to-raft, raft-to-cooling system, and cavity-to-port. Each of these connections must accommodate the motion of the cavities as a result of tuning or temperature changes.

A 4-cavity assembly is shown in Figure 5.8. As shown previously in Figure 5.1, the MICE cooling section is made up of two such units. The 4-cavity assembly is hard mounted together and chain clamped between the windows, except between the middle cavities where a bellows

is used. This bellows is necessary to allow the cavities to expand or contract in the channel. The end cavities are hard mounted to the channel at the windows. In addition to the iris connections, the cavities are also mounted to the cooling section using flexures attached to the raft that allow for cavity motion due to temperature changes and tuning. It is anticipated that the flexure mounts will need to accommodate up to 1 mm of cavity travel for room temperature operation and tuning. The vacuum and RF ports will also need to be designed to allow for cavity motion. For LN<sub>2</sub> (77 K) operation, the flexure-mounts will need to be adjusted to accommodate up to 4 mm of travel. Fortunately, the RF source frequency can be tuned to the resonant frequency of the cavity at LN<sub>2</sub> temperature, so the tuning range of the flexures is unchanged.

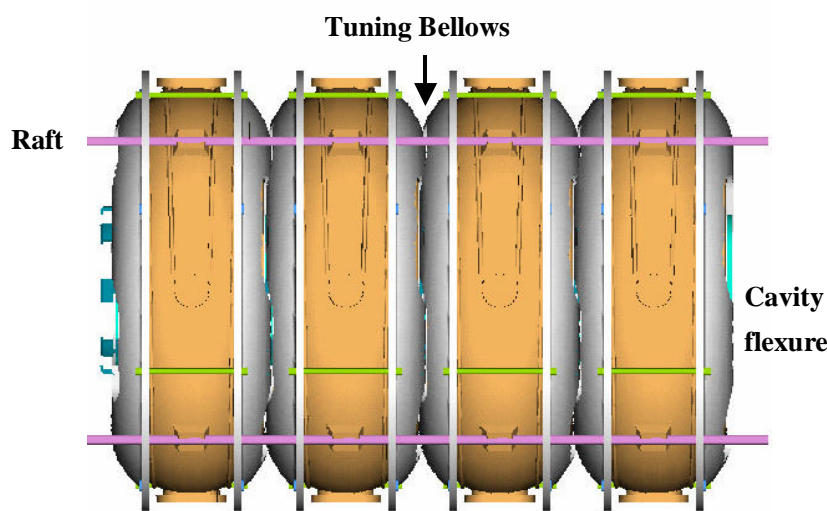


Figure 5.8: Four-cavity assembly on the raft.

## 5.10 Cavity performance

Table 5.3 summarizes the MICE cavity requirements compared with the Study-II parameters. Because the MICE cavity gradient is limited by the available RF power of 8 MW, a total of about 21 MV acceleration (on crest) will be provided by the eight MICE cavities. Peak surface field is only 12 MV/m, compared with the Kilpatrick value at 201 MHz of 15 MV/m. In case of operation at liquid-nitrogen temperature, the resistivity of copper being decreased by a factor 8, the gradient that can be reached for the same RF power should increase by a factor 1.5 to 1.7. This possibility would allow high gradient investigations for limited periods.

In terms of RF gradient, peak surface field and power dissipation on the Be widows, the overall technical risk of the MICE RF system is low. Nevertheless, the cavities have to operate in a strong magnetic field, so cavity and coupler conditioning, dark currents, and x-ray production need further investigation. Lab G at Fermilab, along with the new MUCOOL Test Area now under construction, provide excellent facilities for these studies. RF tests on an 805-MHz cavity with Be windows are under way at Lab G. They will provide valuable information on the above issues that will help optimize the designs for both the cavity and the MICE detectors.

**Table 5.3:** MICE cavity requirements compared with the Study-II parameters.

Parameter	MICE	Study-II	Unit
$V_{\text{eff}}$ (on crest)	2.67	5.76	MV
$E_0$ equivalent	7.5	16.2	MV/m
$E_{\text{peak}}$ on surface	12.3	26.5	MV/m
Peak power per cavity <sup>a</sup>	0.9	4.18	MW
Peak forward power ( $3\tau$ filling)	1.0	4.63	MW
Average power	1.0	8.36	kW

<sup>a</sup>Actual cavity  $Q_0$  assumed 85% of theoretical value.

## 5.11 RF transmitters

Two 4-MW transmitters are foreseen for MICE to power a total of eight cavities, each with 1 MW. Some components of RF power amplifiers are available both at CERN and at RAL. At CERN most of the components to rebuild an amplifier of the dismantled Linac 1 type exist. Those amplifiers were originally used with a Thomson TH 470 tube cooled by boiling off water. These tubes are capable of an output power of the order of 2 MW. The amplifier can be equipped with a Thomson TH 516 tube or with the water-cooled version Thomson TH 116. The latter is preferred for stability reasons. With some additional modifications to allow the use of plate voltages up to 40 kV, power levels of 4 MW can be reached. In particular, to improve voltage holding, the construction of a Kapton or Teflon-insulated plate-blocking capacitor is necessary. At RAL there is also one spare coaxial structure for a TH116 tube which would require some refurbishment before it could be used.<sup>3</sup>

Driver amplifiers of roughly 400 kW are needed on the input side of the TH 116 final amplifiers. At CERN, there are three Siemens amplifiers available, capable of going up to approximately 400 kW. One could be used as driver for one TH 116 amplifier. If the output power were insufficient, the power of three amplifiers could be first combined and then split with a hybrid to drive the two final amplifiers. As an alternative, the power of two Siemens amplifiers could be combined with a hybrid to drive one of the TH 116 amplifiers, whereas the other would require another driver, possibly with a combination of several old tetrode amplifiers (using RS 2058 tubes) from the CERN SPS. For the low-power stages, spare amplifiers from RAL can be used.

Although CERN used delay-line type modulators for both Linac 1 and Linac 2, it is felt that cathode switching is a more convenient and cheaper method. CERN has made successful tests of this approach and, at RAL, such a system is operational in a satisfactory manner. Cathode switching would be applied to the TH 116 final amplifiers and to the Siemens amplifiers.

## 5.12 RF distribution system

RF power from two 4-MW transmitters would be sent to the RF cavities via standard 9-inch rigid coaxial transmission lines (smaller diameters are also possible). The lines are large enough to handle the required RF power but may give small reflections. Directional couplers for forward and reflected RF power will be installed. Phase shifters after the final hybrids are

<sup>3</sup>David J S Findlay, Rutherford Appleton Laboratory, private communication (2002).

required to correctly adjust the RF phases for the cavities. In addition, the line length must be adjusted for proper coupling to the cavities and to avoid high voltages at the amplifiers in case of breakdown in a cavity. The latter is not very critical as the hybrids provide some isolation; that is, part of the reflected power will be absorbed in the dummy loads of the hybrids.

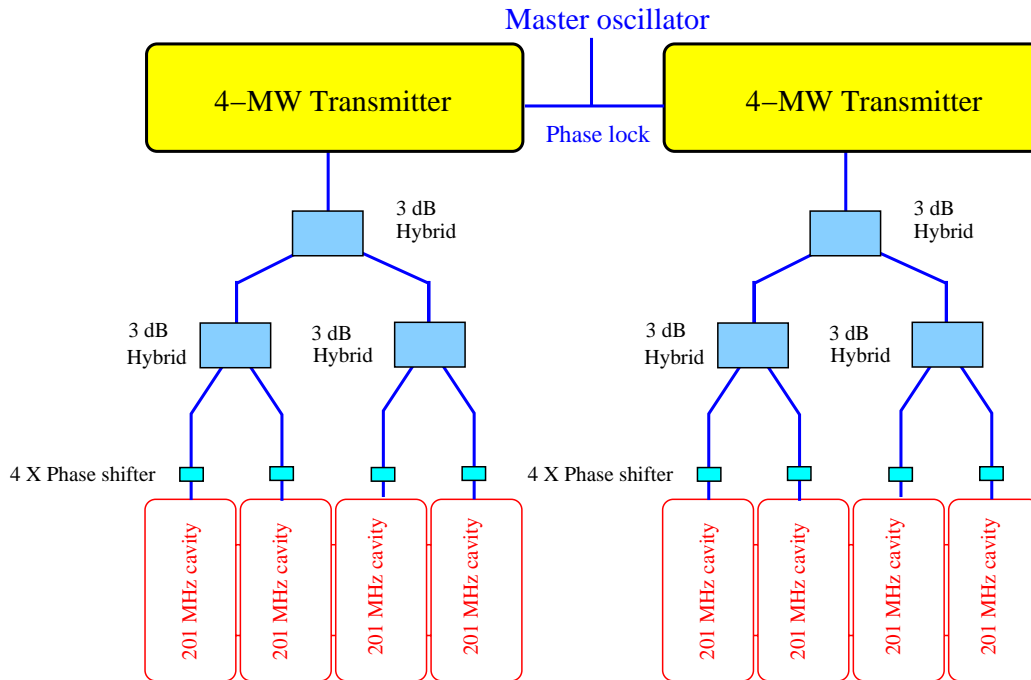


**Figure 5.9:** Diagram of RF distribution system for MICE.

### 5.13 RF control system

Feedback is necessary to control amplitude and phase to a precision of the order of 1% and  $1^\circ$ . Measuring loops in the cavities must produce the required signals. The cavity tuners will each have a separate loop, where the phase in the cavity is compared with the phase of the forward power in the feeder line. The derived error signal will be used to adjust the fast and slow tuners. The general layout can be similar to the scheme used at CERN (Figure 5.10). Note that each of the eight cavities needs its individual tuner loop to achieve phase and amplitude stability. Also, each cavity has its individual (slow) phase adjustment using variable line length on the coaxial feeder lines. The general amplitude and phase feedback works only on the two 4 MW amplifier chains.

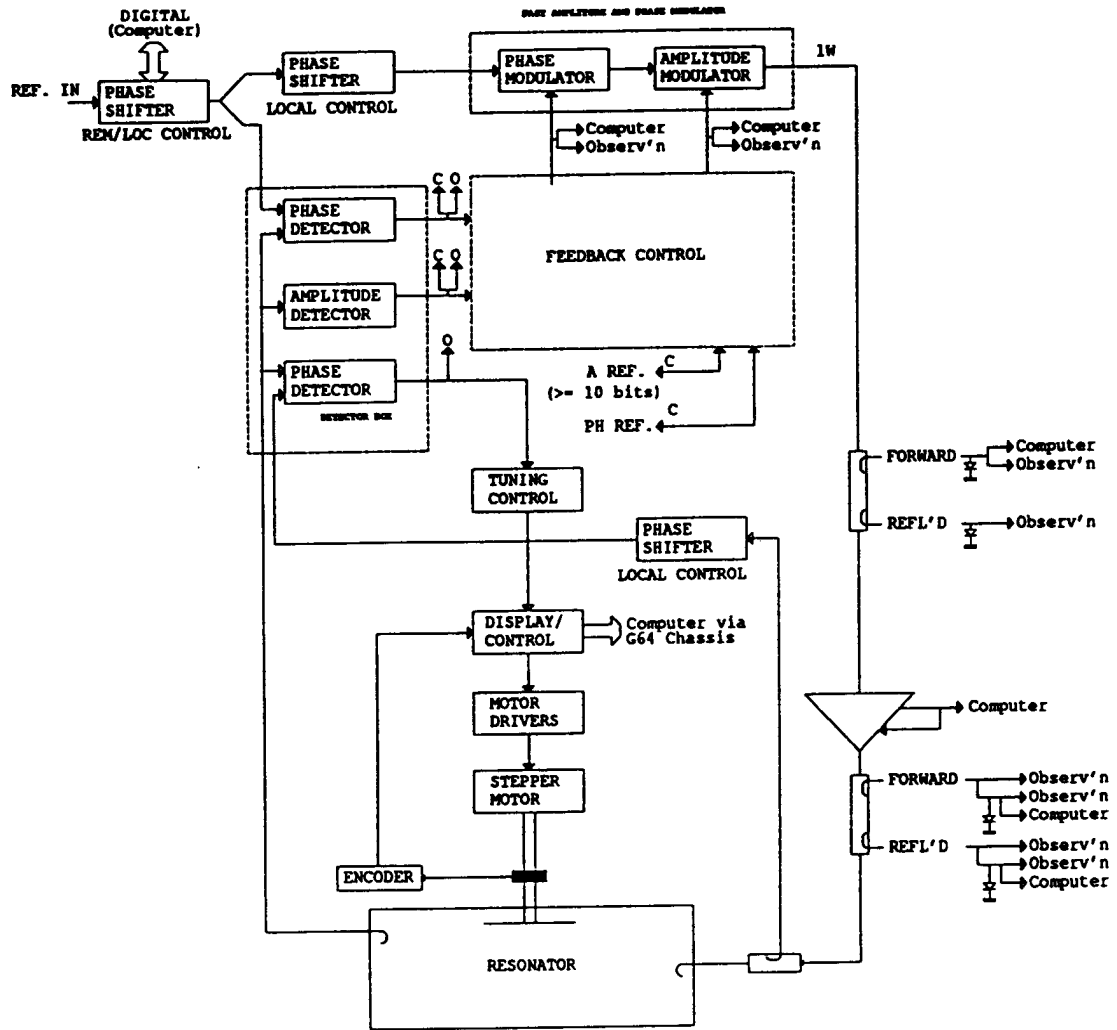


Figure 5.10: Schematic layout of a RF control system as used on the CERN linacs

## 6 LH<sub>2</sub> Absorbers

### 6.1 General design

The reduction in normalized emittance of the MICE muon beam will occur in liquid-hydrogen (LH<sub>2</sub>) absorbers. Muons lose energy in the absorber material by ionization. This reduces their momentum in all directions, thereby increasing their density in phase space. Hydrogen was chosen as the most suitable absorber material because of its large ionization energy-loss rate ('cooling') and small probability of multiple scattering ('heating'). Heating is further minimized by placing the absorber in a high-gradient focusing magnetic field.

The considerations driving the design of liquid-hydrogen absorbers are: (1) minimizing multiple scattering, (2) achieving a sufficient heat transfer rate to maintain uniform absorber density and temperature and (3) safe operation. Safety guidelines are based on the redundant requirements of oxygen and hydrogen separation and avoidance of any possible ignition sources in the vicinity of the hydrogen, reflecting the underlying principle that the system must be failsafe even in the case of two simultaneous failures. Additional design challenges stem from the location of the absorbers: a confined space within a superconducting magnet and between RF cavities, both of which are potential ignition sources.

The absorber is designed to handle a total heat input up to about 100 W. The primary absorber heat source in MICE ( $\approx 15$  W) is expected to be thermal radiation from the room-temperature RF window. Other heat sources (heating by the muon beam, RF cavity dark currents, and conduction through the LH<sub>2</sub> manifold and support structure) contribute relatively less. The absorber is designed to use natural convection and an internal helium-gas-cooled heat exchanger to maintain a uniform temperature and remove heat from the absorber volume.

The absorber and focusing coil module is shown in Figure 6.1. The absorber length is 35 cm and the diameter is 30 cm. The hydrogen volume is 21 l. To help in satisfying the safety requirements, the absorber assembly includes two sets of windows. The space between the inner ('absorber') and outer ('vacuum') windows is vacuum pumped. Details of the safety system are given in Section 10. The four key features of the design with respect to safety are:

1. The window thicknesses are specified based on safety factors against bursting of 4.0 for the absorber window and 2.5 for the vacuum window (at maximum allowable working pressure).
2. An argon-gas-filled jacket surrounds the vacuum chambers of the RF/coupling magnet modules and the hydrogen absorber/focusing magnet modules to eliminate the possibility of oxygen leaking in and freezing on the absorber-system windows.
3. Separate vacuum volumes are provided for the RF cavities, magnets, and LH<sub>2</sub> absorbers.
4. Hydrogen evacuation systems are provided using valved vents into external buffer tanks.

The temperature of the vacuum window will be maintained at  $\approx 50$  K by heat conduction through the absorber support structure. Any significant absorber leak will rapidly cool the window to below the boiling point of hydrogen, preventing rapid expansion of large quantities of hydrogen liquid into gas. Separate vacuum volumes for the magnet, LH<sub>2</sub>

absorber and RF systems will maintain optimal temperatures for their respective operations, and avoid possible hazards in the event of a failure in any of them. In particular, the focusing-coil vacuum and absorber vacuum are separated to avoid magnet quenching in the case of a hydrogen system refrigeration failure. The beam line and RF vacuum volumes not only need to be maintained at ultrahigh-vacuum levels, but the RF cavities represent a potential ignition source and must be isolated from the LH<sub>2</sub> vacuum and evacuation volumes.

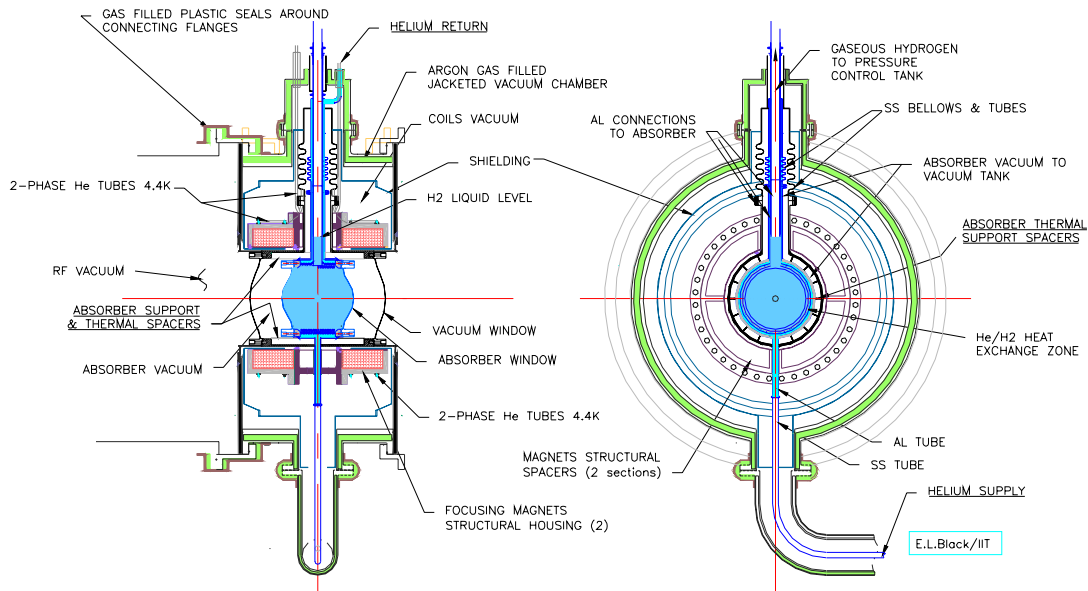


**Figure 6.1:** Engineering rendering of the absorber and focusing-coil module.

Another concern is the possibility of oxygen condensing anywhere inside the hydrogen vacuum or evacuation volumes. If there is any leak from the absorber assembly to the cooling cell exterior, oxygen is likely to enter the assembly and freeze. The frozen oxygen would not be detected by oxygen sensors, and would become a hazard should the vacuum fail and the oxygen vapourize. By providing a layer of argon gas surrounding all of the component vacuum systems at slightly higher than atmospheric pressure, this hazard is eliminated.

## 6.2 Windows

The development of thin aluminium windows to minimize multiple scattering is an ongoing activity of the MUCOOL Collaboration. A series of novel window designs (Figure 6.3a) have been devised that depart from the standard spherical and torispherical shells [ASME80]. The first MUCOOL design, a torispherical shell modified with increased thickness near the ‘knuckle’ for additional strength, achieved a minimum thickness about half that of a standard torispherical shell. A second design incorporates a spherical cap joined to the mounting flange via an inflected, tapered toroidal section, gaining another factor  $\approx 2$  in thickness. The most recent design achieves the same strength with the same central thickness and less material at the edges.

The window designs were developed and refined with extensive guidance from finite-element-analysis (FEA) studies. Figure 6.2 shows results from the FEA study of a window of the ‘thinner-inflected’ design that is 34 cm in diameter and has a central thickness of 130  $\mu\text{m}$ . Figure 6.2a shows the displacement of the window as a function of radius under internal

pressurization at the calculated burst pressure, 5.6 atm. Figure 6.2b shows the von Mises' stress in the aluminium alloy vs radius for the same condition. The stress is nearly uniform throughout the window material, indicating that the taper of the thickness profile is close to optimal. Figure 6.2c shows results of an FEA analysis for the same window under external pressurization. No buckling is seen up to 2.3 atm of external pressure; beyond that pressure the material begins to yield inelastically.

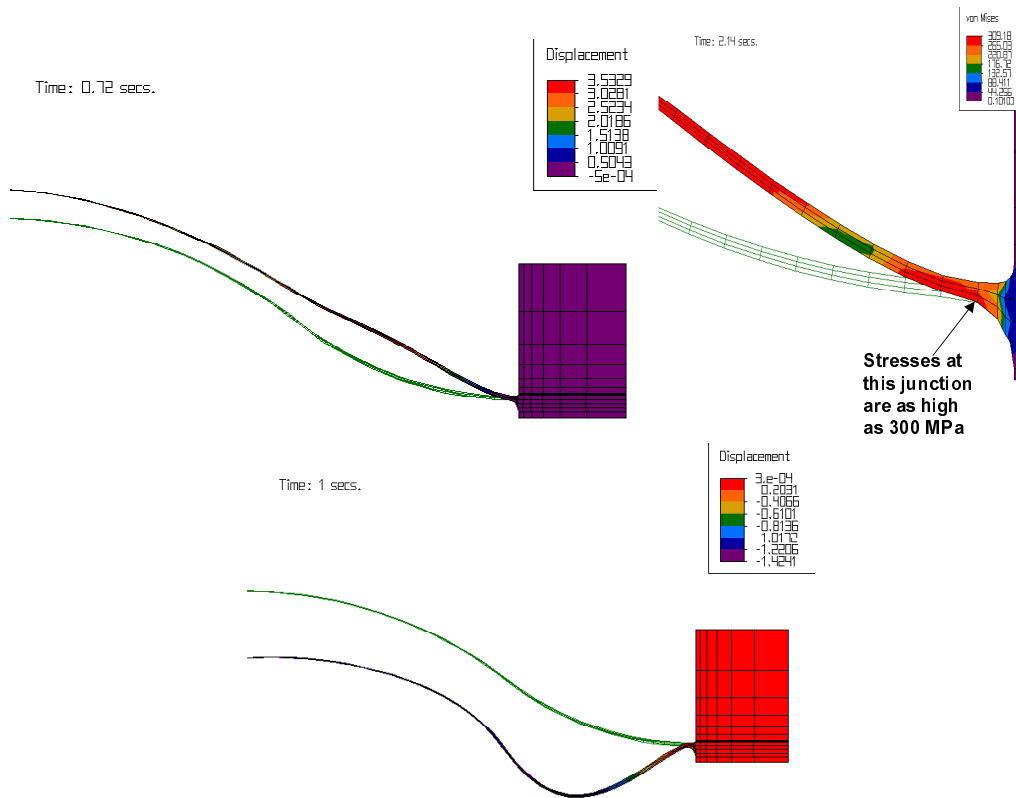


**Figure 6.2:** Top: predicted a) displacement (left) and b) stress (right) vs radius of the 34 cm window at burst pressure; for visibility, deflections have been greatly exaggerated; bottom: c) predicted displacement vs radius of the 34 cm window unloaded (green) and under external pressurization to 2.3 atm (various colours).

FEA studies of such windows for a variety of thicknesses and diameters show that the internal burst pressure and external yield pressures are very nearly linear in thickness and inversely proportional to diameter. Therefore linear scaling has been applied to obtain the thicknesses given in Table 6.1. Comparing the FEA results to the minimum pressure requirements for internal and external loading of vacuum windows in Table 6.1, one sees that the internal loading requirement is the more stringent and determines the required thickness. Further FEA modelling of the actual windows to be built for MICE will be carried out before the final construction for MICE, as well as an extensive series of destructive and nondestructive pressurization tests of prototype windows.

Window of these shapes are individually manufactured out of a single disc of aluminium alloy using a numerically controlled lathe. These designs justify the 500  $\mu\text{m}$  window thickness used in the simulation presented in Section 3. The proposed window specifications are given in Table 6.1.

**Table 6.1:** Absorber-assembly window specifications.

	Absorber window	Vacuum window
Material	6061-T6 Al alloy*	6061-T6 Al alloy*
Diameter (cm)	30	40
Central thickness ( $\mu\text{m}$ )	180	180
Min. burst pressure–internal loading (atm)	6.8	5.0
Min. yield pressure–external loading (atm)	—	1.7

\*Use of the stronger 2195 alloy is under investigation; this could allow the window thickness to be reduced by 45%.

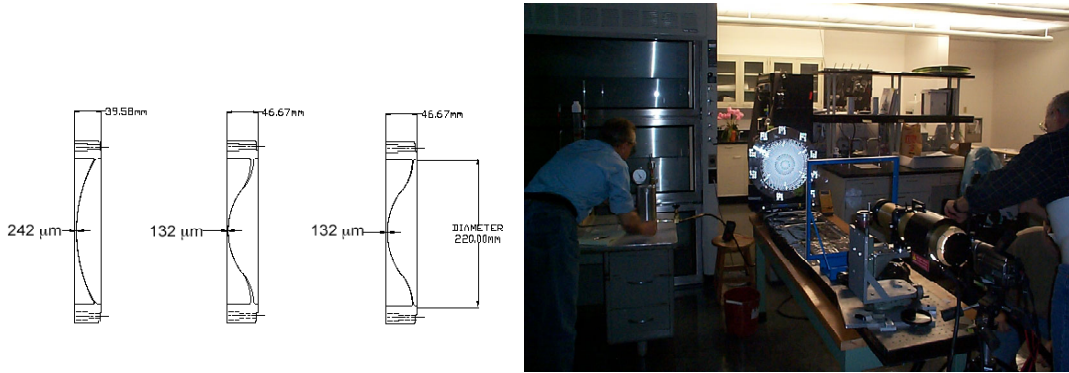


**Figure 6.3:** a) Profiles of three non-standard window designs: ‘tapered-torispherical’, ‘inflected’, and ‘thinner-inflected’ (left); b) photogrammetry set-up at NIU with projector in foreground, camera on right, projected dots on window, and stationary targets on flange (right).

Prototypes of these designs are tested and qualified via a novel application of photogrammetry [Mikhail01], using optical projection of dots measured via a position-calculating digital camera (see Figure 6.3b). Precision of  $\approx 10 \mu\text{m}$  in window thickness and profile has been demonstrated [Cummings02]. The third (‘thinner-inflected’) design in Figure 6.3a is the one planned for MICE, both for absorber and vacuum windows. Manufacture and testing of a prototype of this new design are underway.

### 6.3 Thermal design

The cooling power  $\dot{Q}$  can be calculated from the helium-coolant temperature difference  $dT$  as follows, if the pressure drop and latent heat of the helium are neglected:

$$\dot{Q} = \dot{m}_{\text{He}} dH dT, \quad (6.1)$$

where  $\dot{m}_{\text{He}}$  is the helium volume flow rate and  $dH$  is the helium enthalpy difference. For an inlet temperature  $T_{\text{in}} = 14 \text{ K}$ , outlet temperature  $T_{\text{out}} = 18 \text{ K}$ , and muon heating  $\dot{Q} = 100 \text{ W}$ ,  $\dot{m}_{\text{He}}$  is 5g/s. As described in Section 3, this flow rate and cooling power are achievable using a standard refrigerator.

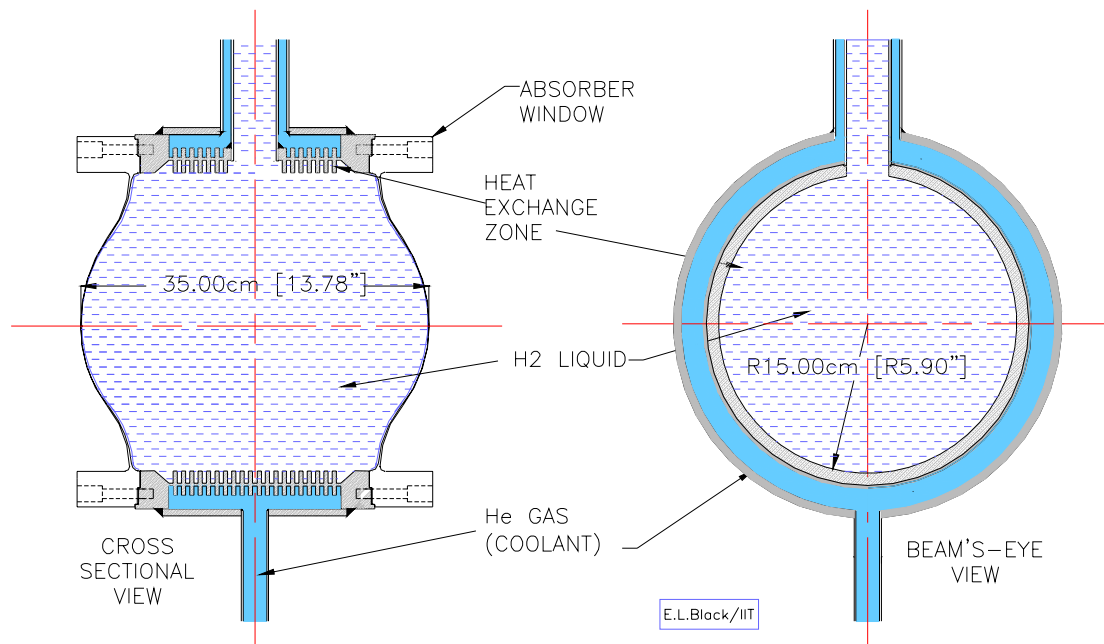


**Figure 6.4:** Liquid hydrogen absorber.

The absorber with its built-in heat exchanger is shown in Figure 6.2. The absorber body and heat exchanger are made of aluminium. The windows are indium-sealed at both ends of the absorber. The heat exchanger is carefully designed to minimize the temperature difference at the metal–liquid boundary.

A computational simulation of natural convection with beam heating has been performed, and indicates that uniform temperature can be maintained within acceptable limits of fluctuation. The  $\text{LH}_2$  density changes from 0.077 at 14K to 0.070 at 21K, almost linearly. Thus, the maximum  $\text{LH}_2$  density fluctuation is 0.007, or  $\pm 5\%$ , and the average effect seen by a muon will be less than this. Study-II cooling simulations showed negligible (percent-level) effects on cooling performance for average-density fluctuations as large as 5% [Study II].

## 6.4 Responsibilities, costs and timelines

Northern Illinois University (NIU) and KEK will be responsible for the integration and installation of the  $\text{LH}_2$  absorbers into the MICE cooling section, and for the absorber-specific instrumentation and readouts. The  $\text{LH}_2$  absorber and vacuum window R&D programme is being conducted primarily by IIT, the University of Mississippi, NIU, and the University of Oxford, in collaboration with FNAL and the University of Illinois at Urbana-Champaign. A series of flow tests, for both the MICE (convection-cooled) and MUCOOL ('forced-flow-cooled') prototypes, is planned through 2003. (The forced-flow design is aimed at higher power dissipation and will be power-tested in a high-intensity proton beam as part of the MUCOOL programme.) A programme at Argonne National Laboratory is being developed to study convection patterns in liquids heated by beam energy deposition (in this case 15 MeV electrons) using laser apparatus based on Schlieren techniques. This will provide data to help determine currently poorly understood heat transfer coefficients and verify fluid dynamics

computations specific to convection flow simulations. These studies will then be extended to model the prototypes developed by KEK and Osaka University and to fine-tune the final MICE absorber design. These tests will also help determine proper instrumentation for cryogenic operation in the MICE experiment.

## 7 Beam and Beam Line

The requirements on the beam line have been delineated in Section 3. Taking into account the energy loss in the emittance generating section, the muon momentum must reach  $300 \text{ MeV}/c$  (and preferably up to  $400 \text{ MeV}/c$ ), muon purity must be better than 90%, and the beam line must deliver a rate of at least a few muons per microsecond for a duration of several hundred microseconds. Such a beam can be provided at RAL by upgrading an existing beam line.

### 7.1 Layout and location

The muon beam line for MICE will use particles produced in the ISIS synchrotron at RAL and will replace the existing high-energy beam line already installed in experimental hall R5.2. The existing beam line has poor performance in terms of muon number and purity. The new beam line will address both issues and will deliver a high purity, high rate muon beam. Particles from the target (mainly pions, but also protons and a few muons) are captured by a quadrupole-doublet and momentum analysed in a rectangular dipole magnet. The momentum analysed beam then enters a 5-m-long superconducting solenoid where pions, muons from pion decay and residual protons are transported to a second dipole magnet. This second dipole selects the muon momentum and is set to a lower value than the first one, to remove particles from the original beam and produce a *clean* muon beam. The proposed beam line is shown in its location in the synchrotron vault and hall 5.2 in Figure 7.1.

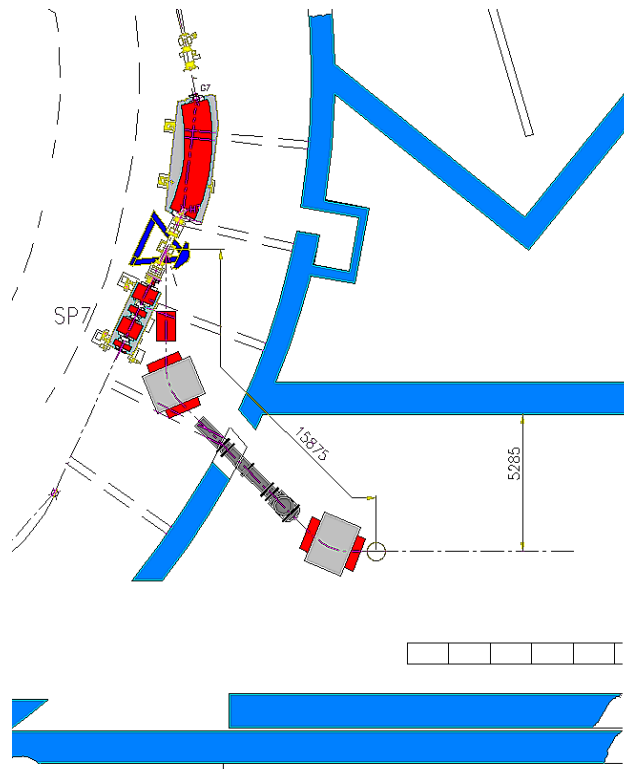


**Figure 7.1:** Layout of the muon beam line on ISIS.

The beam line is straightforward from a vacuum point of view. An all-metal seal system will be built and will be pumped by a single turbo-rotary pump system to reach pressures of  $10^{-6}$  torr. The vacuum will be separated from the ISIS machine vacuum by an air gap, rather than only by the window of the present beam line.

Control of the beam line and its vacuum system will be provided by a standard PLC system which provides user-safe programmed operation. Access to the system will also be possible from a networked PC. New power supplies will be obtained for the beam line elements which will also be controlled through the PLC. Settings can be loaded and stored in a database. The control of the internal synchrotron target system can also be made available to the users (within limits defined in the PLC system). ISIS is protected from accidents by beam loss monitors around the synchrotron ring, which will trip ISIS if the beam loss becomes too high.

A small titanium target in the synchrotron provides the source of pions. The current target system is old and unreliable and will be replaced with a simpler device for MICE. Modern technology provides a means of producing a fast moving device that can be pulsed at a few Hz, inserting the target into the proton beam for roughly a ms duration. The target will be designed to re-use as much of the existing infrastructure as possible (depending on its activation state) and so be a relatively simple upgrade. A schematic of the target is shown in Figure 7.2.

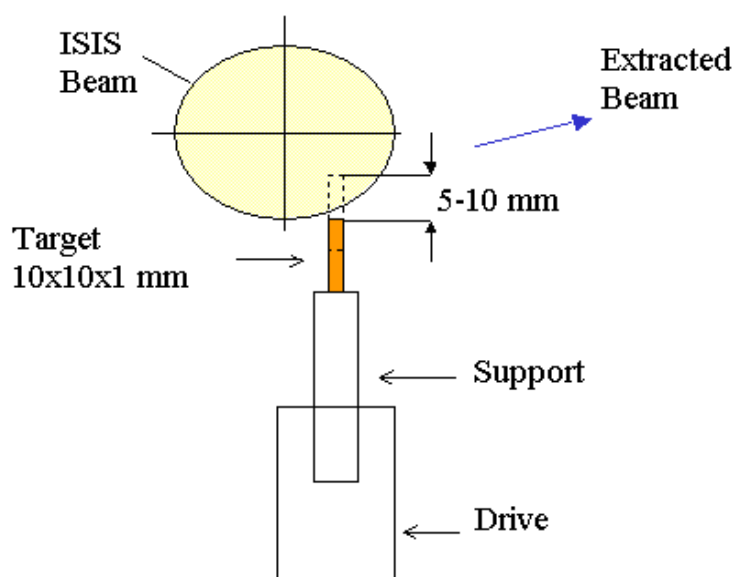
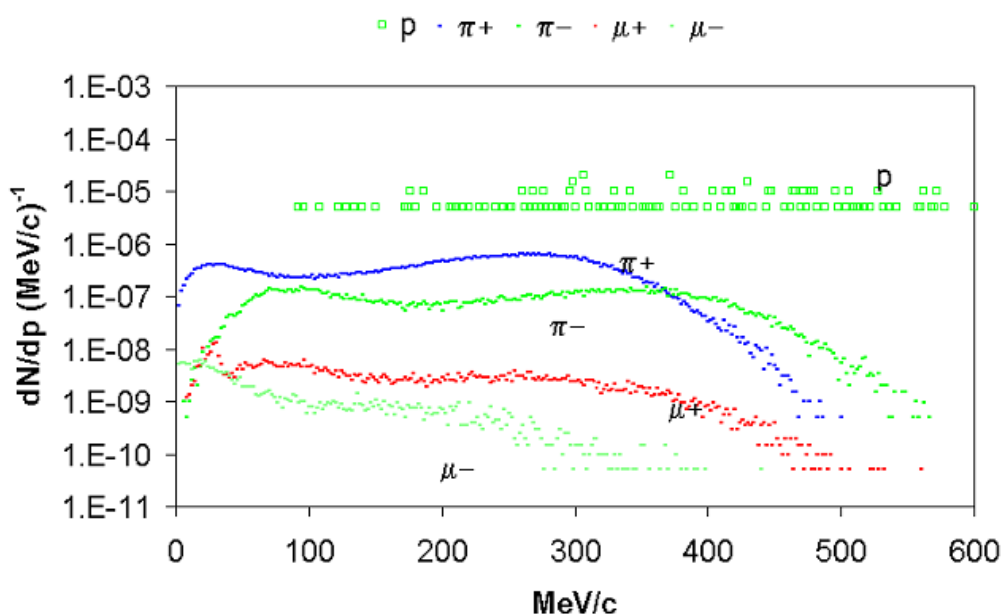


Figure 7.2: Target Schematic

## 7.2 Expected performance and time structure

LAHET [Prael89] has been used to estimate the distribution of particles produced in the small volume target envisaged for the muon beam line. Pions are produced with a momentum of up to about  $500 \text{ MeV}/c$  at an angle of  $25^\circ$  (see Figure 7.3). The maximum pion momentum available depends strongly on the scattering angle as does the intensity at high momentum. The proposed new beam line will capture pions at an angle of  $25^\circ$  to the proton beam, which is the smallest practical scattering angle achievable given the installation constraints next to the synchrotron. The baseline design for the beam line can be divided into three parts: Pion

capture and momentum selection; a pion-to-muon decay section; and a subsequent momentum selection to separate the muons from the pions (and protons). The muons from pion decay essentially fill a cone – the result of transforming a  $\sin \theta_{\text{cm}}$  distribution in the pion rest frame to the lab frame. Muons emitted at large angles (in the pion rest frame) have the largest momentum difference from the original pion and can be more easily separated from the remaining pion beam and the protons. This separation is momentum dependent, and favours higher pion momenta. To optimize the muon transport, it is best to use a solenoid to transport the pions in the decay part of the beam line [PSI, RIKEN]. However, a set of quadrupoles could also be used with lower efficiency [TRIUMF]. The efficiencies of these two schemes are compared below.



**Figure 7.3:** Spectra of particles scattered into the pion/muon beam line (per beam proton per MeV/c).

Figure 7.4 shows the paths of pion and protons through the two possible beam lines (decays were turned off for these plots). In both cases, the first dipole is set to select 400 MeV/c particles, while the second dipole selects 300 MeV/c particles. Clearly, the original beams are effectively lost in this element. Ray tracing protons with a full momentum range (up to that of the synchrotron proton beam) demonstrates that the beam line shown in Figure 7.4 can reduce original beam particles to at least a level of  $10^{-4}$ . The beam optics presented here will suppress the original beam to a level of better than 10% of the muon flux. Typical muon beam rates are given in Table 7.1, measured at a point 3 m downstream of the final dipole magnet.

The ISIS synchrotron is cycled with a repetition rate of 50 Hz. The proton beam rotates around the synchrotron with a varying frequency, which, towards the end of acceleration, is  $\approx 1.5$  MHz. As shown in Figure 7.5, the micro structure of the beam consists of two bunches  $\sim 100$  ns long with a gap of  $\approx 230$  ns that rotate at exactly opposite positions in the machine. The total number of protons in the beam is  $\approx 2.5 \times 10^{13}$ .

The number of pions/protons arriving at the entrance of the solenoid could be measured using a scintillation counter, which should also be able to separate protons from pions using the  $dE/dx$  signal. Measurements to benchmark the calculations could be useful at an early stage.

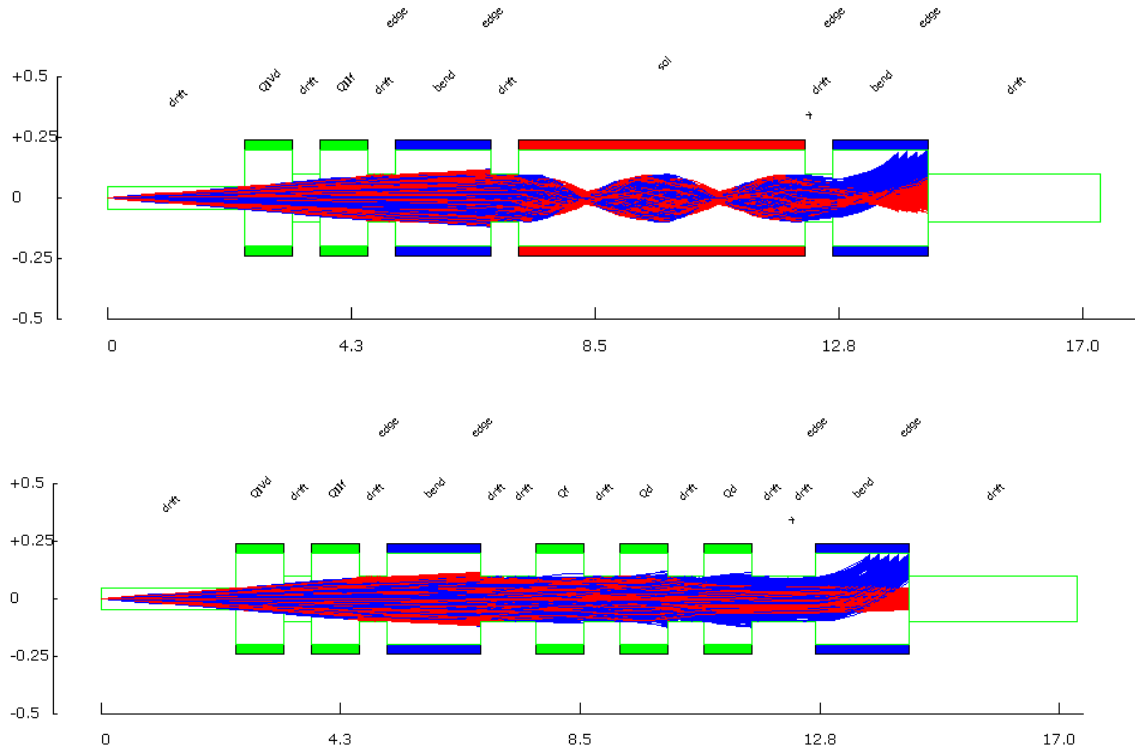


**Figure 7.4:** Particles traced through (top) solenoid and (bottom) quadrupole decay channels. Quadrupoles are drawn as the small rectangles, the dipoles as the intermediate rectangles and the decay solenoid as the long rectangle. The horizontal (vertical) projection of the beam is shown by the dark (light) lines.

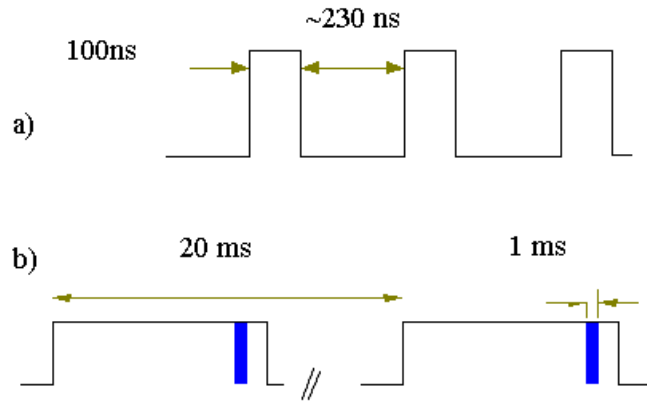


**Figure 7.5:** a) the micro-structure of the ISIS synchrotron beam prior to extraction: there are two bunches rotating at opposite positions in the machine and b) the macro structure of the beam with the time the target is in the beam shown in blue.

**Table 7.1:** Estimated muon yields as a function of muon and pion momentum for the solenoid and quadrupole channels. The yields are for a single 1 ms burst of beam on the target.

Pion Momentum [MeV/c]	Muon momentum [MeV/c]	$N_{\mu^+}$ Solenoid beam	$N_{\mu^+}$ Quadrupole beam
300	200	3000	300
400	300	200	20

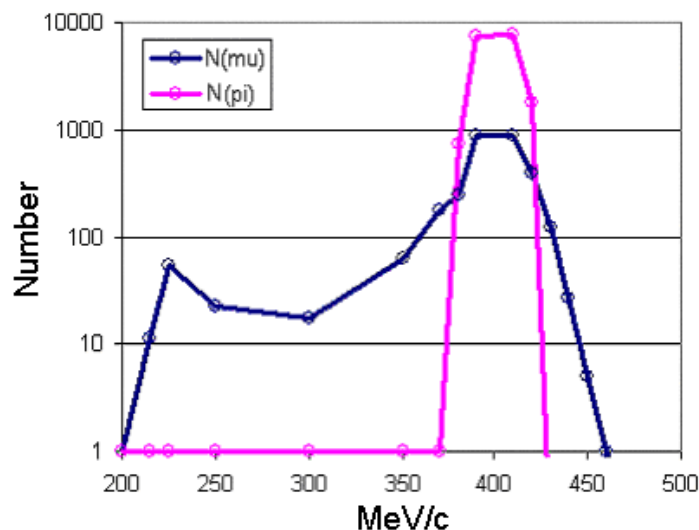


**Figure 7.6:** Relative yields of pions and muons from a 400 MeV/c pion beam vs momentum.

### 7.3 Time line

The baseline plan is to use a decay solenoid that will be made available by PSI, assuming that its activation is within the allowed RAL radiation limits. Stands for the components will have to be designed and procured, and the solenoid shipped to RAL. All other beam line components will be re-cycled from the existing beam line.

ISIS operates fairly continuously for long periods (over several months) interspersed with short shutdowns of the order of 1 or 2 weeks. Machine maintenance occurs at longer intervals and can last several tens of weeks (long shutdown). The latter present the only opportunity to do work in the synchrotron vault since a period of approximately two weeks is required to allow the machine to ‘cool down’. Preparation for the muon beam line requires an aperture to be put in the wall between the MICE hall and the synchrotron, once the existing hall has been cleared out. This can only be done during a long shutdown. Additionally, the aperture must afterwards be made safe from a radiation protection point of view. This implies a minimum amount of work that needs to be completed during the long shutdown. The current understanding of the ISIS machine schedule is that there will be a long shutdown towards the end of 2003. As it is unlikely that a cryogenic system would be available at this time, a conventional quadrupole channel will be installed initially. Considerable civil engineering and shielding work needs to be completed during this shutdown. The solenoid could replace the quadrupole channel in a subsequent shutdown.

### 7.4 Interference with ISIS

Operating MICE on ISIS requires the use of a target internal to the synchrotron that has an existing analogue control system. The use of this target has no material effect on ISIS operation other than causing a small amount of beam loss in the ring. This beam loss is monitored by detectors around the ring which are used to protect the machine.

## 8 Detectors

### 8.1 Overall description, functionality and redundancy

The MICE detector system as sketched in Figure 3.1 is described in this section, element by element. The driving design criteria are: i) robustness, in particular of tracking detectors, to potentially severe background conditions in the vicinity of RF cavities and ii) redundancy in particle identification (PID) to keep contamination below 1%.

Two spectrometers of very similar design, one upstream and one downstream of the cooling section, each measure the full set of six muon parameters. Each of them provides a high-resolution measurement of the five parameters of the muon helix in a tracker embedded in a 4 T solenoid, as well as a precise time measurement. In addition, muon/pion/electron identifiers (a  $t_0$  timing station and a small Cherenkov) are situated in front of the upstream detector and muon-electron identifiers (a larger Cherenkov and an electromagnetic calorimeter) are situated beyond the downstream spectrometer.

### 8.2 Scintillators for timing, trigger and upstream PID

Three fast time-of-flight (TOF) stations equipped with fast scintillators are foreseen. The first two stations (TOF 0 and TOF 1), upstream of the cooling section and separated by about 10 m, will provide the basic trigger for the experiment, in coincidence with the ISIS clock. These two stations have precise timing (around 70 ps) and will provide muon identification by TOF. The second of these stations will also provide the muon timing (relative to the RF phase) necessary for the measurement of the input longitudinal emittance. The coincidence with a third scintillator station of similar nature (TOF 2), downstream of the second measuring station, will select particles traversing the entire cooling section. The variation of emittance due to losses and decays will thus be distinguishable from cooling. The TOF 2 station will also record the muon timing for the measurement of the output longitudinal emittance. As discussed in [Janot01], a 70 ps resolution provides both effective (99%) rejection of beam pions and adequate ( $5^\circ$ ) precision in the measurement of the muon RF phase. Other design criteria are efficiency, redundancy and quality of calibration. The design presented here satisfies these requirements.

The three TOF stations are  $12 \times 12$ ,  $40 \times 40$  and  $40 \times 40$  cm<sup>2</sup> respectively. The two largest stations (TOF 1, TOF 2) are equipped with 8 scintillator slabs ( $40 \times 6 \times 2.5$  cm<sup>3</sup>) to make a plane (Y), by staggering and superimposing them at the edges for about 1 cm to allow cross-calibration with impinging beam particles. Bicron BC-404 scintillator material (with 1.5 ns decay constant and 1.7 m attenuation length) is the most suitable choice. The smallest station (TOF 0) could be made of two crossed planes (X-Y), each of two  $12 \times 6 \times 2.5$  cm<sup>3</sup> slabs, using BC-420 plastic scintillator, which is even faster than BC-404 but with a shorter attenuation length. Each slab is read out at both ends by a fast photomultiplier through a Plexiglas light guide. The time-of-flight measurement is achieved by combining leading-edge time measurements from a TDC with pulse-height information from an ADC.

TOF 0 will be equipped with Hamamatsu R4998 PMTs (0.7 ns rise time, 160 ps transit time jitter) or equivalent. The fringe fields of the spectrometer solenoid have been estimated by a Poisson-Superfish [Poiss] calculation to be as high as 1 T. The choice of the PMTs for TOF 1

and TOF 2 is therefore a critical issue. One option is to use the same R4998 PMTs but with a multi-layer mu-metal shield and a suitable design of the light guides. An alternative option is the Hamamatsu R5505 which can operate beyond 1 T but with a reduced gain. Similar solutions were successfully adopted in the BESS experiment [BESS].

Studies with several scintillation counters equipped with both types of PMTs will be performed at INFN Milano, INFN Padova, and in the free air bore of a large superconducting solenoid facility [LASA] at the INFN LASA Laboratory in Milano. A test beam at the CERN PS is also foreseen before a final decision is made. Funding for the initial phase of these tests has already been granted by INFN. For the time inter-calibration of a single detector plane, cosmic rays will be used with a dedicated set-up for the trigger (as done in the HARP experiment [HARPTOF]), or with beam particles passing in the overlap region of two nearby counters. The time monitoring of the system will be done with a laser-based system. Studies are under way to assess whether the expensive laser system [HARPlaser] used in HARP can be refurbished, or whether a similar one must be purchased.

The target of 70 ps resolution seems well within reach, as performance ranging between 50 and 90 ps intrinsic resolution has been published for TOF planes of similar dimensions [BESS, NA49]. Assuming that the electronics and calibration system of the HARP TOF wall can be re-used, a preliminary cost estimate for scintillator, PMTs and general reconfiguration would amount to about 200 k€ (see Table 8.1 for details). A layout with crossed (X-Y) planes is also under study for TOF 1 and TOF 2.

### 8.2.1 Ultra-fast time-of-flight system

Previous work within the Muon Collaboration addressed the need for an ultra-fast timing capability for an 805 MHz implementation of a muon cooling experiment. The need to tag muons arriving in phase with 805 MHz RF required a timing-tag precision of 10 ps or better. With a 201 MHz implementation of a cooling experiment, this requirement is not as stringent (as indicated above). Nonetheless, R&D on time-of-flight instrumentation capable of 10-ps resolution will continue. A prototype system will be tested in MICE to explore details of the muon longitudinal phase space that might not be accessible with the conventional plastic-scintillator time-of-flight system that will be the primary MICE TOF.

**Table 8.1:** Cost estimate for the TOF system (capital investment only).

Item	Cost (k€)
<b>Detector system</b>	
40 PMTs + mu metal	100
Scintillator (BC-404 and BC-420), light guides	15
Mechanics	5
<b>Calibration system</b>	
Laser	80 <sup>a</sup>
Optical system	15
Cosmic ray set-up	5
<b>Electronics</b>	
QDCs	10
TDCs	10 <sup>a</sup>
Scalers, MT, NIM modules, delay boxes, splitters	20 <sup>a</sup>
Crates, HV system, discriminators	30
HV cables, signal cables	10 <sup>a</sup>
<b>Total</b>	<b>300<sup>b</sup></b>

<sup>a</sup>These items may be recoverable at no cost from the HARP experiment.

<sup>b</sup>Total would be reduced to 180 k€ if all indicated items are recovered from HARP.

### 8.3 Upstream PID Cherenkov

Cherenkov detectors will contribute to particle identification for the MICE experiment. A small radiator with refractive index of about 1.25 will be used upstream to separate beam muons from pions and electrons of the same momentum on the basis of the difference in light yield. The upstream Cherenkov will reduce any background from electrons and pions that might be left after the time-of-flight selection has been made, for example, due to overlaps. A single 125 mm diameter cell of C<sub>6</sub>F<sub>14</sub> fluorocarbon liquid with a quartz window is proposed. An air light guide and 45° mirror would bring the light out to a single 125 mm photomultiplier tube. The total length of the device is 30 cm. The index of refraction of C<sub>6</sub>F<sub>14</sub> is 1.25 and it has thresholds of 0.7, 140, and 190 MeV/c for electrons, muons, and pions, respectively. Discrimination is achieved by pulse height analysis [Bartlett].

### 8.4 Tracking detectors

As discussed in Section 3, three precise measurement planes can provide adequate resolution in transverse and longitudinal momentum. Nonetheless, the tracking issues for single muons in MICE can become very problematic if the x-ray background from the RF cavities is too severe. The tracking detectors are therefore required to have low mass, to avoid photon conversions, and enough redundancy to separate signal hits from a potentially large background of photon hits.

Two options for the tracking detectors are being vigorously pursued by the MICE collaboration. They are both being prototyped and will be tested between now and summer 2003 in particle beams and in the vicinity of RF cavities. The final choice will be made based on the results of these tests, taking into account the relative performance and cost of the two proposed technologies. The expected date for decision is end of October 2003.

The first option utilizes scintillating fibres. Prototypes of this type of detector have already been exposed to RF cavity backgrounds in Lab G at Fermilab, and the performance estimate as a function of background rate, as well as the cost estimate, is reliable. The second option is a Time Projection Chamber with GEM amplification ('TPG'). The TPC principle and the GEMs are well established, but the combination is quite new. This is a promising technique with low material budget and high pattern recognition capability, but the effect of x-rays on the GEMs themselves remains to be evaluated, as does the immunity of the signal preamplifiers to electronic noise from the RF cavities. With either tracker choice, the upstream and downstream trackers would be identical.

#### 8.4.1 Baseline option: scintillating fibre tracker

##### 8.4.1.1 Operating principle

The scintillating fibre tracking option has a number of powerful features:

- it can operate effectively at very high background rates
- it is immune to electromagnetic interference
- it is totally passive and therefore poses little risk when operated near liquid hydrogen

Figure 8.1 illustrates the mechanical arrangement of one tracker. The five planes will be supported in a rigid tube so that the whole assembly can be slid into (or out of) the spectrometer solenoid. Two five-plane scintillating fibre trackers are envisioned, each plane consisting of three sets of fibre doublets at  $120^\circ$  to each other (see Figure 8.2).

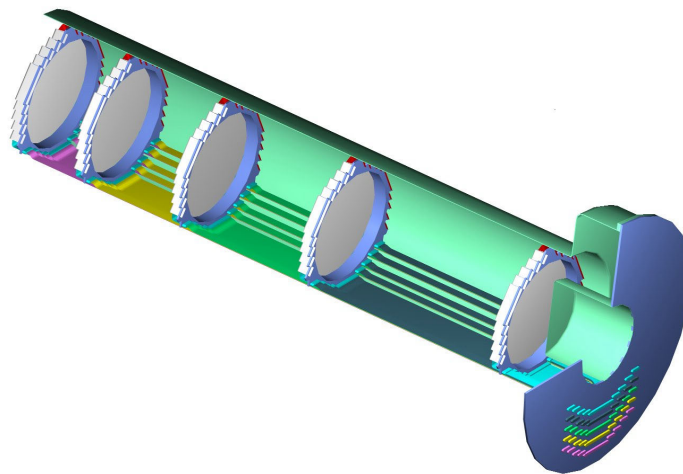


**Figure 8.1:** Engineering representation of 5 station fibre tracker

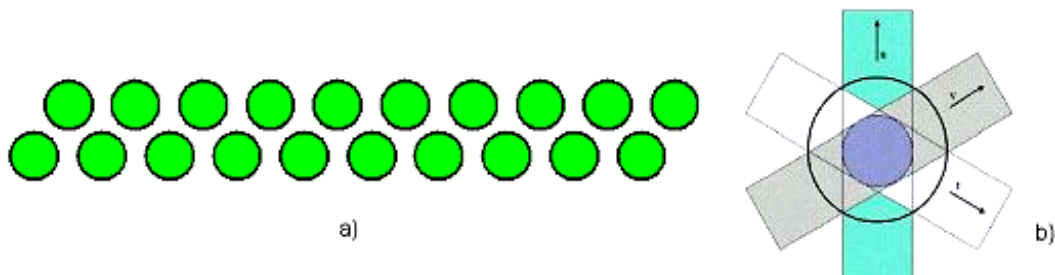


**Figure 8.2:** a) Ribbon doublet structure; b)  $u-v-t$  fibre plan

This structure will give efficient space-point reconstruction, since hits in any two of the three doublets suffice. Each doublet consists of two overlapping layers of round fibres, giving 100% geometrical coverage over the face of the detector and an approximately uniform thickness of scintillator, independent of where a particle crosses the doublet. This structure also suppresses the effects of background photons since a photon interaction is not likely to produce a triplet hit in a fibre plane. Each detector plane will have an active area that completely encloses a 30-cm-diameter circle. Figure 8.2 shows the fibre ribbon doublet structure and a typical  $u$ - $v$ - $t$  readout plane. Scintillation light from the fibre will be piped to the photodetectors using clear fibre light guides of a length not to exceed 3 m. The photodetector of choice is the Visible Light Photon Counter (VLPC), due to its high quantum efficiency (85%) and high gain (50,000). This design is inspired by that of the D0 Fibre Tracker's [D0] VLPC system. To minimize the effects of the background x-rays, the smallest fibre that yields enough light for efficient tracking will be used. Based on results from D0, 350  $\mu\text{m}$  fibre diameter seems acceptable, given the short active length (30 cm) of the MICE tracking planes and the relatively short light guides in comparison to those used in the D0 Fibre Tracker. Fibre ribbons made with both 500 and 350  $\mu\text{m}$  fibre are currently being prototyped. The light yield from these prototypes will be measured with a 32 channel VLPC system using cosmic rays.

**Table 8.2:** Fibre tracker parameters

Fibre diameter [ $\mu\text{m}$ ]	350
Fibre pitch/diameter in ribbon	1.2
Views per plane	3
Radiation length per plane [% $X_0$ ]	0.35
Planes per spectrometer	5
Total number of fibres (approx.)	42,900
Estimated light yield per singlet [p.e.]*	8

\* p.e. = photoelectron

As noted above, coping with the high background rates from the RF cavities and providing redundancy dictate that the upstream and downstream tracker each comprise five fibre-tracking planes. Each plane will consist of the triplet-doublet structure described above, using 350- $\mu\text{m}$ -diameter fibres. Given a fibre-ribbon pitch to diameter ratio of 1.2, a total of 42,900 fibres are required to instrument the 30-cm-diameter area using five planes in each of the trackers. The additional radial space needed to bring the fibre ribbons to the readout electronics is less than 5 cm.

#### 8.4.1.2 Tracking studies

Details of the Monte Carlo simulation that was performed to study the fibre tracker's performance in a high-background environment are given in Section 9; a few salient points are given here. The five-plane fibre tracker is very insensitive to photon backgrounds from the RF cavities and maintains its excellent tracking performance at rates significantly higher (260  $\text{kHz}/\text{cm}^2$ ) than that expected in MICE based on current measurements. Representative results for the measured helix radius are shown in Figure 8.3 for incoming (upper plot) and outgoing (lower plot) muons. There is no cooling channel in this simulation (which corresponds to step III in Figure 3.13) so both plots should be identical. We see that the distributions in (generated minus reconstructed) radius are unaffected by background photons over a wide range in photon rate, illustrating the robustness of this tracking approach.

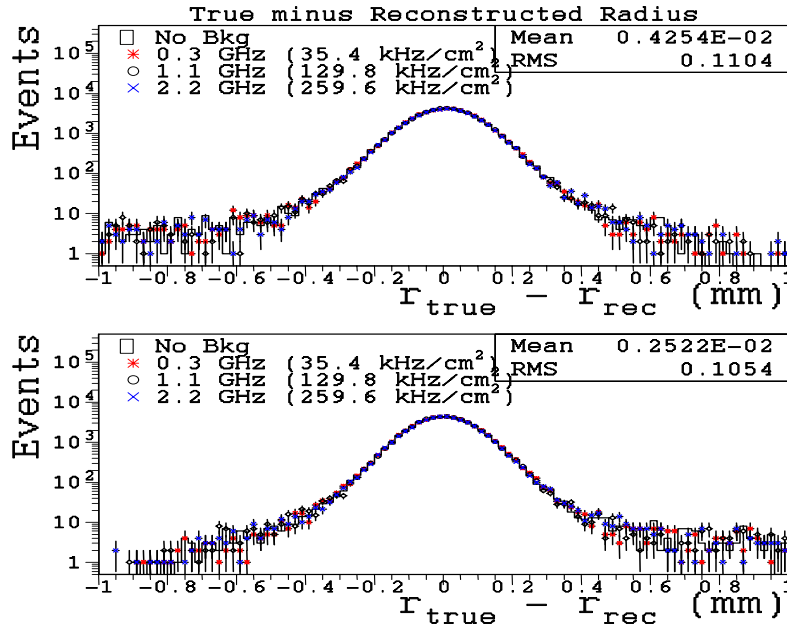


Figure 8.3: Monte Carlo tracking results for the fibre tracker as a function of background rate.

#### 8.4.1.3 Readout electronics

The readout planned for MICE uses the D0 VLPC system. A total of 44 D0-type 1024-channel VLPC cassettes are required. No new engineering is needed and the available infrastructure at Fermilab can be used for VLPC cassette production. A new order for VLPCs will have to be initiated with the vendor, however. Also, the D0 cryogenics design will be used for MICE. The current design calls for two D0-type VLPC cryostats each holding approximately 22,000 channels (22 cassettes) of VLPC readout. One cryostat will service the upstream tracker and one the downstream tracker. This configuration allows minimization of the fibre light guide length, thus maximizing light yield and reducing fibre costs. Each VLPC cassette uses two 512-channel readout boards. The existing boards currently used in the D0 experiment provide analog and trigger bit (digital) information from the VLPCs, temperature and bias control, and calibration. D0 is currently working on a new front-end design that will allow for higher readout rate and include the possibility of adding timing information (with 1-2 ns precision) for each hit. The MICE collaboration plan to work with D0 on this effort, with the hope that a single final design can be used for both experiments.

#### 8.4.1.4 Cost and schedule

The cost estimate is based on the experience of the D0 experiment. Costing for the ribbons, support structure, wave guides, etc. follow the MICE design as outlined above. The full hardware cost for the 43,000-channel fibre tracker is estimated to be 4.1 M€. Construction of the fibre tracker is estimated to take approximately 2 years. The tracker could, therefore, be ready by the beginning of calendar year 2005.

#### 8.4.1.5 Low RF background scenario

If it turns out that the backgrounds from the RF cavities can be kept at a low level, the cost and the channel count of the fibre tracker can be reduced by multiplexing the fibres. The readout of the scintillating fibres into the VLPCs can then be multiplexed as illustrated in Figure 8.4.

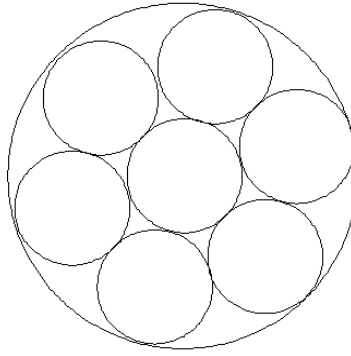


**Figure 8.4:** Fibre multiplexing scheme

Seven 350  $\mu\text{m}$  fibres can be multiplexed into one VLPC pixel. There would only be about a 10% loss of light in the outer ring of fibres due to a slight mismatch. This implementation of the fibre tracker would be provided by a 7:1 multiplexing wave guide, so as to retain the capability of reading out each fibre individually should there be a need to cope with higher background situations at a later stage. To implement individual readout would then require that the wave guides be changed and additional readout channels be purchased, but the tracker itself would remain unmodified. This scenario has a number of nice features. First, if the backgrounds are low, MICE can run in this configuration and the system channel count (and therefore cost) can be substantially reduced. If the experiment is pushed to run at high RF fields, and backgrounds become a problem, the trackers themselves would not have to be rebuilt. The cost saving with 7:1 multiplexing is approximately 3 M€. The fibre tracker system would then cost about 1 M€.

#### 8.4.2 Tracking device option II: Time Projection GEM chamber

This detector has been proposed [Gas02] with the acronym TPG (Time Projection chamber with GEM amplification [GDD02]). The ionization electrons generated by the muon in a gas volume 1 m long and 30 cm in diameter will be drifted along an electric field parallel to the magnetic field, and multiplied by a factor  $10^4$  to  $10^5$  in a set of three gaseous electron multipliers (GEMs). (A GEM [Sau97] is a structure in which high gas gain results from the concentration of electric field at the edges of small holes bored in a thin double-clad plastic foil, across which a high voltage is applied.) The readout plane, called a hexaboard [Bre98, Sau01, Bac02], is made of hexagonal pads arranged to form three sets of strips oriented at  $120^\circ$  to each other. The TPG technique offers the following features:

- with the choice of a light gas mixture ( $\text{He-CH}_4$  or similar), the detector offers little multiple scattering and low absorption of x-rays
- the response for all particles entering the detector is uniform
- a large number of space points ( $\geq 100$ ) is generated for each muon, each with a spatial resolution in the transverse plane  $\Delta x < 400 \mu\text{m}$ , offering exceptional pattern recognition capabilities even in the presence of high background
- the application of GEM technology into a TPC [GDD02] has the advantage of minimizing the positive-ion feedback into the drift region as well as the  $\mathbf{E} \times \mathbf{B}$  effects in the readout system

These features are potentially offset by the fact that, during the rather long drift time of the order of 50  $\mu\text{s}$ , the signals from a given muon will be collected together with x-ray noise or

with the signals from previous or following muons. In addition the effect of x-rays on the GEMs themselves must be evaluated.

#### 8.4.2.1 Detector structure

Figure 8.5 shows the main components of the upstream TPG. The detector is supported by a sturdy cylindrical tube of insulating material that can be inserted in one piece into the spectrometer solenoid. The field cage design could be similar to that of the HARP-TPC [HAR02]. It will be designed for a high voltage of 80 kV.

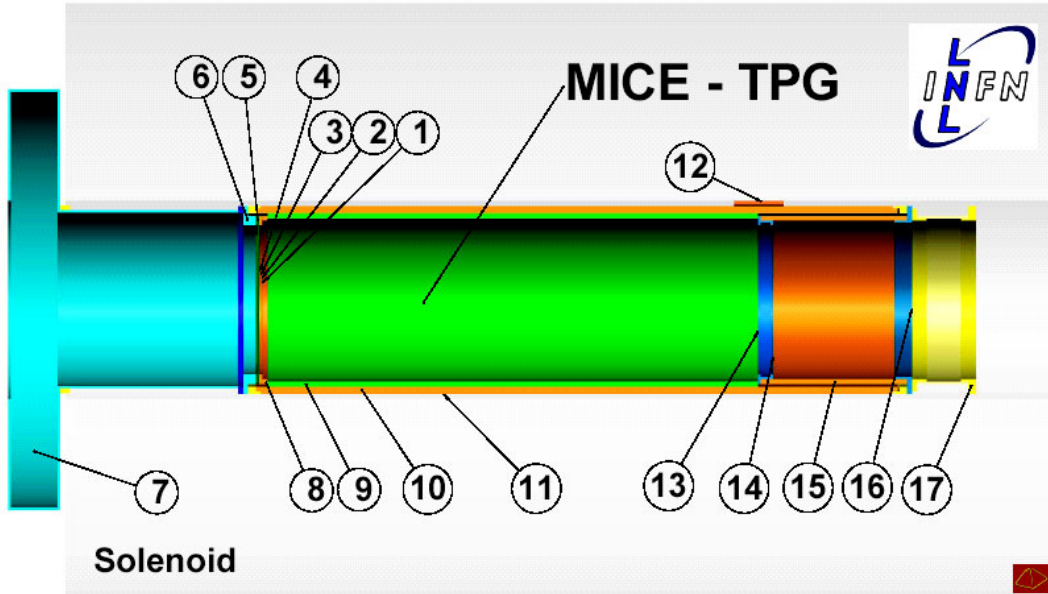


**Figure 8.5:** MICE-TPG upstream detector. Muon beam enters from the left. 1: GEM-1 foil; 2: GEM-2 foil; 3: GEM-3 foil; 4: hexaboard; 5: Board (for hexaboard support, gas seal and signal connectors); 6: readout flange; 7: front-end electronics support and EM shield; 8: field cage termination; 9: field cage; 10: TPG isolating container; 11: TPG peripheral grounded shield; 12: HV inlet for drift electric field; 13: HV thin metallized foil cathode; 14: HV thin metallized foil gas seal; 15: HV foil support (insulating tube); 16: grounded thin foil seal; 17: TPG-LH<sub>2</sub>-absorber integration connection flange (schematic).

The drift volume is 1 m long; it is delimited upstream by the first GEM foil (GEM 1) and downstream by a thin metallized cathode foil attached at the (negative) HV side of the field cage (13 in Figure 8.5). The TPG is decoupled from the LH<sub>2</sub> absorber safety area by an inert gas volume about 30 cm long, closed by thin metallized foils on both ends (14) and (16).

To minimize multiple scattering and photon conversions a low-Z gas is preferred for the TPG. The best candidate is a He-based mixture, as in KLOE [Adi02]. Tests of operation with various mixtures are planned. In the following, a mix of He/Iso-butane 90/10 with a drift field of 50 kV/m is assumed, providing a drift velocity of 1.7 cm/μs.

On the upstream side, the TPG is closed by the three GEM foils and the hexaboard. The material budget here is not critical, since the muons traverse this plane before the input emittance measurement or after the output emittance measurement. For reasons of flexibility, safety and redundancy, a triple-GEM structure will be used, following the experience of COMPASS [Alt 02]. GEM foils are 50 μm thick, with 5-μm-thick Cu coverage and 60-μm-diameter holes etched in a hexagonal pattern with a pitch of 150 μm. The separation of the GEM foils is provided by 2-mm-thick spacers.



track are shown with the same colour. Figure 8.7 (bottom) shows helical trajectories fit to the identified tracks. The HARP pattern recognition and track fitting programs were used with very little modification.

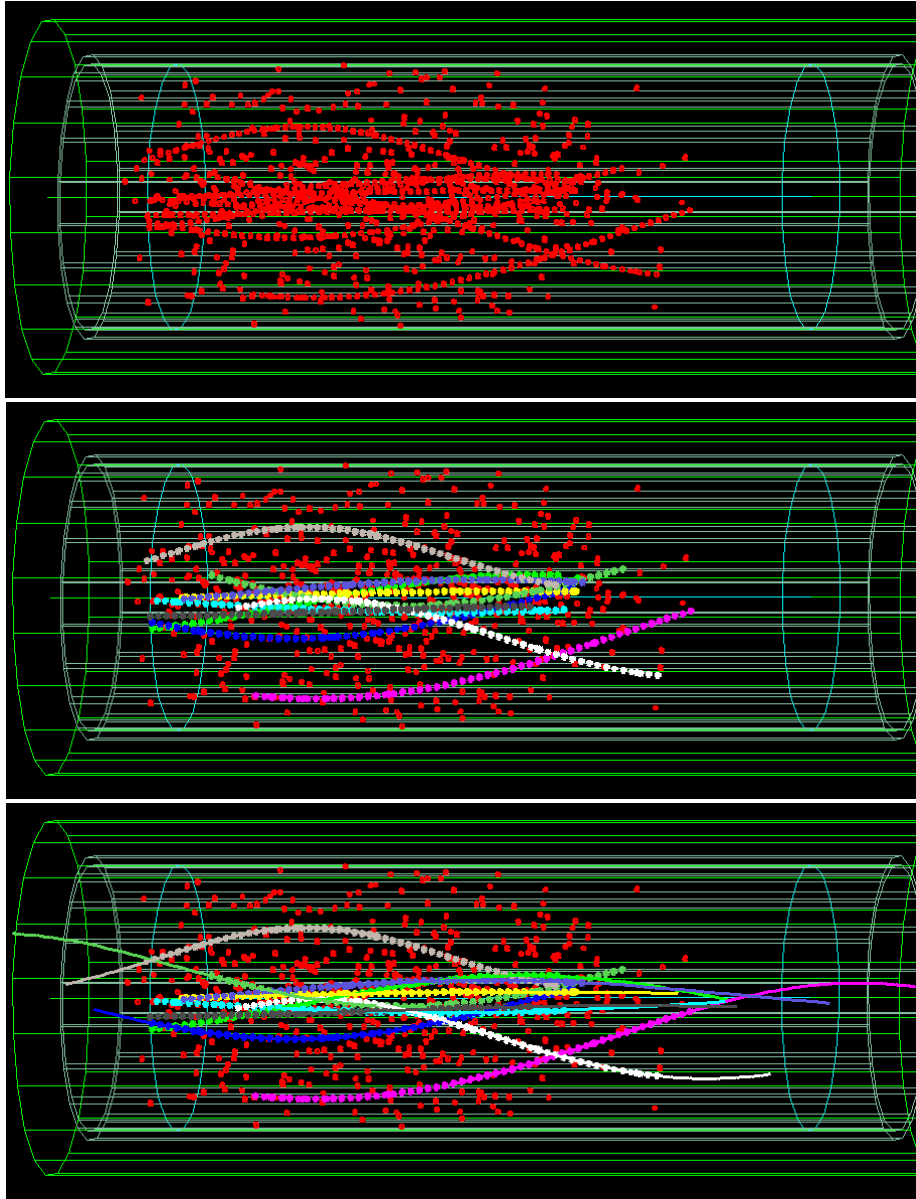


**Figure 8.7:** top: simulated track and noise hits in the TPG; middle: highlighted hits are those assigned by the pattern recognition to belong to the same track; bottom: track fitted on the selected hits.

#### 8.4.2.3 TPG R&D test programme

Tests of GEM response with the envisaged gas mixture and front end electronics are underway with a small GEM chamber constructed in Napoli. This device will then be exposed to a source of RF electromagnetic radiation to test the shielding, and to an RF cavity to evaluate the effect of x-ray radiation.

One full TPG readout system (with hexaboard and triple-GEM structure) will be built, and equipped with the full front-end cabling and preamplifier electronics. Its functionality will first be tested in the lab. It will then be plugged into the HARP-TPC field cage for cosmic-ray

and beam tests in the HARP-TPC solenoid. The goal is to observe and measure charged particle tracks in the available 1.5-m-long field cage immersed in a magnetic field of 0.7 T.

The conceptual design of the TPG is ready. The engineering of the readout flange and of the adaptation to the HARP-TPC field cage are under way, and will be ready in January 2003. Construction of the readout flange and of the adaptation to the HARP test-bed should be completed by April 2003. Lab tests of the hexaboard and GEM components should be completed by June 2003. Installation into the HARP test-bed and beam tests should take place in summer 2003.

#### 8.4.2.4 Cost estimates and responsibilities

The TPG development is carried out by the University of Geneva, INFN Bari, INFN Legnaro, INFN Napoli and INFN Trieste. The cost estimate is as follows: readout structure (3 GEMs, spacers, hexaboard and mechanics of the gas and HV inlets, preamplifiers) is 100 k€ per TPG (estimate for the first prototype); field cages are 70 k€ each (extrapolation from the HARP construction); ancillaries, gas and HV supplies are 30 k€; FADC electronics is 610 k€, most of which will be recovered from HARP. The total estimated cost for the TPG system is 980 k€, of which more than 500 k€ is covered by already existing parts.

## 8.5 Downstream PID (e- $\mu$ separation)

In a small (~1%) fraction of events, a muon decays inside the cooling section or one of the spectrometers. The resulting electrons bias the emittance measurement considerably and must be rejected. Momentum distributions of electrons and muons arriving downstream of the second spectrometer are shown in Figure 8.8.

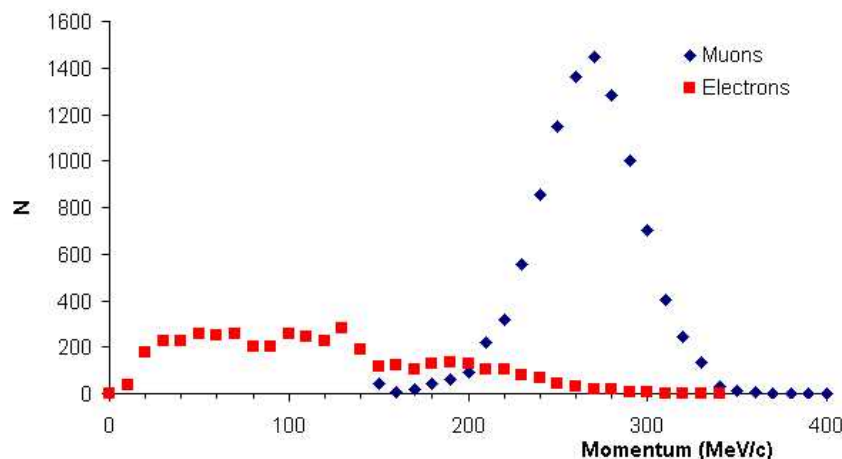


**Figure 8.8:** Momentum distributions of muons and electrons downstream of the second spectrometer [Janot01].

Kinematics cuts can reject about 80% of decay electrons, but this rejection is not sufficient to avoid a bias in the emittance measurement. Dedicated detectors are needed to separate electrons from muons. The strategy is as follows:

- a) positively identify muons by requiring low and longitudinally uniform energy deposition in an electromagnetic calorimeter at the very end of the experiment

- b) reject any residual background of electrons in the muon sample defined by the calorimeter by means of a threshold Cherenkov detector immediately upstream of the calorimeter

Geometrical features of these particle identifiers are determined by the angular and spatial distributions of particles at the end of the experiment. The profiles in position and angle 50 cm downstream of the solenoid, obtained from simulations, are shown in Figures 8.9 and 8.10. A geometrical aperture of order 1 m is needed to take into account the defocusing of particles in the stray magnetic field of the downstream solenoid.

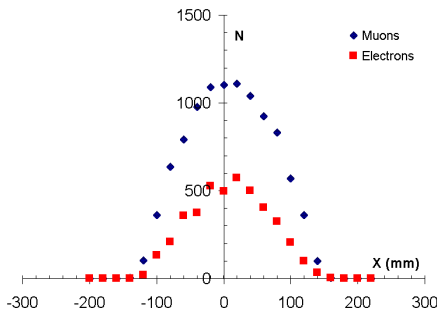


**Figure 8.9:** Particle spatial distributions in a plane perpendicular to the beam axis [Janot01]

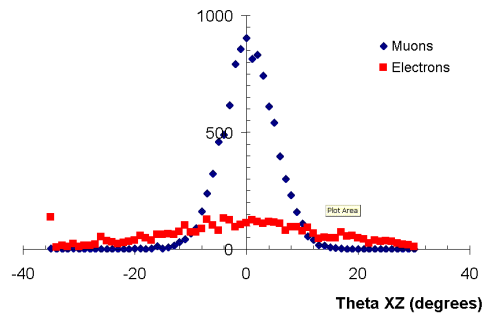


**Figure 8.10:** Particle angular distributions in a plane perpendicular to the beam axis [Janot01]

## 8.6 The electromagnetic calorimeter

A state-of-the-art, high-resolution electromagnetic Pb-scintillating fibre calorimeter, of the type built by KLOE [KLOE], is proposed. It offers adequate energy resolution to perform muon and electron identification in the momentum range of interest for MICE.

### 8.6.1 Structure and layout

The proposed calorimeter, built by gluing 1-mm-diameter blue scintillating fibres between 0.5-mm-thick grooved lead plates, has uniform and symmetric Pb-scintillating fibre structure, with fibre spacing of 1.35 mm. When layers are superimposed, fibres are located at the vertices of adjacent quasi-equilateral triangles, forming a homogeneous and compact structure with a fibre:lead:glue volume ratio of 48:42:10. The resulting composite, with a density of  $\approx 5 \text{ g cm}^{-3}$ , a Moliere radius of  $\approx 3.5 \text{ cm}$ , a radiation length  $X_0$  of  $\approx 1.5 \text{ cm}$  and a sampling fraction of  $\approx 15\%$  for a minimum ionizing particle, gains considerable stiffness, and can be easily machined to the shape required for the final assembly.

This ‘spaghetti’ design offers the possibility of fine sampling and results in optimal lateral uniformity of the calorimeter. Fibres run mostly transversely to the particle trajectories, reducing sampling fluctuations due to channelling, i.e., showers developing along the fibres’ direction, an effect particularly important at the low energies of interest. Finally, the very small lead foil thickness ( $< 0.1 X_0$ ) results in a quasi-homogeneous structure and a high efficiency for minimum ionizing particles and low energy electrons.

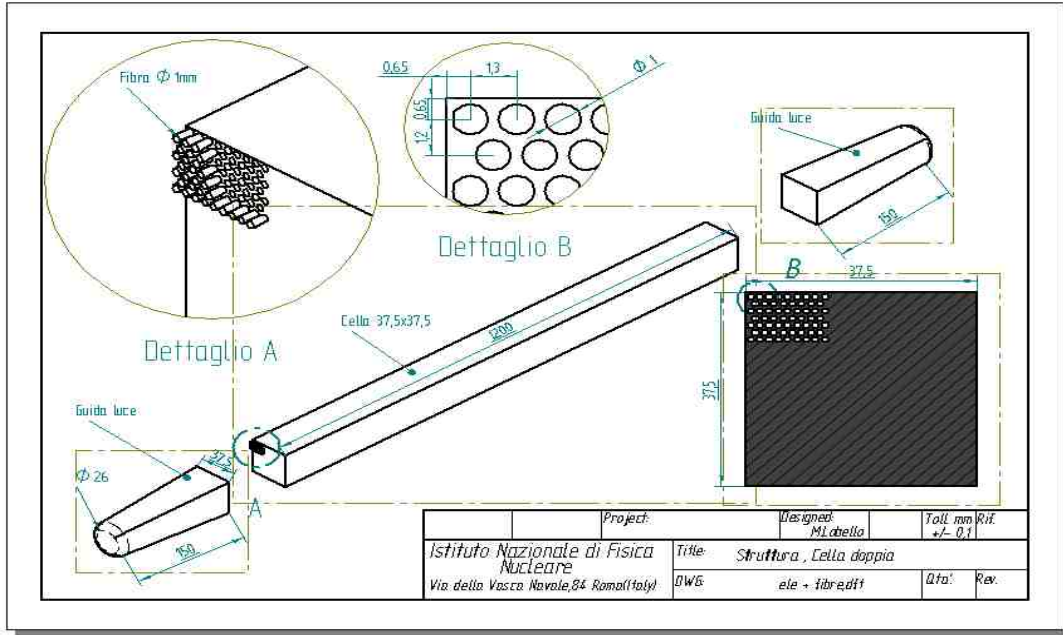


Figure 8.11: Internal structure of the electromagnetic calorimeter.

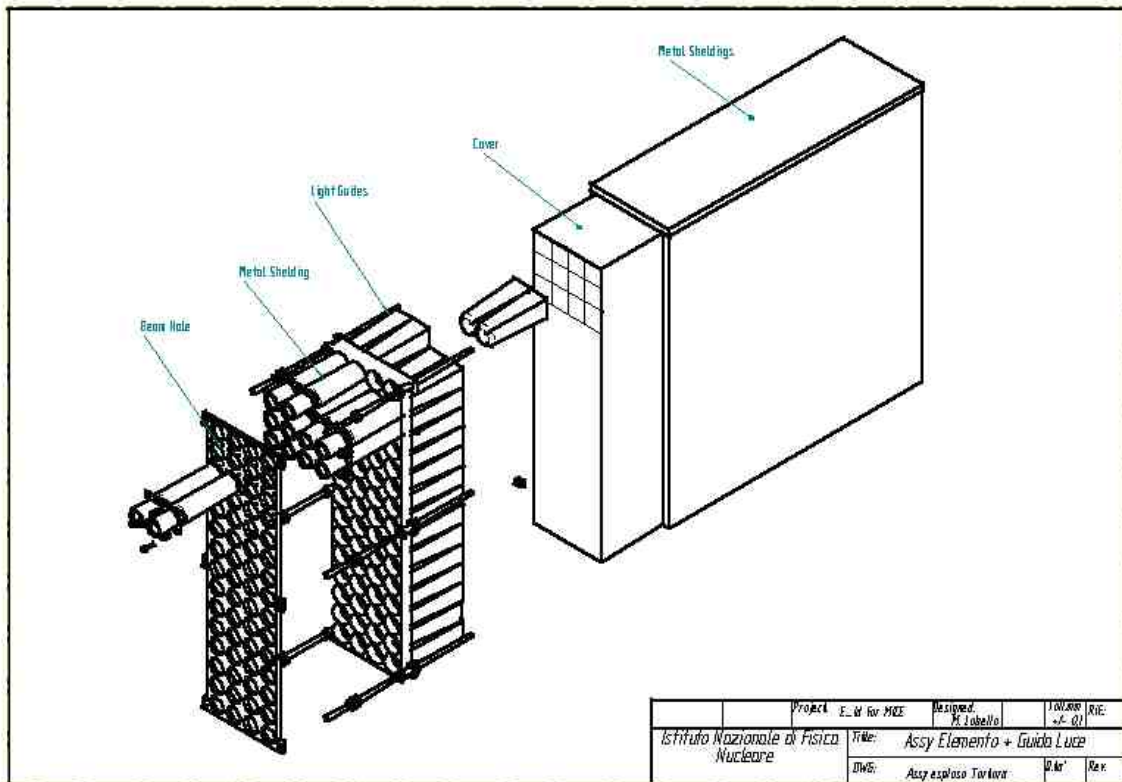


Figure 8.12: Electromagnetic calorimeter assembly drawing (one side, readout view).

A calorimeter module of  $120 \times 120 \text{ cm}^2$  area, 15 cm thick, consisting of  $\approx 125$  lead and fibre layers, can be built using the facilities of the Frascati (LNF) workshop formerly used for the construction of the KLOE electromagnetic calorimeter [KLOE]. The lead and fibre planes are perpendicular to the beam axis. The calorimeter is structured in four layers, each made of 16

cells  $3.75 \times 3.75 \text{ cm}^2$  wide and 120 cm long. Its basic features are shown in Figures 8.11 and 8.12.

### 8.6.2 Fabrication of components

The grooved lead foils are obtained by rolling 0.5-mm-thick foils in a special shaping machine. Based on KLOE experience, the optical fibres will be Pol.Hi.Tech. type 046 [POL], emitting in the blue-green region and meeting, at reasonable cost, the MICE technical specifications. Great care will be taken to maximize the efficiency of the light collection system and to ensure uniform photocathode illumination. KLOE experience suggests light guides consisting of a tapered mixing part, where the quadrangular entrance face transforms smoothly to its inscribed circle, plus a Winston cone concentrator [Welford], matching the area of the calorimeter element to the sensitive area of the photocathode face. If it is possible to shield against the residual magnetic field, a suitable readout choice, at both ends of each cell, is the 1-1/8 inch R1355 Hamamatsu phototube. This tube, already used in the HARP experiment, has a transit-time spread less than 1 ns. In this case, the area concentration factor is  $\approx 2.65$ , with a light collection efficiency of  $\approx 85\%$ .

### 8.6.3 Front-end electronics

The deposited energy will be digitized by conventional ADCs, e.g., the VME CAEN 792, already used in the HARP experiment. An unbiased cross-calibration of all calorimeter readout elements will be obtained both from cosmic rays and test-beam muons. A rough measurement of the impact point on the calorimeter will be derived from the ratio of pulse heights on two ends of the fired cell.

### 8.6.4 Energy and timing resolution, particle identification.

The fibres have a decay constant of  $\approx 2.5$  ns, an attenuation length of  $\approx 3.5$  m, and a yield of about 80 photoelectrons per minimum ionizing particle (mip) crossing one of the  $3.5 \times 3.5 \text{ cm}^2$  calorimeter cells at a distance of 20 cm from the photomultiplier.

Based on the response of the KLOE electromagnetic calorimeter [Adinolfi] to electromagnetic showers of similar energies at the DAΦNE  $\phi$ -Factory, the expected energy resolution is  $\approx 5\% / \sqrt{E[\text{GeV}]}$ , fully dominated by sampling fluctuations. The time resolution was measured in KLOE, with modules 4 m long, and is also very good,  $\sigma_t \approx 54 \text{ ps} / \sqrt{E[\text{GeV}]}$ , giving a precise measurement of the impact point along the fibre. The KLOE calorimeter test-beam data [Antonelli] show that distributions of total energy are Gaussian, with almost no tails. The response of the calorimeter to electrons and photons in the energy range 20–300 MeV is linear, independent of incident angle [Antonelli]. The signal deposited by a minimum ionizing particle in a  $3.5 \times 3.5 \text{ cm}^2$  cell is equivalent to that of a 27 MeV electron or photon. In the momentum range of interest for MICE, muons mostly punch through, whereas electrons leave basically all their energy in the first two layers. In combination with the downstream Cherenkov, the measurement of energy deposition and of its longitudinal profile in the calorimeter should provide an electron rejection of  $\sim 10^{-3}$ .

Cosmic ray tests are foreseen together with tests of detector response to low energy electrons, hopefully at the Beam Test Facility in the DAΦNE complex of LNF [TBF].

### 8.6.5 Construction schedule

INFN technical manpower will groove the lead foils, mould the light guides, and design and fabricate the mechanical supports for photomultipliers and patch panels. The precise schedule must be negotiated with the Pisa group, who are members of the AMS experiment and currently the main users of the lead-grooving machine at LNF. Some refurbishing and tuning of the KLOE tooling machinery will be needed. Construction of light guides, production of fibres, gluing of layers of lead with fibres, machining of the assembled modules and final gluing of light guides will be contracted to external firms. The completion of the construction project will take one year after approval of funding.

### 8.6.6 Costs

The expenditure needed to build the MICE calorimeter – 15 cm thick – is estimated to about 170 kEuro plus 30 additional Keuros for ADC's. This includes the purchase of lead foils, fibers, glue, light guides and relative workings. The entire readout chain, except the ADC's, worth about 150 additional Keuros (256 photomultipliers & voltage dividers, cables, front end electronics and VME crate) will be recuperated from HARP.

## 8.7 The downstream Cherenkov $e/\mu$ separator

Further electron rejection will be provided by the downstream aerogel Cherenkov detector. This detector should not be affected by background from the RF cavities, as x-rays will rarely be high enough in energy (above 2 MeV) to produce electrons that give Cherenkov light in the aerogel. The RF noise at 201 MHz has a skin depth of 6  $\mu\text{m}$  in aluminium; shielding of the photomultiplier tubes will be necessary, but straightforward.

### 8.7.1 Description and performance

In the momentum range of interest to MICE, aerogel ( $1.01 < n < 1.06$ ) appears to be the only adequate radiator from which to build a threshold Cherenkov blind to the passage of muons. The choice of the appropriate index of refraction for the radiator is governed by the relative light yields of electrons and muons, and their respective detection efficiencies assuming a fixed detection threshold. The goal is to maximize the response to electrons while minimizing possible contributions from higher energy muons. The aerogel radiator proposed here has an index of refraction  $n = 1.02$  and a total thickness of 10 cm. The transverse size is  $90 \times 90 \text{ cm}^2$ . This geometrical aperture is deliberately chosen to safely account for the increase, due to the magnetic field profile, of the rms beam envelope.

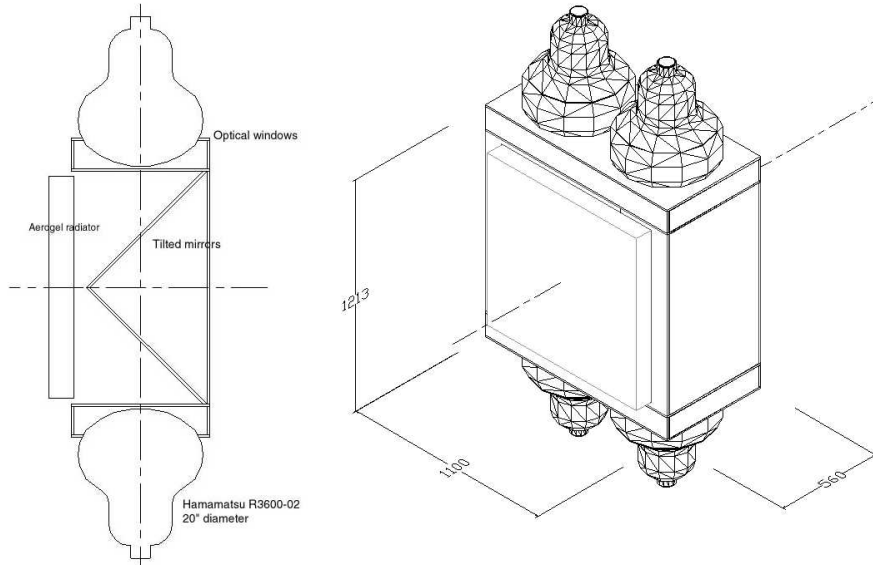


**Figure 8.13:** Meridian cut through the optical system and perspective view of the set-up.

For reasons of availability, cost and handling, all inner surfaces potentially hit by light are constructed from aluminized PMMA plastic sheets or (more expensive) optical glass plates. The reflectivity of the aluminized plastic sheets is taken to be about 90% (as used for the Cherenkov detector of the HARP experiment). A plane mirror, tilted at  $45^\circ$ , reflects light at  $90^\circ$  to the optical beam axis towards the photodetectors. The mirror can also be made from aluminized PMMA plastic or optical glass.

The proposed system uses Hamamatsu R3600-02 20-inch-diameter photomultipliers, with a standard bi-alkali photocathode (the same ones as used in the Super-Kamiokande experiment). This PMT has the advantage of a rather large gain,  $3 \times 10^6$ , well matched to the low light yield of aerogel radiators.

Due to the large bore of the solenoids, detailed studies are needed on how best to shield the PMTs from stray magnetic field. The gas-tight external box enclosing the optical system will be constructed from nickel-plated soft steel. An additional heavy iron wall (with an adequately large opening for the particles) is foreseen in front of the device (not shown in the figures). Should this be insufficient, one solution would be to locate the PMTs farther from the beam axis. Additional precautions (thin lead shielding and  $10\text{-}\mu\text{m}$ -thick copper cladding) will be taken to account for the possible x-ray and RF backgrounds.

Optical characterization of the whole set-up was performed by accurate 3D optical ray tracing, taking into account realistic surface properties of the mirrors (spectral and angular reflectivity), bulk scattering inside aerogel materials, transmittance of the window and the typical quantum efficiency of standard photomultipliers. The overall light collection efficiency reaches about 80%. On the basis of the light collection and the photoelectron yield, the detection efficiency for electrons versus their momentum has been evaluated (Figure 8.).

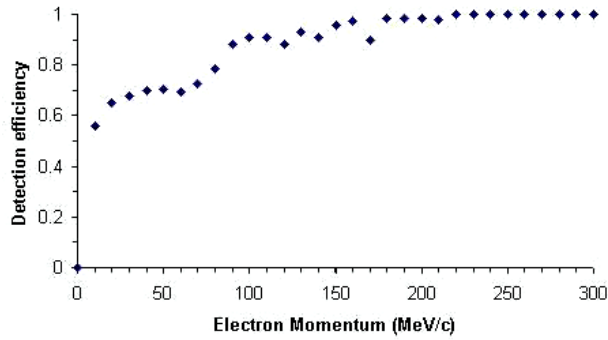


**Figure 8.14:** Electron identification efficiency vs momentum

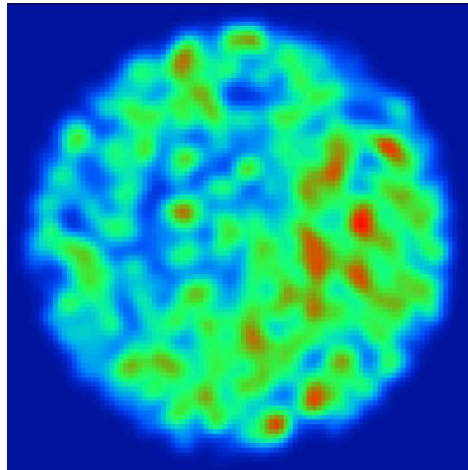


**Figure 8.15:** Downstream Cherenkov light collection on the surface of the photomultiplier tube.

A graphical summary of the results from the optical studies is shown in Figure 8. as a false-colour intensity distribution on the photocathode of the R-3600 photomultiplier. The overall light collection efficiency exceeds 77% assuming no polarization-dependent reflections.

### 8.7.2 Cost estimates

Cost and schedule details for the downstream Cherenkov system are given in Table 8.3.

**Table 8.3:** Cost and schedule estimate for the downstream Cherenkov

Item	Supplier	Delivery	Costs (k€)
Aerogel	Matsushita		100
Glass plates, aluminization, supports	Schott + CERN	16 weeks	21
Containment vessels, welding, Ni plating, supports	Pegard		25
Assembly and testing			4
5 photomultipliers R3600-02	Hamamatsu		40
Positive HV supply	CAEN		6
Mu-metal shielding	Imphy		4
Slow controls (sensors...)			4
Transportation, shipping, misc.			2
Sub-total			206

An alternative design for the downstream Cherenkov based on the Belle Cherenkov detector [Suda], significantly thinner but featuring a higher channel count, was also investigated. The approach described above was ultimately selected as the baseline option for MICE.

## 8.8 DAQ, trigger, on-line monitoring

### 8.8.1 Beam structure and trigger

The ISIS beam delivers a 1 ms spill of about 3000 pion bunches, each 100 ns long and separated from its neighbours by 224 ns, with a repetition rate of few Hz. The RF power source can be operated with a duty-factor of about  $10^{-3}$ . Using it in the most efficient way delivers a flat top of 850  $\mu$ s at 1 Hz, during which 2600 bunches will reach the experiment.

The basic enable signal to data-taking will be provided by the start of operation of the MICE RF cavities (Start-Of-RF, or SORF). It will last until the End-Of-RF (EORF) signal, for a data-taking gate of typically 500  $\mu$ s. (Because of the high level of multipacting during the RF transient, the detectors must be insensitive during the rise- and fall-time of the RF pulse, so the data-taking gate is shorter than the RF pulse.) This gate will be generated by the MICE trigger system.

The time structure of the beam is such that there is not enough time for particle-by-particle readout. For this reason, all digitisers will be buffered during the spill and read out by the DAQ system at the end of the data-taking gate. The storage capabilities of the digitisers may put limits on the duration of this gate. ADC gates and TDC stops will be generated by simple coincidences of TOF planes. The RF phase and characteristics of the RF pulse will be recorded at the same time as the muon events.

For calibration and reference purposes, one or several SORF/EORF data-taking gates can be generated, with beam but without RF, between the real SORF/EORF cycles.

The trigger system will be designed to provide enough flexibility to allow the detectors to run in stand-alone mode for set-up, test and calibration purposes. Specific tests for the choice of a suitable trigger receiver may be performed during the TPG test at CERN in 2003.

### 8.8.2 Working hypothesis: event rates and sizes

- The maximum beam rate will be 1 particle per bunch. This is a limiting case, in which there will often be more than one particle in a 100 ns time window.
- One calibration (RF off) cycle will be taken per normal (RF on) cycle
- The upstream spectrometer will have to measure out-of-acceptance and out-of-RF-phase particles
- For the purposes of evaluating the data rates, it has been assumed that only 1/4 of the incoming particles will fall into the acceptance after the diffusing plates and will be able to reach the downstream spectrometer.

- While the Sci-Fi tracker is relatively insensitive to the x-ray background, the data size from the TPG may change dramatically as the background conditions vary. For this reason, the total data volume from the TPG has been evaluated for the case of 50% occupancy over the whole detector.

### 8.8.3 Readout volumes and network structure

All the digitizers will be housed in VME crates, either 6U or 9U. As can be seen from Table 8.4, no crate exceeds the maximum sustained rate attainable on a standard VME bus.

**Table 8.4:** Data volume for the MICE detectors.

<b>Subsystem</b>	<b># VME crates</b>	<b>Data volume</b> [MB/s]	<b>Data volume/crate</b> [MB/s]
TPG	3 front + 3 rear	$\leq 12$	$\leq 2$
Sci-Fi	$\approx 30$	$\leq 2$	$\leq 0.5$
TOF	1 front + 1 rear	$\leq 0.5$	$\leq 0.25$
e/ $\mu$ -ID	1 rear (same crate as TOF?)	Negligible	—

Each crate will be equipped with a VME processor, which is a single-board computer provided with a VME interface and a network connection. The task of the processor will be to read data out of the digitizers via the VME bus, and to pass them over the network to the Event Builders.

As is now commonplace, the MICE DAQ system will make use of a switched Ethernet network for transferring data to the Event Builders and the Storage System, to synchronize and control the DAQ processes running on several nodes and to perform on-line monitoring tasks.

To cope with the total rate of the experiment and to allow for redundancy, the DAQ will comprise at least 2 Event-Builder (EVB) computers. Their role will be to assemble event fragments produced by the many VME readout processors, make consistency checks, write assembled events to the Storage System, and serve live data to the On-Line Monitoring System. In order to minimize the cost of data storage, the possibility of building enough parallelism and computing power into the EVB system to perform on-the-fly data compression will be considered and tested.

The most widespread storage solutions for scientific laboratories are rack-mount PC cases holding several large-capacity, hot-swap E-IDE hard disks, connected to the PCI bus by hardware-RAID controllers, with an available capacity of  $\sim 1$  TB [Sanders].

The performance of such systems can be considered appropriate for the MICE data rate; however, some care has to be taken since the on-line Storage System will not only provide space for storing runs, but will also serve data for on-line analysis work. For this reason, the hardware will have to be tested for concurrent sequential read/write access of large files before being considered compliant with MICE rate requirements.

MICE will be able to cool, at most,  $100 \mu\text{s}$ . To achieve a statistical precision of  $10^{-3}$ , one has to take data for 1000 seconds. During this time the detector will produce up to 15 GB of data. Storing a week of data, hundreds of runs, may require several TB. The availability of a

centralized storage system at RAL would be a great help by reducing the on-line storage system complexity and eliminating the need for a high-performance backup system.

Several workstations will be available for monitoring data, either spilled on the fly from the Event Builders, or read directly from the Storage System. The DAQ will have its own monitoring library, useful for checking the main working parameters and performance of the detectors. In addition, a proper design of the off-line software can offer a powerful tool to run the reconstruction algorithms and a detector display on a sub-sample of events taken from the live data stream.

The on-line cluster, including the VME processors, will use the Linux operating system. Since no readout operations are foreseen during the spill, it is unlikely that the Linux real-time extension will be needed on the VME processors; this matter will be subject to tests.

### 8.8.4 Cost

The following budget table (Table 8.5) is compiled under a few assumptions:

- MICE will have to buy the VME crates
- The cost of storage is evaluated at today's prices, which will most likely drop in the next year
- The VME processors can be recovered from the HARP experiment at CERN, provided tests show that they meet the MICE performance needs

**Table 8.5:** Cost estimate for the data acquisition system

Item	Number	Cost (k€)
VME crates	10	100
VME processors	10	50 <sup>a</sup>
100 Mbit switches	2	5
Backbone Gbit switch	1	10
Event Builders	Up to 4	15
Mirrored disk buffers	5 ×1 TB	40
Workstations + monitors (control, monitoring, on-line analysis)	20	50
<b>TOTAL</b>		<b>270<sup>b</sup></b>

<sup>a</sup>No cost if recovered from the HARP experiment.

<sup>b</sup>Reduces to 220 k€ if VME processors available from HARP.

## 8.9 Conclusions

A complete set of detectors, capable of performing the measurement of emittance even in the harsh background conditions of the experiment, has been identified. The resources and competence exist in the collaboration to design, build and operate them. Given the crucial importance of tracking, two options are presently under study. The set of crucial measurements to be made has been identified, and is planned so as to allow a final decision on this issue in a time frame that does not delay the rest of the experiment.

## 9 Effects of Radiation on Detectors

### 9.1 General understanding and characteristics

Background emissions by RF cavities constitute an important issue for a muon cooling channel, as they may limit the gradients that can be achieved or create excessive heating in the liquid-hydrogen absorbers. This is also an issue for MICE, although it takes a different form. Tracking detectors for measuring single muons near RF cavities will be subject to backgrounds caused by dark currents. This difficulty was recognised early in the muon cooling effort, and an experimental programme, described in Section 9.2, was developed to understand and mitigate the problem.

Initial measurements have shown that the primary mechanism for the RF backgrounds is as follows: Low energy electrons ('dark current') produced by field emission are accelerated across the cavities and generate bremsstrahlung photons whenever they hit material. While the basic processes of Fowler-Nordheim (FN) field emission, Compton scattering and bremsstrahlung have been understood for years and verified in many experiments, the magnitudes of their effects depend very strongly on specific conditions. For example, the FN process depends very strongly on electric field, with an effective threshold, above which the dark currents rise very rapidly. Very recent experimental results have shown that the presence of high magnetic fields parallel to the electric fields enhance considerably the production of dark currents. Surface properties also have considerable importance. The influence of the various phenomena will be understood better as the experimental programme progresses. For practical reasons, this program is currently focused on investigations of 805 MHz cavity prototypes. To take into account the size and frequency of the cavities, it is assumed here that the relevant processes scale primarily with available area and accelerating field. This will also be experimentally tested.

In MICE, the RF cavities will normally operate at a gradient of about 8 MV/m, over a total length of 1.72 m. The electric field will be out of phase for electrons, and thus will produce a broad spectrum of electrons with a maximum energy of about 10 MeV. The energy loss in the liquid hydrogen is sufficient to stop these electrons, while the cusp magnetic fields generated by the opposite-polarity focusing coils will deflect them. Consequently, the dark-current electrons are not expected to hit the detectors directly. However, the electron beams hitting the upstream and downstream absorbers will generate a bremsstrahlung x-ray flux aimed at the spectrometers. The trackers have been designed to offer only a small amount of low-Z material to this photon beam, and to have fine segmentation and good capability to separate background hits from the signals from muon tracks.

Simulations of the complete magnetic and physical environment are under way with GEANT4, but are not complete at this time. At the order-of-magnitude level, assuming that the detectors can operate with singles rates of 100 MHz/plane, and that each electron stopping in a liquid-hydrogen absorber will produce 0.1 Compton recoil electron (see Figure 9.1), the maximum tolerable electron current would be

$$I = (1.6 \times 10^{-19})(10^8)(10) \approx 0.16 \text{ nA} \quad (9.1)$$

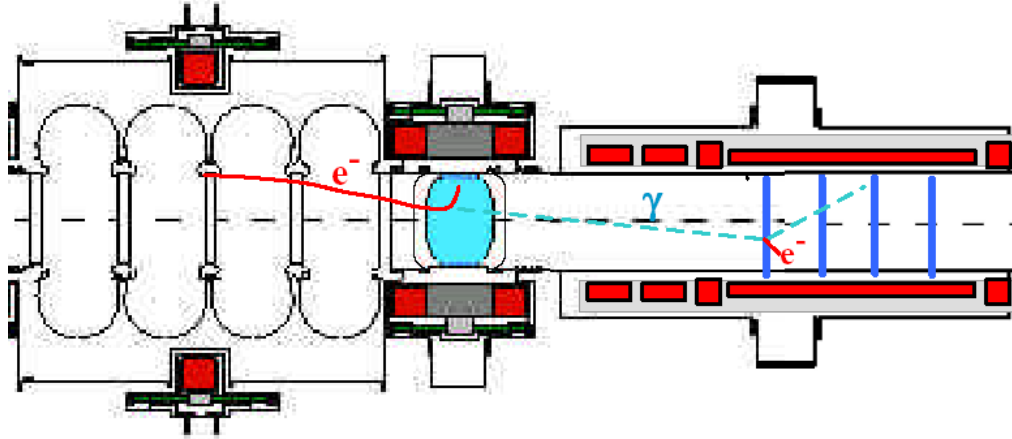


**Figure 9.1:** Possible scenario for the generation by dark currents of backgrounds in the MICE trackers: i) electrons are extracted from the cavity surface; ii) they are accelerated by the electric field along magnetic field lines, iii) electrons are absorbed in the liquid hydrogen absorbers but emit bremsstrahlung photons; iv) the photons interact by e.g. Compton scattering in the detectors.

The operating gradient of the cavities is limited effectively by the available RF power, which can provide only 1 MW/cavity (see Section 5). This limits the accelerating field, which depends on the power per cavity as  $E_{\text{acc[MV/m]}} = 8 \sqrt{P_{\text{[MW]}}}$ , to  $\sim 8$  MV/m in normal MICE operation. Although there is some enhancement of the surface field with respect to the accelerating field, this level is effectively below threshold for measurable dark currents, in the absence of magnetic fields. However, experiments with RF cavities operating in solenoidal magnetic fields have shown much higher emission levels. Furthermore, it will be an important part of the experimental programme of MICE to explore higher accelerating fields. This will be feasible by applying the available power to a subset of the cavities, up to the maximum attainable power of 4 MW/cavity, giving twice the nominal electric field, and a much higher background yield. Higher gradients can also be made available by cavity operation at liquid-nitrogen temperature. As will be seen below, the MICE trackers should be able to operate comfortably under the nominal conditions. The possibility of exploring more challenging operating conditions would require a safety margin of 2-3 orders of magnitude.

## 9.2 Measurement results

As noted, the experimental programme has used 805 MHz cavities, of comparably lower stored energy and higher gradient than those of the MICE 201 MHz cavities. The experimental programme started in 1999, with initial experiments on the Argonne/Taiwan electron gun of the AWA, where it was verified that significant fluxes of x-ray photons were produced from dark current electrons [Nor01]. More recently the experimental effort has moved to Lab G of Fermilab, where data have been accumulated on a 1-m-long 805 MHz open-cell cavity and an 8.6-cm-long pillbox cavity. Both of these cavities operate within the bore of a two-coil superconducting magnet, which can produce 5 T in either a solenoidal mode (with its coils powered in the same polarity) or a gradient mode (with the coils powered in opposition to produce a cusp field). The test set-up is shown in Figure 9.2.

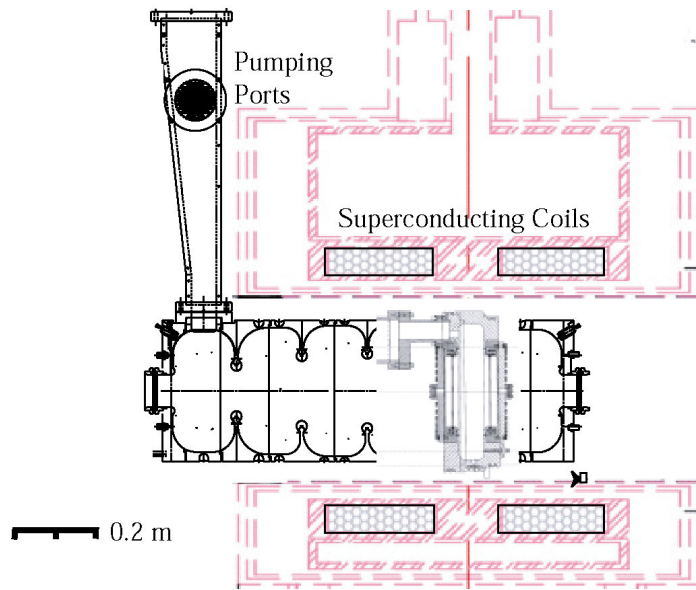


**Figure 9.2:** The 805 MHz pillbox and open-cell cavities in the superconducting magnet of Lab G. The figure shows a superposition of two independent set-ups, which were used in sequence.

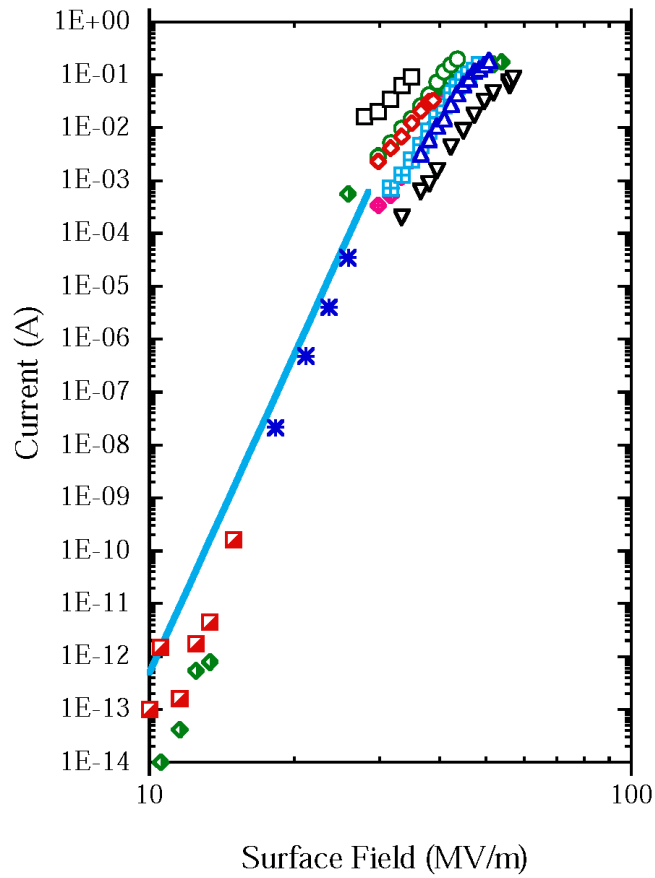


**Figure 9.3:** Dark current vs surface field for the 805 MHz open-cell cavity.

The open cell cavity was used from June to December of 2001, and the pillbox cavity was installed in January of 2002. The open cell cavity permits study of electrons and photons of energy quite close to those of MICE, while the pillbox cavity provides a better match to the magnetic and physical geometry of the MICE cavities.

Initial results obtained with the 805 MHz open-cell cavity are shown in Figure 9.3, where the measured dark current is plotted against surface field [Nor02]. From this figure, it can be seen that, at this frequency, the constraint of  $\approx 0.16$  nA of dark current would be easily met at any field level attainable with the available power supplies. The field emission signal is identified by the rapidly rising  $I(E)$  dependence, with the dark current rising by 14 orders of magnitude. At low surface field, multipactoring, a resonant multiplication of electrons hitting the walls of the cavity, is seen.

These data are readily understood as an example of the simple FN emission from a collection of sharp emitters inside the cavity. The dark current depends on the accelerating field,  $E$ , as

$$I(E) = A_{RF} A_e i_{FN}(E), \quad (9.2)$$

with the Fowler-Nordheim current density of the form,

$$i_{FN}(E) = A_{FN} (\beta E)^2 \phi^{-1} \exp(-B_{FN} \phi^{3/2} / \beta E), \quad (9.3)$$

where  $A_{FN}$  and  $B_{FN}$  are constants of the field emission process,  $\phi$  is the work function of the metal (about 4.5 eV for most metals),  $A_{RF}$  is the duty cycle of the RF cavity for dark currents, effectively equal to 0.1 for all data, and the constants  $A_e$  and  $\beta$  denote the total area of the emitter surface and the total electric field enhancement at the tip of the field emitter. One has essentially no control over the values of  $A_e$  and  $\beta$  in a working cavity as they are the result of surface topology resulting from breakdown events, which in turn seem to depend on a variety of variables including stored energy. In Figure 9.3, the constants  $A_e$  and  $\beta$  effectively determine the vertical and horizontal position of the data set, since  $A_e$  determines the magnitude of the current, and  $\beta$  determines the electric field at which this current exists.

The pillbox cavity has been operating since February 2002. In the absence of a magnetic field, this cavity quickly conditioned to very high surface fields (32 MV/m), showed little tendency to break down, and produced low levels of dark currents and x-rays. Recently, the cavity has been operated with magnetic field, and it was found that the dark currents are higher and that the cavity breaks down at lower gradients with the field than without. This behaviour is shown in Figure 9.4.

Recent data with the pillbox cavity show higher dark current levels at low surface field with the solenoidal magnetic field, in a geometry where the electric and magnetic fields are parallel and normal to the end planes of the cavity. The increase in rate at low gradient seems to be due in part to a displacement of the fast-rising field emission signal, probably due to a change in  $\beta$ , the degree of field enhancement at the field emitter tips, and partially due to an increase in the low field emission due to processes like multipactoring. The data show some conditioning at low gradients, but less than was obtained with the open cell cavity with and without the magnetic field and less than was obtained with the pillbox cavity without the magnetic field. Although the low-gradient behaviour of the pillbox cavity with the solenoidal field is somewhat similar to multipactoring, the gradient dependence is different both from that of field emission and of multipactoring and is not completely understood.

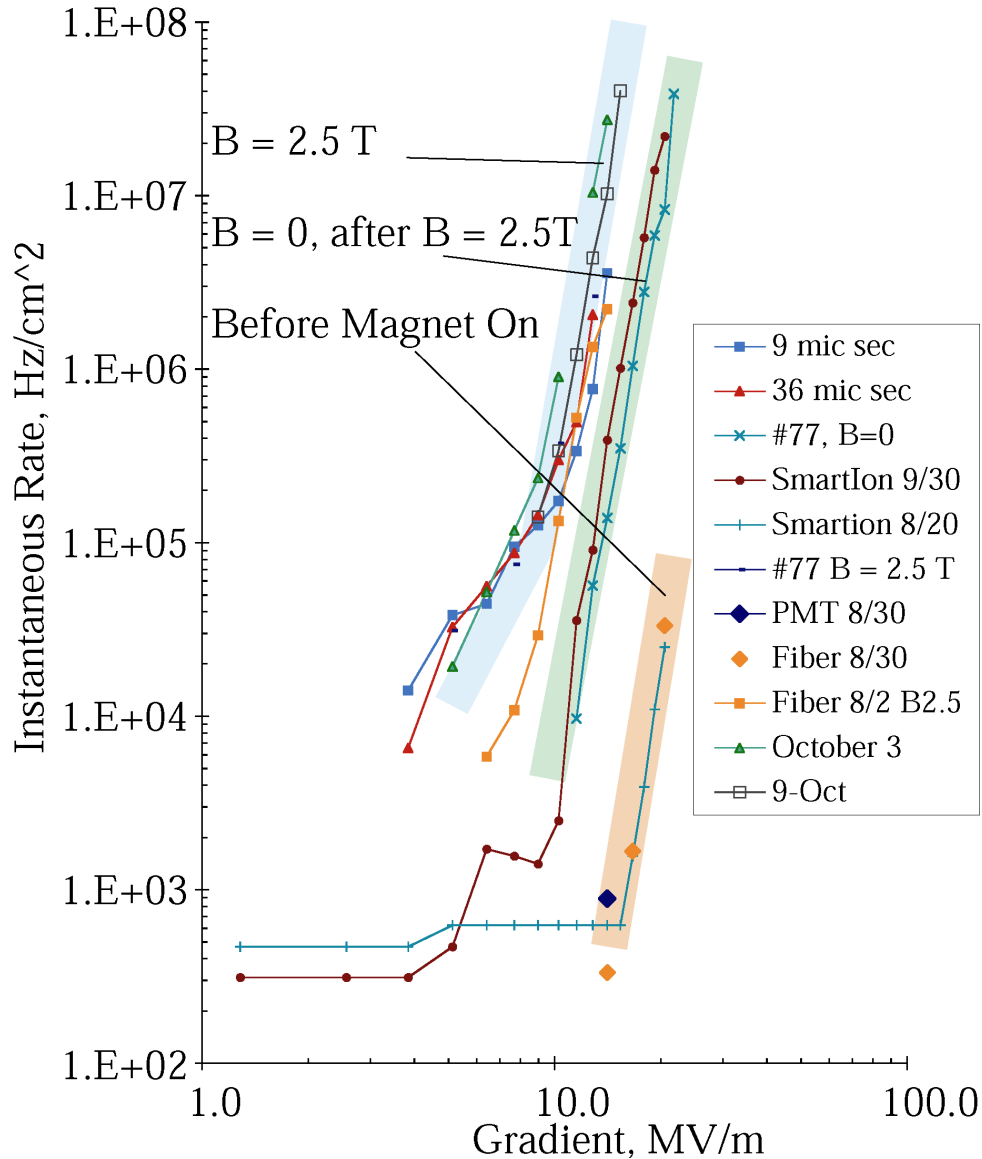


**Figure 9.4:** Dark currents in an 805 MHz pillbox cavity with and without solenoidal magnetic field.

Extrapolation of these data to the MICE situation is attempted as follows. Using data from Figure 9.4 ( $4 \times 10^4$  Hz/cm<sup>2</sup> at 8 MV/m) and a detector radius of 15 cm (an area of 700 cm<sup>2</sup>), scaling the electron rate by the volume ratio of the two cavities (since emitter area should be proportional to surface area, and energy is proportional to length) gives a total electron rate of  $3 \times 10^9$  Hz. These electrons would be comparatively inefficiently converted to photons in the hydrogen absorber (efficiency =  $R_e/X_0 \sim 0.07$ , where  $R_e$  and  $X_0$  are, respectively, the electron range and the radiation length). The resulting photon flux would subsequently produce Compton scattering events in the detector modules. In the scintillating fibre detector, the efficiency for Compton scattering per plane (each consisting of 6 fibre ribbons 0.035 cm thick with a radiation length of 45 cm) is 0.26%. (Here we have taken into account that the fibres are round and spaced within the ribbon by 1.2 diameters.) Thus the rate per plane would be about 0.5 MHz (within a large uncertainty of perhaps an order of magnitude). As described next, the Monte Carlo simulation has studied tracker performance and found no degradation with background rate up to levels much higher than this.

### 9.3 Projected effect on MICE tracker performance

The x-ray background will directly affect the trackers, as no material should stand between them and the cooling section; the other detectors can be shielded with a small thickness of high-Z material if needed. The method for simulating and reconstructing muon events is described in Sections 3 and 8. The tracker response to background was simulated assuming a constant 4 T magnetic field aligned along its axis. The configuration of one tracker is shown in Figure 9.5. Muons and photons were generated according to distributions described below, and the number of photons per muon event was varied in order to estimate the background sensitivity.

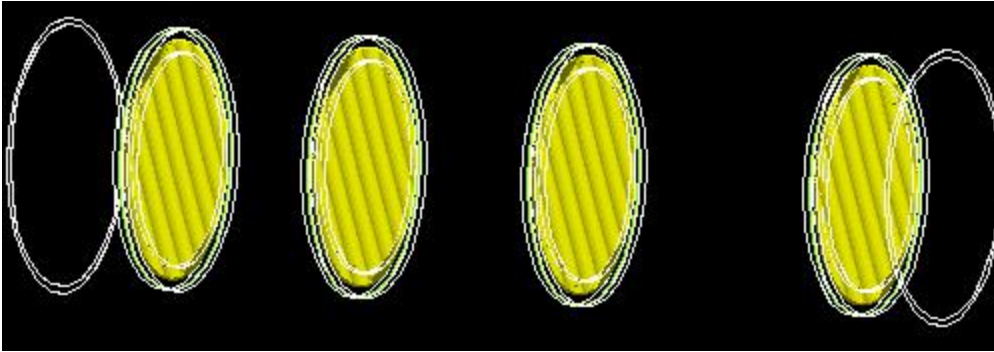


**Figure 9.5:** The fibre tracker geometry as implemented in G4MICE.

Muons were generated with a uniform spatial distribution on a disc 5 cm in diameter on the tracker axis. The muon kinetic energy was uniformly distributed from 166 to 250 MeV and the momentum direction was uniformly distributed over a  $90^\circ$  cone also centred on the tracker axis. Photons were generated with a fixed energy of 50 keV and their direction was parallel or anti-parallel to the tracker axis.

Figure 9.6 shows (on a logarithmic scale) the distribution in reconstructed transverse momenta of muon tracks. Each figure contains two plots, one for the input spectrometer (upper) and the other for the output spectrometer (lower). Because there is no cooling channel in this simulation, these plots should be identical except for effects due to energy loss or multiple scattering in the trackers. The  $x$  axis in each plot is the difference between true and reconstructed transverse momentum, and the  $y$  axis is number of events. There are four samples in each plot, which were generated and reconstructed in an identical way, except for a variation in the number of background photons in each event. The key in each plot shows the number of background particles present in each tracker. These background particles are generated by interactions of the photons in the event with the tracker material. The errors are statistical only.

Figure 9.6 shows no discernable degradation in performance as the background is increased, up to the level that has been simulated to date. This level is two to three orders of magnitude higher than expected from present background estimates. A programme of simulations to verify these conclusions with more realistic assumptions on the background distributions is under way. This will include using a measured energy spectrum and angular distribution for the photon background and simulating dark current production within the RF cavities.

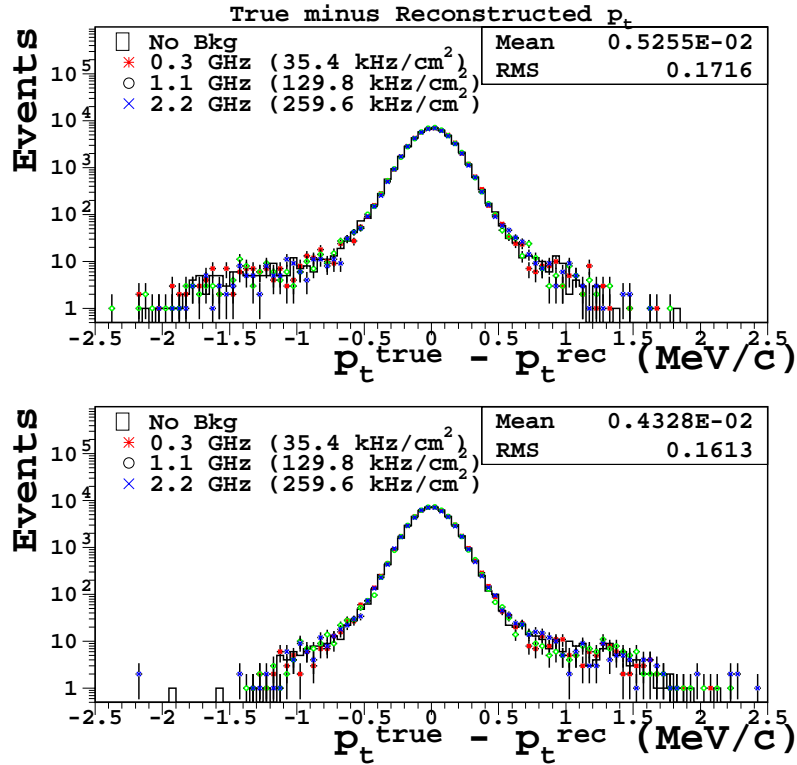


**Figure 9.6:** Transverse momentum reconstruction performance for background rates of 75, 280, and 550 MHz/plane.

## 9.4 Programme of further measurements

An extensive programme at Lab G at Fermilab will include ongoing measurements of the pillbox cavity and other structures. The highest priority is to study the behaviour of beryllium windows. Compared with the open-cell case, the flat window geometry permits an increase in the accelerating field by a factor of about 2.6 for the same surface field. The experimental study of the operation of Be windows in RF cavities is under way at Fermilab. First a thin 3-cm-diameter Be disc has been introduced into an electron gun without any detectable damage. After this, a Be window, coated with TiN to prevent multipacting, has been installed into the 805 MHz test cavity at lab G and conditioning has started.

Another factor that influences the dark current is the magnetic field. Since the magnetic environment of MICE is complex, and the dark currents seem strongly affected by the amplitude and direction of the magnetic field, the dark currents will be measured as a function of the magnetic field gradient. The magnetic field configuration will be varied by powering the two coils of the Lab G magnet with independent power supplies. This will permit establishing non-uniform fields similar to those used in the MICE experiment.

Alternative materials and surface treatments will also be investigated, first theoretically and then experimentally in the MUCOOL Test Area (MTA). The MTA facility will also be used to test a variety of RF coupling and window mounting options in a realistic solenoidal magnetic field. Tests of surface coatings can be done by replacing the windows in the pillbox cavity.

When the Muon Test Area (MTA) becomes available at Fermilab, 201 MHz cavities can be tested at full power (the MTA will have access to a spare 201 MHz power supply located in the Fermilab linac gallery).

# 10 Implementation of MICE at RAL and Engineering Integration

## 10.1 Hall layout

The MICE experiment will be installed in Building R5.2 at RAL, a part of the ISIS accelerator complex located between the ISIS linac hall (Building R5.1) and the ISIS control room (Building R5.5). It was built in the 1960s to house a linac and currently houses a high energy physics beam line facility. Figure 10.1 shows the location of Building R5.2. It has about 560 m<sup>2</sup> of floor space, a floor-to-roof height of 8 m, and a volume of about 4500 m<sup>3</sup>, and it is equipped with two overhead cranes, each with a capacity of 8 tonnes.

The proposed MICE layout in Building R5.2 is shown in Figure 10.2, which indicates the location of the MICE experimental components downstream of the beam line. The experiment will be located inside a concrete shielding bunker. Space within the hall has been allocated for the major services to detectors and RF systems. Positions for the main components of the cryogenics and hydrogen systems are also shown and are discussed in Section 10.2.

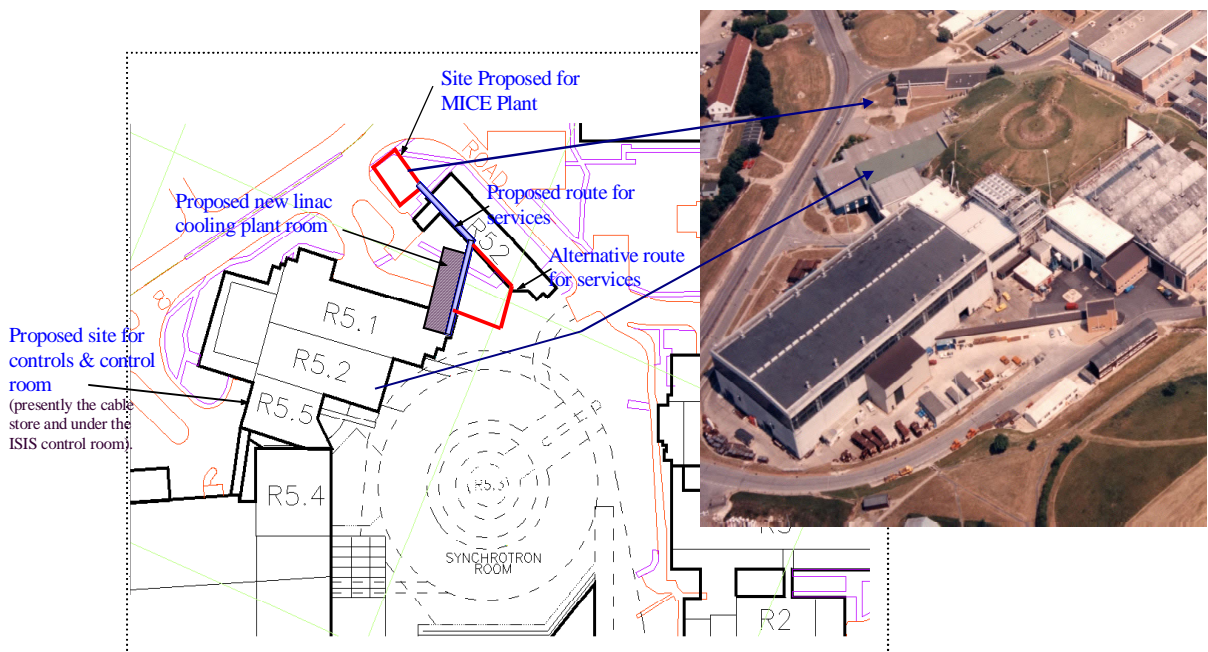


**Figure 10.1:** Location of Building R5.2 at RAL and proposed site for MICE cryogenics plant.



## 10.2 Infrastructure and services

### 10.2.1 MICE services audit

MICE will require the extensive cooling and power services summarized in Table 10.1.

**Table 10.1:** MICE cryogenics, electrical, and cooling water requirements.

	Equiv. cooling power @4K [W]		Liquid	Electrical	Chilling
	basic power	+ 30 % margin	nitrogen [l/hr]	power [kW]	water [kW]
MICE magnets + absorbers	140				
Beam-line SC solenoid	35				
SC magnets + absorbers	175	230	100	125	125
SciFi detectors	150	200	25	110	110
SC magnets + SciFi detectors	325	425		230	230
Extra for absorbers with LHe	53	70			
SC Magnets with LHe absorbers	228	300		160	160
RF system				100	100
All systems	378	500	125	370	370

### 10.2.2 Cryogenics system

As described in Section 4, MICE makes use of superconducting magnets and liquid-hydrogen absorbers, both of which require substantial cooling power. The scintillating fibre detectors also need cooling for their VLPC photosensors. To serve these needs, a dedicated cryogenic system will be installed in the experimental hall. The general structure of the cryogenics system is shown in Figure 10.2 and Figure 4.4. It consists of a refrigerator that supplies He cryogen to both the superconducting coils and the hydrogen absorbers via transfer lines. The refrigerator includes a helium tank and a compressor, both placed outside the building, and a cold box and 500-l buffer dewar, both positioned inside the experimental hall. It should be noted that if the solenoid from PSI is used as the superconducting decay solenoid in the upstream beam line it would need a dedicated cold box as it requires supercritical helium for cooling.

It is envisaged that the helium refrigerator cold box will deliver two-phase helium at 4.4 K in the saturated-liquid condition and 14 K helium gas at a pressure of 14–18 bars. The 4.4 K helium will be used to cool seven superconducting magnets in the MICE magnet string, and the 14 K helium will be used to cool the liquid-hydrogen absorbers, the magnet shields, and the gas-cooled electrical leads that will operate between 50 K and room temperature. Helium returns to the refrigerator from the magnet string at 4.3 K. Helium gas from the absorbers returns to the refrigerator at 18–19 K. The helium that will be used to cool the magnet shields and leads will by-pass the refrigerator cold box and return to the refrigerator compressor at room temperature.

### 10.2.3 Hydrogen system

The MICE experiment employs three absorbers, each filled with about 21 l of liquid hydrogen (i.e., 63 l in total). A dedicated hydrogen handling system will be designed and installed in the hall. The general schematic of the MICE hydrogen system is shown in Figure 10.2. The system includes hydrogen supply bottles placed outside the building, a hydrogen buffer tank

and a hydrogen vent system. The absorbers will be placed inside igloos to minimize the volume into which hydrogen might leak, thus simplifying its collection and venting. Hydrogen safety issues are discussed in Section 10.3.1.

#### 10.2.4 Electrical power and water

The experiment requires both electrical power and chilled water for the RF power systems. There is already sufficient 240 V power capacity installed in the building, but a 3.3 kV system must be added to supply the refrigeration plant and RF power systems. A new chilled water plant of 1 MW capacity will be built for ISIS. Negotiations with the ISIS team are currently taking place, so as to increase this power to 1.5 MW, which would satisfy the needs of both ISIS and MICE. The proposed location for the new ISIS chilled water plant is indicated in Figure 10.1. This figure also shows a possible position for the MICE cryogenics plant, which includes the compressor room, the He buffer tank, and the hydrogen supply bottles.

### 10.3 Safety

Safety is a key issue for MICE. A MICE Hazard Assessment will be prepared to identify possible accident scenarios, analyse their probabilities and consequences, and identify steps needed to reduce the risks to a level as low as reasonably achievable. An independent safety committee will review the Hazard Assessment.

The design of both the MICE experimental apparatus and its infrastructure will be done in accordance with the following regulations:

- The new European explosive gas regulations [ATEX Web-site]
- Pressure vessel regulations: RALSC1 [RALSC1], HSN8 [RALHSN8] and PED 97/23/EC [PED97]
- RAL codes of practise and safety policy, including Health and Safety Executive and Control of Substances Hazardous to Health (HSE and COSH) regulations

Hazards specific to the engineering of the MICE experiment are briefly discussed below.

There will be several vacuum vessels in MICE. At RAL, a vacuum vessel is considered to be a pressure vessel and must be certified to the British standard BS5500 by an accredited professional engineer. The certification must state that the vessel meets the requirements of BS5500, RALSC1 where applicable, HSN8, and PED 97/23/EC, and is of a 'sound engineering design'. The vessel design, where required, must include adequate safety provision for loss-of-vacuum events caused, for instance, by a cryogen leak or by the breaking of a vacuum window. Documents detailing the design calculations for the vessel must be submitted for scrutiny along with the certificate.

Metallic pipe work other than vacuum-insulated cryogenic transfer lines will be designed to meet, at a minimum, the requirements of BS807 and PED 97/23/EC.

### 10.3.1 Hydrogen safety

Liquid hydrogen is currently used in the moderators on ISIS, albeit with volumes somewhat lower than those specified for MICE.<sup>4</sup> Design of the MICE hydrogen system will be done in accordance with RALSC1 (currently under revision) and RALSC6 [RALSC6].

RALSC1 lists the following potential hazards when working with liquid hydrogen:

- Drop of oxygen content in air below 17% (oxygen deficiency hazard)
- Low temperatures
- Large liquid-to-gas expansion ratio
- The wide range of flammable limits after vaporization, with threat of explosion

The most significant hazard from a hydrogen system is an explosion (the flammability range of hydrogen in air is 4–75% and the detonation range is 18–59%). Great care in the management of faults must be taken to ensure that a chain of events does not lead to an uncontrolled dangerous situation. In particular, an assessment will be required on the consequences to ISIS of an explosion.

A particularly hazardous and undetectable situation, potentially leading to an explosion, can be generated if oxygen (air) entering from small leaks in a vacuum chamber is cryogenically pumped by cold surfaces near the liquid-hydrogen containers. The MICE liquid-hydrogen absorber design will conform to the RAL safety rules (as expressed in RALSC1), which require steps to prevent the condensation of oxygen on any surface that could come into contact with a hydrogen leak. As an example, the ISIS liquid-hydrogen moderator, shown schematically in Figure 10.3, is surrounded by a vacuum layer that is surrounded, in turn, by a helium layer to prevent the ingress of air in the event of a leak.

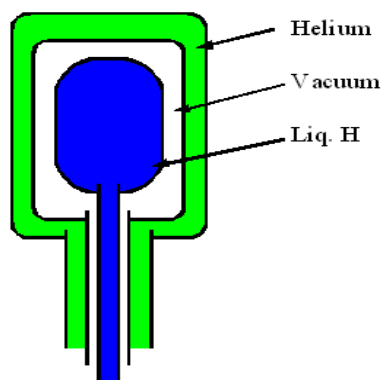


**Figure 10.3:** Schematic diagram of the liquid-hydrogen moderator currently in use on ISIS at RAL.

---

<sup>4</sup>ISIS uses about 20 l of liquid hydrogen, whereas MICE will use about 63 l.

All sources of ignition must also be excluded from the hydrogen system. In particular, the RF system is such an ignition source. In MICE, the hydrogen vessel is separated from the RF module by two aluminium windows (along with a third, beryllium, window in the baseline design for the RF cavity terminations). In addition, igloos purged with nitrogen gas will be used around the hydrogen system. Inside the igloos, and in other defined zones as needed, all electrical equipment will have to be ‘intrinsically safe’ and be obtained from certified suppliers.

Venting of hydrogen will take place through the roof. A chimney may be required to exhaust the hydrogen away from air conditioning intakes.

For MICE, several options have already been considered for the design of the safety measures surrounding the LH<sub>2</sub> absorber modules. The final choice for the LH<sub>2</sub> module design will be made on the basis of a detailed safety analysis that will be carried out under the supervision of the RAL/ISIS safety officers. In general, the experiment benefits from having the least additional material in the beam path, so the preference is for a safe approach with the fewest windows. Design concepts presently under consideration, and their particular safety features, are described below:

- Option 1 (Figure 10.4) is the closest in concept to the design of the ISIS hydrogen moderator, which is already approved by the RAL/ISIS safety officers. Here, the hydrogen absorber volume is surrounded by a vacuum space for thermal isolation and a secondary jacket filled with helium (or other inert gas) to prevent oxygen from an air leak from being cryo-pumped onto the cold surface. For MICE, several design questions remain to be answered, in particular the behaviour of the warm intermediate window in the event of shock-cooling by a hydrogen leak. A detailed analysis will be done to study this and other aspects of the design.
- In option 2 (Figure 10.5), the idea is to separate the focusing coil cryostat vacuum and the LH<sub>2</sub> absorber vacuum (thus providing an extra jacket for LH<sub>2</sub>), and to keep the LH<sub>2</sub> safety window relatively cold (thus eliminating the potential problem associated with the warm window in option 1), but without increasing number of windows.
- In option 3 (Figure 10.6), the MICE components are separated from air by an argon gas jacket. In this scheme there is no path for air to leak into the LH<sub>2</sub> vacuum volume. This option is the most attractive for the experiment because fewer windows are required. A first practical implementation of this scheme has been developed, as described in Section 10.4.2, and serves as the baseline approach. The detailed design of this concept must provide a jacket for all the penetrations of the cryostats, a non-trivial exercise.

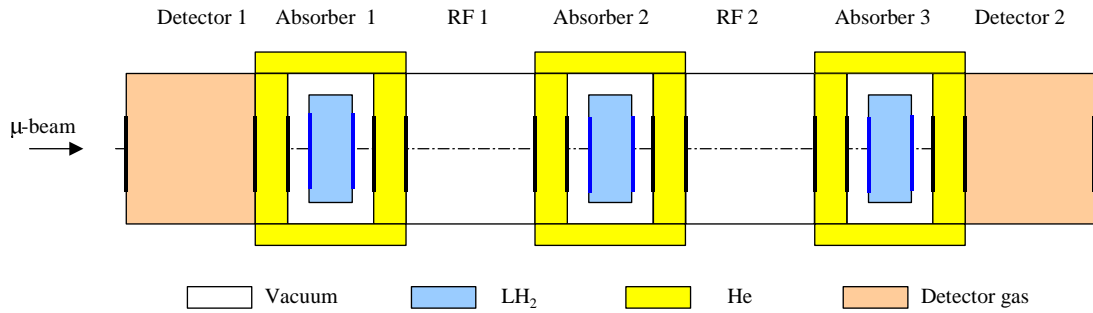


**Figure 10.4:** Schematic diagram of safety option 1.

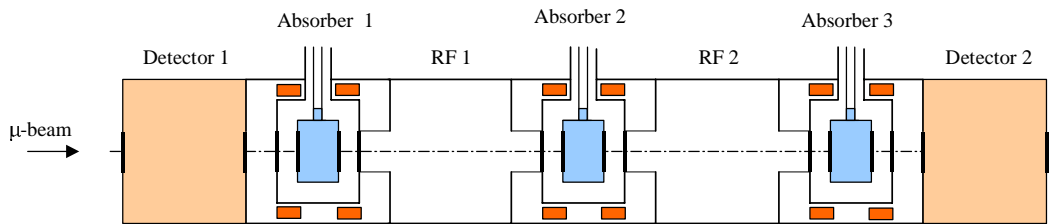


**Figure 10.5:** Schematic diagram of safety option 2.

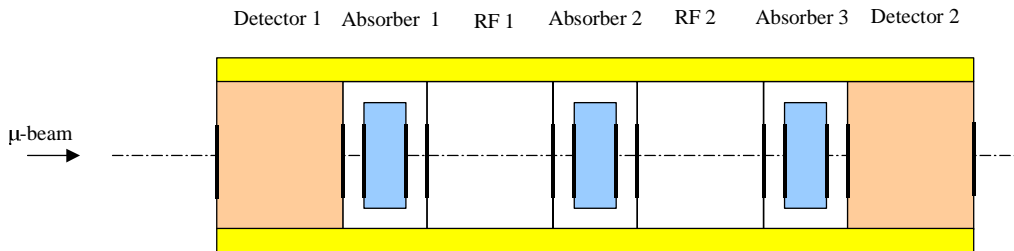


**Figure 10.6:** Schematic diagram of safety option 3.

### 10.3.2 Radiation safety

The principal sources of radiation in the MICE experiment come from the proton beam in the ISIS synchrotron and x-rays generated by the RF cavities. Shielding will be used to reduce levels to  $0.5 \mu\text{Sv/hr}$  in normally accessed areas, as required by HSN20 [RALHSN20]. To achieve this, the cooling section in the experimental hall will be surrounded by radiation shielding made of roughly 60-cm-thick concrete (and steel) blocks, as shown in Figure 10.2. The final thickness of the concrete shielding will be chosen based on the experience of running a prototype of the RF cavity at Fermilab.

### 10.3.3 Magnetic field safety

The baseline MICE magnetic channel does not include either active or passive magnetic shielding in the vicinity of the experiment and generates a significant magnetic field in the experimental hall. This design feature cannot be modified very easily since the focusing properties of the coils in the cooling section originate from the fringe fields themselves. Therefore, it has to be checked that the field within the MICE experimental hall, as well as the stray field in the nearby buildings, in particular the ISIS linac and control room, are below the required safe levels.

According to HSN9 [RALHSN9] and NRPB, stray magnetic fields in a normally accessed public area must not exceed 0.5 mT, the limit for a person utilizing a pacemaker. Where work must be carried out in a magnetic field, the following limits are used:

- partial body exposure (arms, hands, and feet): 2 T for short periods (minutes); 0.2 T for long periods (hours)
- whole body exposure: 0.2 T for short periods; 0.02 T for long periods.

Two regions of stray field have been considered: i) the  $B = 0.5$  mT (5 gauss) line, which forms the boundary of the stay clear region for the general public and for persons with pacemakers, and ii) the 0.01 T (100 gauss) line, within which precautions must be taken if one needs to work with ferromagnetic objects. Work will normally be conducted around the MICE apparatus with the magnets off, but any magnet-on work around the MICE channel will have to be done using non-ferromagnetic tools and following safety procedures; furthermore, the area around the magnet will need to be swept for ferromagnetic objects before the MICE magnetic channel can be turned on.

The baseline case (case 1a in Section 4.1 and the similar cases studied in that section) has the feature of generating zero net magnetic moment, so that at distances comparable to the distance separating the cancelling elements the stray field falls to zero rapidly. The level of stray field produced by MICE was modelled with the OPERA-3D software package. Some results are shown in Figure 10.7.

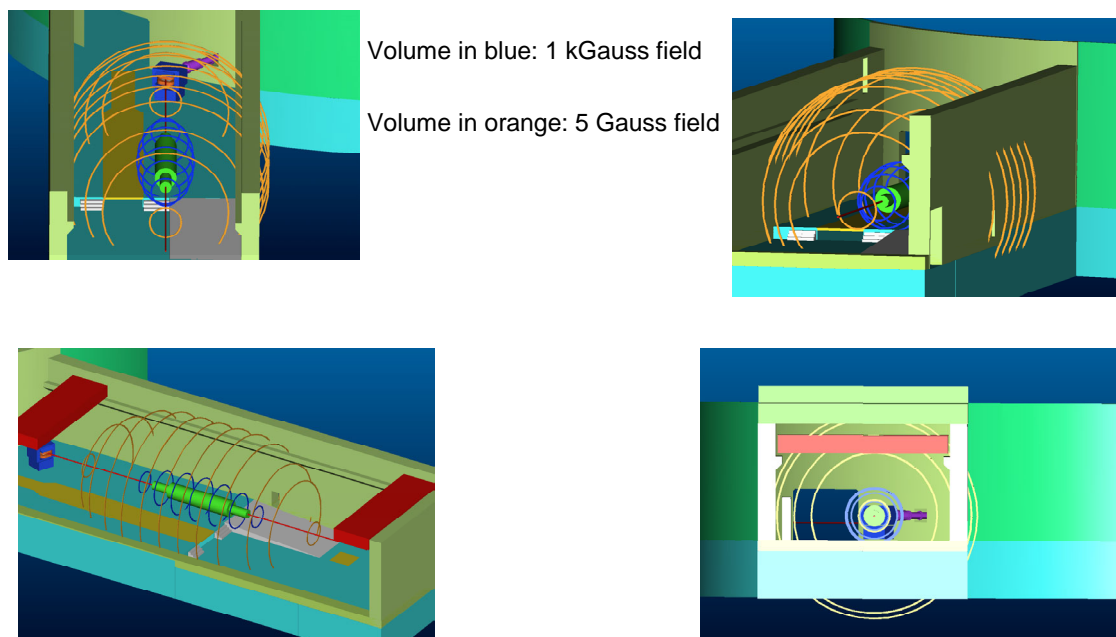


**Figure 10.7:** Calculated stray fields around MICE in the experimental hall.

In the worst of the cases presented in section 4 (case 1b), the largest extension of the 0.01 T line is situated at a distance from the MICE axis of  $r = 4.35$  m and a position with respect to the center of the cooling section of  $z = 7.54$  m. The 0.5 mT line for this case extends to  $r = 7.5$  m and at  $z = 12.7$  m from the centre of the experiment (about 6.9 m from the end of the spectrometer magnet).

These results show that the 0.01 T contour line is well contained within the MICE experimental hall, while the 0.5 mT line is mostly contained as well. The effect of MICE on the ISIS linac, which is in the adjacent building, will be negligible. The effect of the experiment on the ISIS control room remains to be clarified, as the 0.5 mT field contour extends slightly into it. Magnetic shielding using metal plate cladding could be utilized to shield dedicated areas or apparatus, to protect them from stray fields further if this were deemed necessary.

These positive results apply to the baseline case with three magnetic field flips in the cooling section. The coupling coils generate most of the stray field. For situations with fewer or no magnetic field flips, the stray field may be larger, and more serious precautions may have to be taken. A more complete, case by case, study will be needed to understand which ones can be used without additional shielding and which ones would require further precautions.

## 10.4 Engineering and installation plans

The engineering of MICE must satisfy the requirements imposed by i) the strong magnetic forces, ii) the installation in steps, and iii) the safety requirements. This section develops a scenario that takes these constraints into account, with emphasis on safety, while complying with the programme of measurements to be undertaken.

### 10.4.1 Installation

The MICE experiment will be installed in stages, starting from a spectrometer solenoid equipped with tracking detectors and ending with a complete cooling section between the two spectrometers. This staged build-up is described in Section 3.5.3. The proposed staged approach requires a flexible design of the cooling section elements, their support structures, and the service lines. The support system will be implemented using rails, to allow repositioning of the MICE components along the beam line. A technical specification for the support structure – a key element in the overall integration of MICE – is being prepared.

A preliminary analysis of the MICE magnetic system has been carried out using the OPERA-3D software package. The results predict axial forces on individual magnetic coils of up to 200 tonnes, with net forces on the cryostat structure up to 30 tonnes (see Figure 10.8). These net forces must be supported between the magnet cryostats.

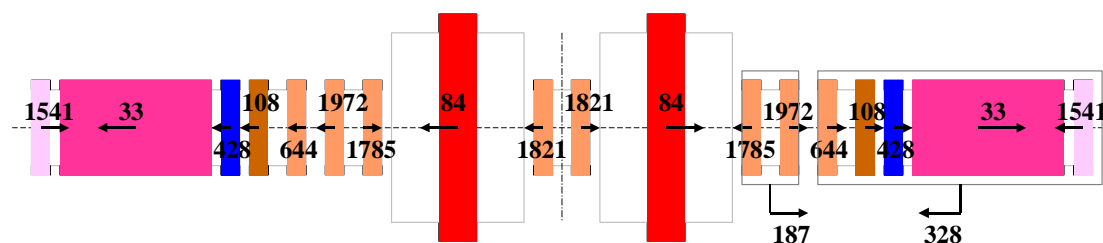


**Figure 10.8:** Axial forces (in kN) on the coils in the MICE magnetic system.

### 10.4.2 Cooling section components

The MICE cooling section lattice (see Figure 10.9) consists of five modules — three hydrogen absorber plus focusing magnet modules and two RF cavity plus coupling magnet modules. To facilitate the installation at RAL, it is envisaged that the required sub-assemblies,

which are provided by a number of widely separated institutions, will be assembled and tested as modules. After the tested modules are delivered to RAL, they will be installed in the experimental area, aligned to the beam axis, and joined together by special retractable flanges that permit transverse displacement of individual modules without affecting adjacent components of the lattice.

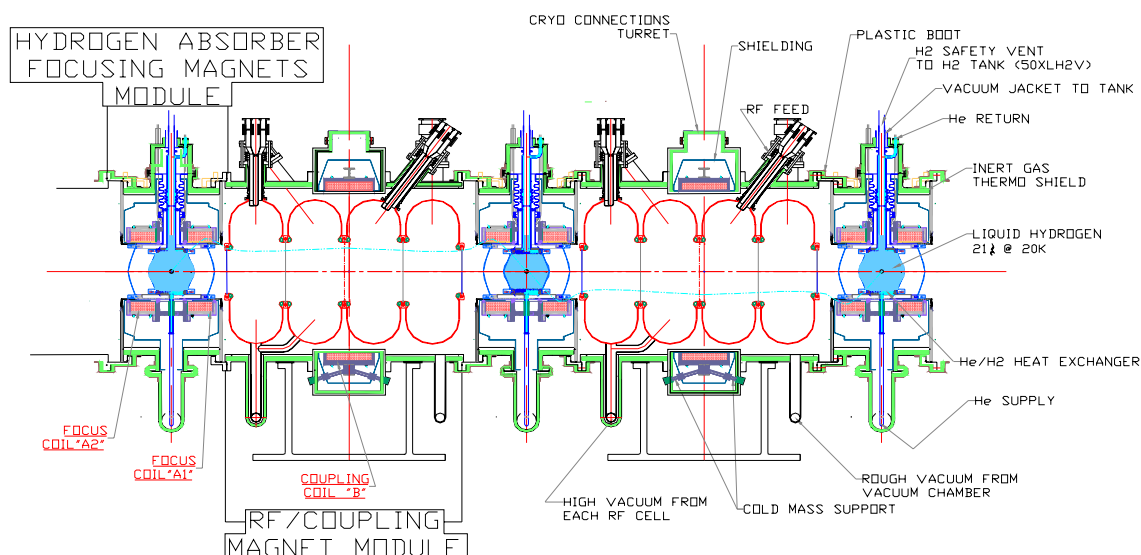


**Figure 10.9:** MICE cooling section component arrangement.

The spectrometer solenoids located at both ends of the cooling apparatus are not shown.

Because of the need for liquid-hydrogen absorbers, there are special requirements for the vacuum housing for each module. In particular, it is necessary to ensure the absence of oxygen in the system. In addition, established safety design criteria implicitly require that the safety aspects of each module be fully tested independently as well as in their final form as an assembled unit. To accomplish this, each module is a separate assembly consisting of a doubled-walled vacuum chamber filled with inert gas (argon) in the annular space between the walls.

The cooling cell modules and their assembly are now described.

### 10.4.3 Absorber and focusing magnet module

The main components in this module are the liquid-hydrogen absorber and the two focusing magnet coils. Each system requires its own environment for proper performance and for safety, so each has its own vacuum enclosure. Other sub-components in this module include the structural supports, which are designed for low heat leak and to support the mechanical forces under either normal or off-normal conditions.

#### 10.4.3.1 Hydrogen absorber

The liquid-hydrogen absorber design takes into account the safety rules specified in RALSC1, particularly with regard to the precautions to avoid oxygen condensation on the absorber vessel body, windows, connecting cold helium and hydrogen tubing, etc. As shown in Figure 10.10, this is accomplished by isolation using both vacuum and an inert-gas-filled annular volume enclosing the vacuum chamber.

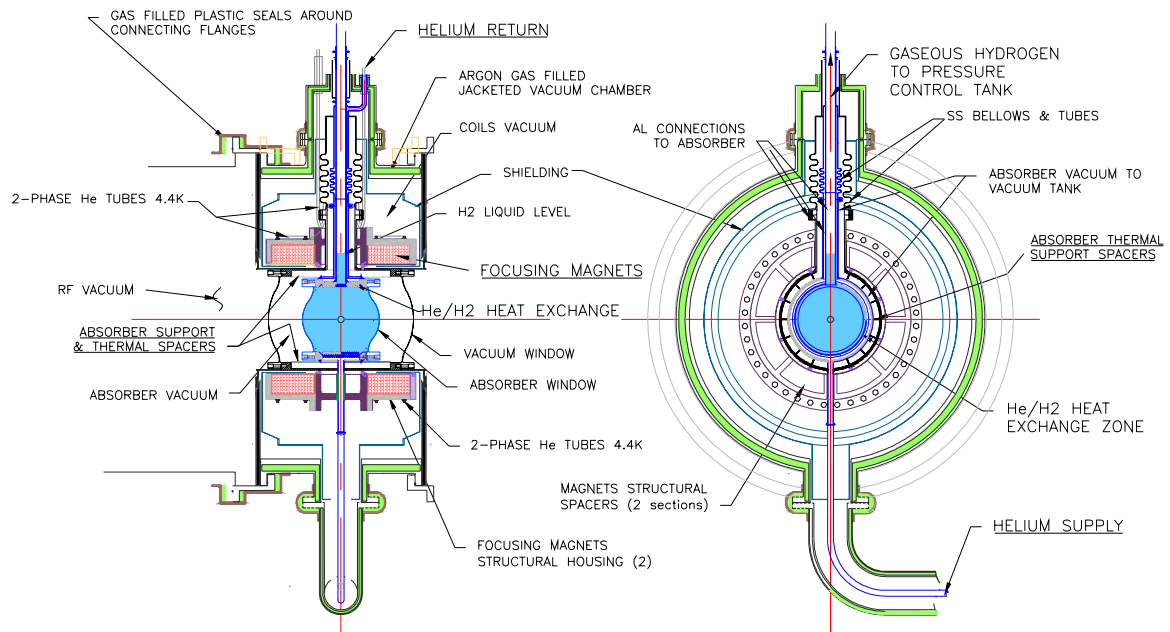


**Figure 10.10:** Cross-sectional views of the liquid-hydrogen absorber and the focusing magnet module.

Figure 10.10 illustrates the absorber design concept. Liquid hydrogen is contained within the cylindrical absorber body and its two windows. The windows are bolted onto the absorber body, thus allowing their replacement by a mechanical support for other types of absorbers. The liquid hydrogen is maintained at a temperature of about 20 K by heat exchange at the inner perimeter of the all-aluminium absorber body. The inner perimeter has an extended surface area in the form of fins. Behind the finned surface is a channel, also integral to the absorber body, where helium coolant flows at a controlled temperature of about 17 K. Two concentric tubes are welded to the top of the absorber, the inside tube to the inner perimeter for conduction of hydrogen to a large evacuated vessel, and the outside tube to the outer perimeter for the return of helium to the refrigeration system. Helium from the facility refrigeration system is conducted through the bottom of the absorber, past the heat exchanger channel and out to the top, through the annular space, to the return port. As the hydrogen liquefies by condensation, it will fill the absorber chamber volume and reach some level up into the hydrogen tube. The level in the tube will vary depending on the (small) heat input from the beam and from any heat leakage into the system. This variable level provides an ideal location for instrumentation sensors to monitor absorber behaviour. The evacuated vessel for safety relief of the hydrogen is required to have a volume 800 times that of the liquid volume from one absorber (calculated to be 21 l), i.e., 16,800 l.

#### 10.4.3.2 Absorber vacuum chamber assembly

The functions of this chamber (see Figure 10.11) are:

- To provide isolation vacuum to shield the absorber from excessive heat, air, and any propelled objects that could impact the delicate absorber windows
- To contain the liquid hydrogen and facilitate safe boil-off and evacuation of any evaporated hydrogen, preventing over-pressurization
- To provide structural support to the absorber in case of a catastrophic event in which an absorber window breaks

The chamber comprises a flanged cylindrical container vessel, with aluminium windows similar to the ones in the absorber, that completely encapsulates the liquid-hydrogen absorber. The chamber is constructed from four pieces: two end flanges on which to mount the windows and two half-cylinders to form the body. Thin blades of 16-gauge aluminium, wedged radially between the absorber and the vacuum chamber in the radial direction, support the absorber.

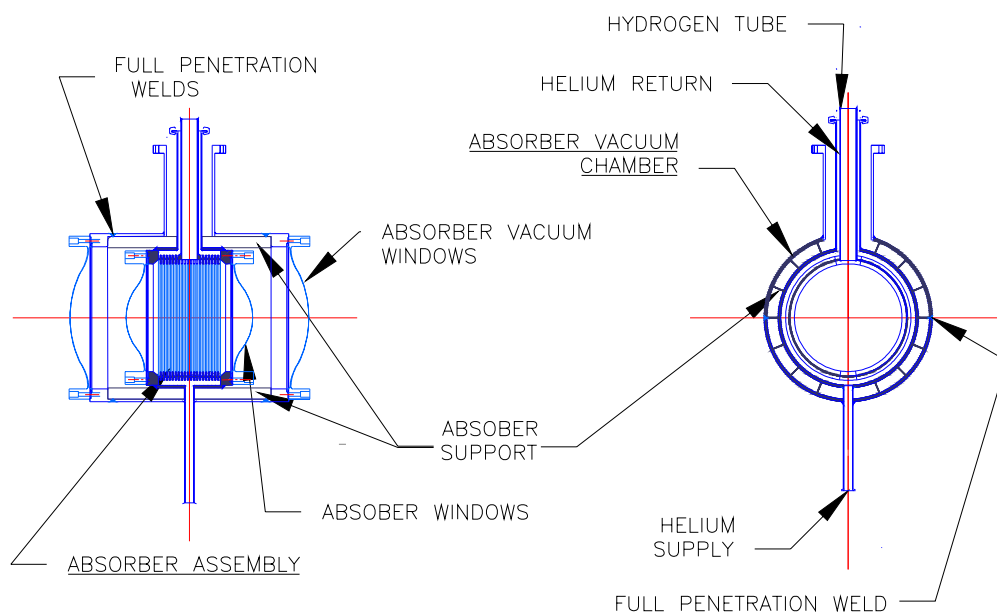


**Figure 10.11:** Cross-sectional view of absorber vacuum chamber and connections.

The assembly sequence of the absorber and vacuum chamber commences with the welding of the hydrogen and helium tubes to the absorber body to form the first sub-assembly. The two halves of the vacuum chamber cylinder are then positioned around the absorber to be welded. Prior to welding, the supporting blades are seated within machined grooves on the outside of the absorber assembly and the inside of the cylinder. The top half-cylinder has the exhaust vacuum nozzle welded to the inside of the cylinder. This half is slipped around the hydrogen and helium tubes. After the welding of the vacuum chamber cylinders, the final step is to weld the flanges to the two ends of the vacuum chamber cylinder body. At this stage several tests will be performed on the absorber vacuum chamber assembly to verify its integrity.

All components in this assembly are aluminium; connections are stainless steel with bellows to accommodate thermal displacements and to allow for sealing with bayonet-type insertions.

#### 10.4.3.3 Absorber and focusing magnet assembly

As shown in Figure 10.12, the magnet support structure consists of a welded or cast aluminium flanged cylinder split in half. At the top and bottom of each half-cylinder a semicircular enclosure fits snugly around the absorber tube connections, which are separated from the cylinder wall by G-10 bushings. The two half-cylinders are bolted to each other and to the magnet casing. At the inside of the flange, adjustable threaded spacers are used to aid in centring the absorber between the magnet coils.

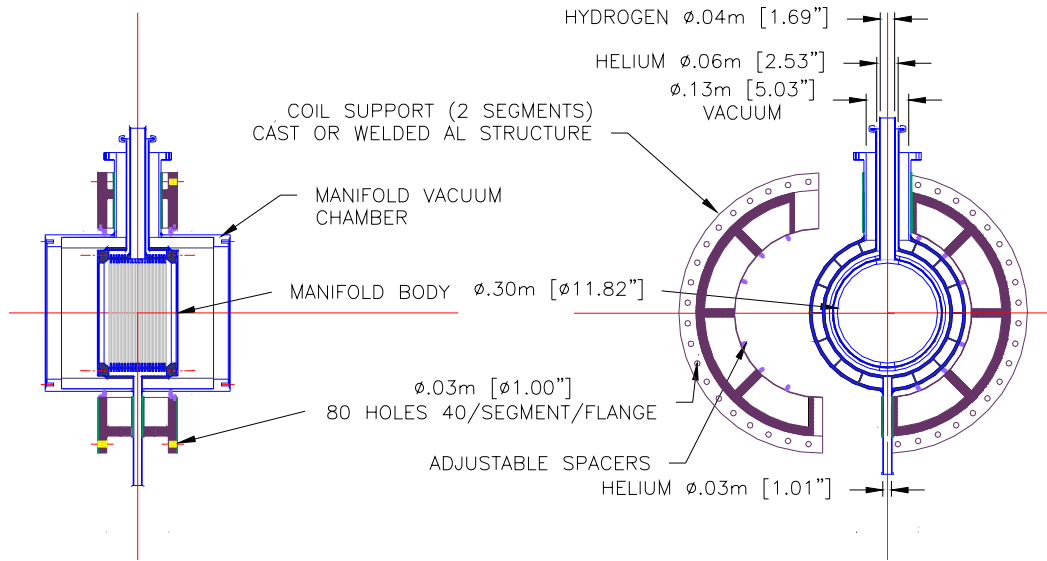


**Figure 10.12:** Focusing magnet support assembly detail.

The assembly shown in Figure 10.12 is inserted into the absorber vacuum chamber. Cold-mass supports are affixed to the reinforcing gussets of the coil support structure (see Figure 10.13). These supports are designed for vertical and longitudinal restraint of forces produced by gravity and magnetic fields from the coils. All the supports will be connected at this time, followed by the insertion of the magnet assemblies, which will be guided into place and pinned for alignment. The mass of each coil assembly is about 100 kg; the maximum force considered in the design of the longitudinal supports is that encountered during a magnet fault (refer to Figure 10.8). These forces can be carried by four fibreglass-epoxy cylindrical supports, attached to the coil support structure and the inner wall of the vacuum chamber longitudinally in the beam direction.

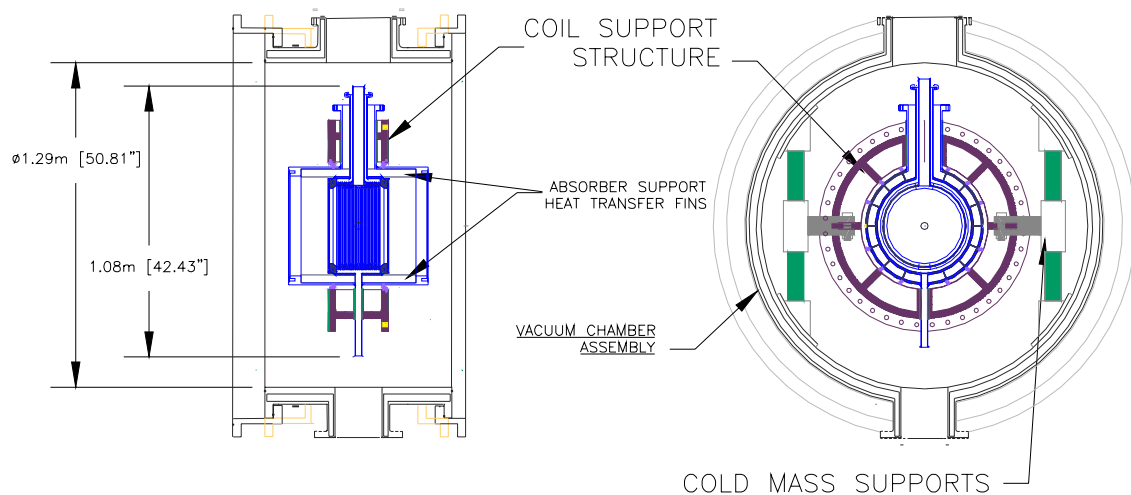


**Figure 10.13:** Focusing magnet coil support assembly.

#### 10.4.3.4 Magnet coil assembly

Focusing magnet coils (see Figure 10.14) will each be encapsulated in a cylindrical flanged structure of welded or cast aluminium construction. On the outside surface of each cylinder, tubing is attached for carrying 4.4 K two-phase helium that cools the superconducting coils to their operational temperature. (These magnet coils, if properly protected, can be shipped to the assembly site individually.) The next step in the assembly is the installation of the 40 K thermal shielding around the magnets. The shield will be fabricated from 1100 aluminium alloy, 1 mm thick; details of the shield construction are not yet finalized.

To isolate the vacuum for the magnets, the hydrogen absorber vacuum chamber is assembled at both ends with tubular extensions at its perimeter that extend to the outer boundary of the module length. The edges of these tubes will be seal-welded to an insert in the module vacuum chamber end plates. The module will be tested after complete assembly and prepared for shipment to RAL. This preparation will include purging all module components of any hydrogen or helium using dry nitrogen. Temporary blind flange plates will be installed at both ends of the module and on all nozzles, hermetically sealing the module inner volume from the environment. Volumes inside the module, and the annular volume between the vacuum vessel double walls, will be purged and filled to above atmospheric pressure with dry nitrogen and argon gas, respectively, in preparation for shipment.

#### 10.4.4 RF cavity and coupling coil module

This module (see Figure 10.15) comprises one RF assembly of four cavities, one coupling coil, and the module vacuum vessel, of similar construction to that of the absorber and focusing magnet chamber. The coupling coil magnet is totally enclosed in an independent vacuum chamber of argon-gas-filled, double-wall construction. A turret on top provides access for electrical and cryogenic connections.

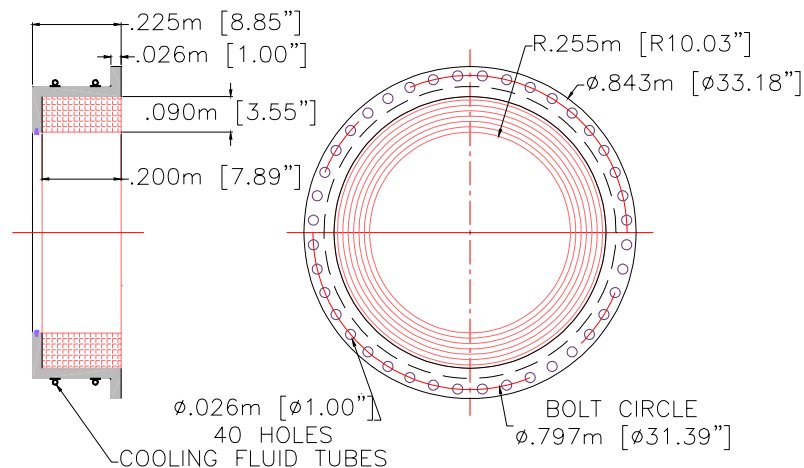


**Figure 10.14:** Focusing magnet assembly detail.

The module vacuum vessel will be constructed in two sections that bolt to the coil vessel. Flanged nozzles penetrate the vessel. Two of these are angled to permit connection to the central RF cavities while still clearing the magnet vacuum vessel. Special coaxial connections are mounted through the nozzles and attached to each cavity. All connections are sealed with

bellows to accommodate movement expected from temperature variations and/or initial tuning of each cavity.

Each RF cavity is maintained at high vacuum via connections through nozzles that penetrate the module vacuum chamber. Internal manifolds permit two cavities to be pumped through one nozzle, requiring only two cavity–vacuum penetrations. A third nozzle is used to provide vacuum for the entire module.

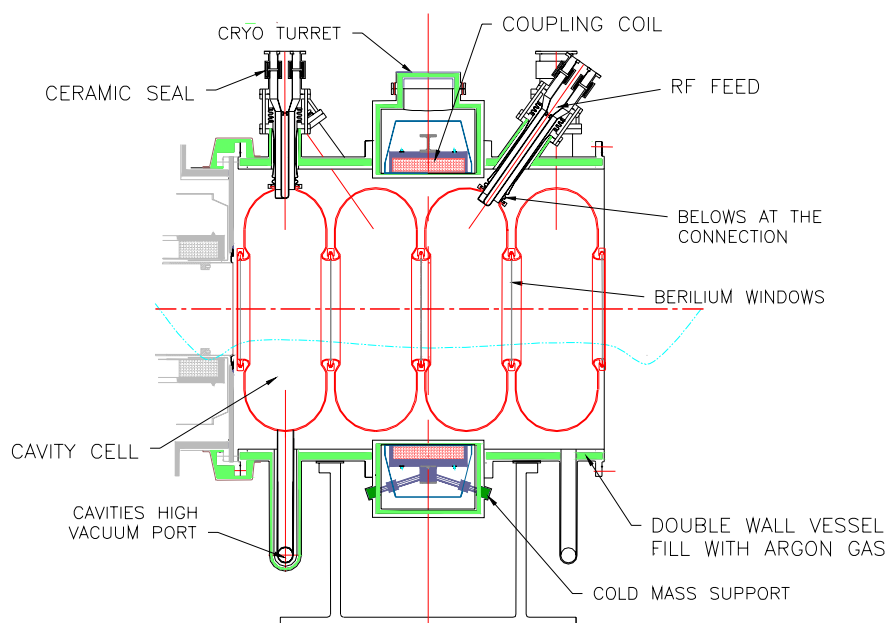


**Figure 10.15:** RF and coupling coil assembly cross-sectional view.

## 10.5 Costs and time-line of MICE installation at RAL

Cost estimates in k€ for the installation of infrastructure for MICE at RAL (not including the cost for the beam line itself) are summarized in Table 10.2; the estimates are based on a preliminary technical analysis. It should be noted that the cost of the MICE components themselves is not included in Table 10.2, which reflects only the infrastructure costs in support of the experiment. The relatively high cost of the cryogenics system is mainly due to the cost of the refrigerator, which is based on a commercial estimate for a 500 W machine. The time line estimated for accomplishing the tasks listed in Table 10.2 is presented in Figure 10.16. The longest task is the installation of the cryogenics system. This is mainly due to a 12–14 month delivery time for the refrigerator. Thus, the MICE infrastructure requires at least two years to be completed.

**Table 10.2:** Cost estimates for MICE installation at RAL (not including the beam line).

<b>Task</b>	<b>Cost (k€)</b>
Management activities	635
Civil engineering	945
Layout and services	1335
Detectors	75
Cryogenics system	2480
Hydrogen system	390
Superconducting magnets	240
RF system	50
Vacuum system	130
Controls	385
Total	6665
Contingency (30%)	2000
<b>Grand total</b>	<b>8665</b>

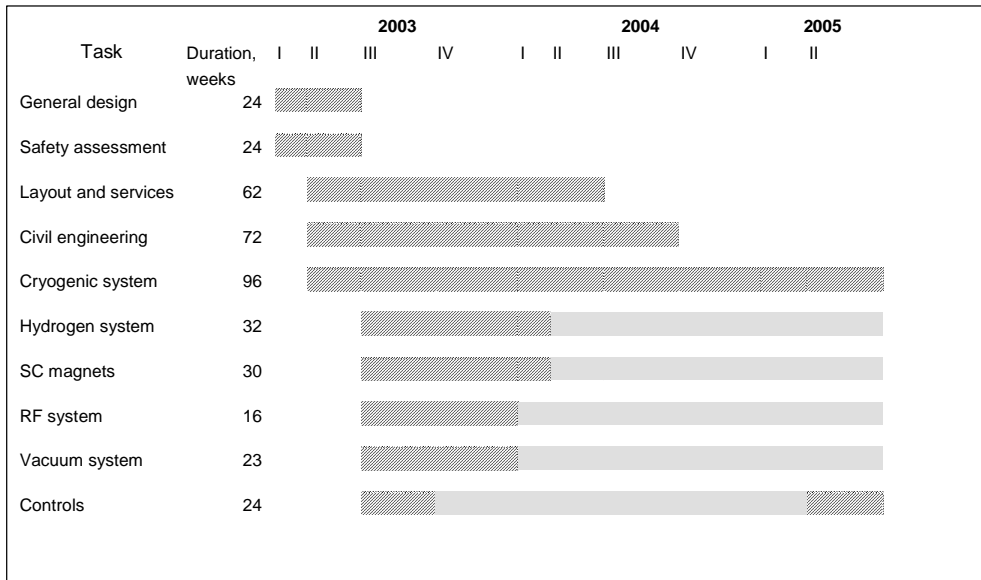


**Figure 10.16:** Time line for the installation of MICE infrastructure.

# 11 Summary of Responsibilities, Costs, Funding and Schedule

## 11.1 Cost

In this section, the expected costs for MICE are discussed. As the experiment is international, it is necessary to deal with the issues of different accounting rules and different currencies in the various participating countries. To do this in a straightforward way, only the base costs of the required hardware and the level of full-time staff years effort required to provide it for MICE are presented. It is assumed that it is the responsibility of the individual groups to propose to their respective funding agencies a budget that will deliver the hardware items required for MICE. This permits us to avoid dealing with such matters as contingency, escalation rates, and how to account for manpower. It also facilitates comparisons among the contributions from the various regions.

The cost estimates presented in this section are based on the assumption that all components must be provided new, and for the baseline tracker choice. As discussed in section 11.1.2, substantial cost savings, up to 24% of the cost of the experiment, could be envisaged if i) improved understanding of the RF dark current backgrounds allowed savings on the tracker, and ii) by refurbishing existing hardware. The realization of these cost savings would also lead to some redistribution of responsibilities within the collaboration.

To be conservative, we have listed in the tables the full base cost of the proposed MICE apparatus assuming it is constructed from scratch. As detailed in Section 11.1.2, there are substantial potential cost savings that may be realised by reusing existing components that may become available from other experiments, by borrowing equipment from participating institutions or by optimizing the apparatus design based on R&D now in progress.

Table 11.1 gives an overall summary of the estimated MICE hardware costs and effort; Tables 11.2–11.4 summarize the detailed hardware costs and effort for the experiment. For convenience, the costs are presented in k€, but the numbers can also be interpreted as k\$ since the euro and dollar are essentially equal at present. In broad terms, the cost estimate is broken down into three main categories: the Cooling Section (Table 11.2), which summarizes the costs for the magnets, RF cavities, liquid-hydrogen absorbers, and diagnostics; the Spectrometer Section (Table 11.3), which includes costs for the detectors and the solenoid spectrometer magnets; and Ancillary Items (Table 11.4), which includes cryogenics, data acquisition, vacuum, preparing a control room, and the like. The estimate for each item in Tables 11.2–11.4 was obtained from the responsible group, based on a careful look at the costs required to put the system in place at RAL.

For completeness, Table 11.5 summarizes the costs for the additional beam and infrastructure items that must be provided by RAL to make available a suitable beam for MICE. These expenditures, while necessary for MICE, are not included in the funding request for the experiment; that is, these costs do not appear in the total cost given in Table 11.1. Note that the cost given in Table 11.5 for the decay solenoid is for a new one, though it is likely that an existing solenoid can be borrowed from the PSI laboratory, giving substantial cost reduction.

### 11.1.1 Responsibilities

Tables 11.2–11.4 indicate the group or groups responsible for delivering the hardware. In the case of the US participants, a formal proposal has already been submitted to the National Science Foundation (NSF) and the Department of Energy (DOE). Thus, responsibilities have already been designated to individual laboratories and universities. In the case of the other regions, formal funding proposals have not yet been prepared. In most instances, the particular group responsible for a given hardware item is known, and is indicated in Tables 11.2–11.4. In other cases, particularly in the UK and Japan, the specific institutional assignments must await the funding decisions, and only the regional responsibility is indicated. Clearly the ability to fulfill these responsibilities is contingent on obtaining the required funding, so all assignments shown here are necessarily provisional until funding approval is granted.

**Table 11.1:** Overall hardware costs for MICE in M€ (or, equivalently, M\$) and effort levels in staff years. Funding assignments for the participating regions are indicated.

Item	Estimated cost					Effort [staff·yr]
	(M€)	US	Japan	Europe	UK	
Cooling section <sup>a</sup>	13.9	6.3	0.3	3.7	3.6	67
Spectrometer section <sup>b</sup>	7.5	2.1	0.7	3.0	1.7	48.5
Ancillary items <sup>c</sup>	3.8	0.1	0	0.5	3.2	60.5
Total	25.2	8.5 (34%)	1.0 (4%)	7.2 (29%)	8.5 (34%)	176

<sup>a</sup> See Table 11.2 for detailed breakdown.

<sup>b</sup> See Table 11.3 for detailed breakdown.

<sup>c</sup> See Table 11.4 for detailed breakdown.

**Table 11.2:** Hardware cost estimate for the MICE cooling section. Cost values are in k€ (or, equivalently, k\$) and effort levels in staff years.

Item	Responsible	Funding Source				Total	Effort [staff·yr]
		US	Japan	Europe	UK		
Cooling Section						13883	67
Magnets							
Focus coil pairs	UK				2491	2491	10
Coupling coils	LBNL	2560				2560	2.5
Power supplies	LBNL	135				135	0.5
Magnetic measurements	EU			100		100	0.5
RF System							
Cavities	LBNL	1686				1686	12.5
Windows	U-Miss.	855				855	2
Tuners	U-Miss.	259				259	8
Cryostat	IIT	96				96	2
System integration	IIT	235				235	5
Power distribution	UK				950	950	4
Power source + LLRF	EU			3500		3500	4
Absorbers							
Body (manifold)	Japan		349			349	3
Windows	U-Miss.	199				199	7
System integration	IIT/NIU/UK	40			17	57	2
Hydrogen safety <sup>a</sup>	UK	120		100	20	240	2
Diagnostics							
RF cavities	ANL/UK	22			22	44	0.5
Vacuum	EU			10		10	0.5
Cryogenics	NIU	117				117	1

<sup>a</sup> Paid for from 'common fund'.

**Table 11.3:** Hardware cost estimate for the MICE spectrometer section. Cost values are in k€ (or, equivalently, k\$) and effort levels in staff years.

Item	Responsible	Funding Source				Total	Effort [staff·yr]
		US	Japan	Europe	UK		
Spectrometer Section						7540	48.5
Magnets							
Spectrometers	Genoa			2200		2200	6
Power supplies	LBNL	280				280	0.5
Magnetic measurements	NIKHEF/Saclay			50		50	0.5
Detectors							
Tracker	U.S./UK/Japan/ INFN*/Geneva	1800	500	900	900	4100	19
Cherenkov	U-Miss./Louvain	150		100		250	10
Time-of-flight	Padova/Milan	10		300		310	7.5
Calorimeter	Rome III			350		350	5

\* Bari, Legnaro, Napoli, Trieste

**Table 11.4:** Hardware cost estimate for the MICE ancillary items. Cost values are in k€ (or, equivalently, k\$) and effort levels in staff years.

Item	Responsible	Funding Source				Total	Effort [staff·yr]
		US	Japan	Europe	UK		
Ancillary Items						3757	60.5
Cryogenics							
Cooling section	UK				2480	2480	1.5
Detector electronics	UK				200	200	0.5
Vacuum							
Pumps and valves	EU			127		127	0.9
Beam spoiler	UK				20	20	0.1
Supports and Stands							
Cooling section	UK				110	110	0.6
Spectrometer section	UK				50	50	0.4
Data Acquisition	Bari	7		263		270	5
Slow Controls	UK/EU			90	90	180	
Alignment	UK				50	50	0.5
Control Room	UK				120	120	1
Consumables <sup>a</sup>	UK				150	150	
Travel <sup>b</sup>		827	100	1000	480	2407	
Exp. Supp. & Analysis <sup>c</sup>							50

<sup>a</sup>Mainly cryogenic fluids and the like.

<sup>b</sup>Travel costs are not included in hardware total.

<sup>c</sup>Post-docs.

**Table 11.5:** Cost and effort estimate for additional beam and infrastructure items not included in the MICE funding request but necessary to carry out the experiment. All will be the responsibility of the UK.

Item	Hardware cost [k€]	Effort [staff·yr]
Management activities	16	4.2
Civil engineering	800	1.0
Beam line modifications		
Decommissioning old beam	160	0.3
New target	120	0.5
New beam components	840	1.7
Services	1270	0.4
Decay solenoid	2740	0.4
Total	5946	8.5

### 11.1.2 Possible cost savings

Section 11.1 presents the costs for the experiment based on the assumption that all components must be provided new. In that sense, this represents the full value of the components that will go into MICE. In a number of cases, however, there is a good likelihood that existing components can be refurbished or used as-is. Some of these potential savings require verification. Nonetheless, it is appropriate here to indicate the envisaged savings.

For the cooling section, several existing RF power sources located at CERN could be refurbished. If this were successful, the cost of the RF system would be reduced by about 2500 k€. In the spectrometer section there are a number of areas where cost savings may be possible. The Sci-fi tracker costs are based on the assumption that no multiplexing of the fibres will be done (for reasons of background tolerance). If the background simulations demonstrate that multiplexing is an acceptable alternative, it may be practical to reduce the cost of the system by as much as 3100 k€ (for 7:1 multiplexing). If the TPG tracker proves viable in the MICE environment, a similar saving would accrue. Possible savings by re-utilizing HARP electronics (after that experimental programme terminates) show up in several areas. In particular, the cost of the time-of-flight system could be reduced by 120 k€, the cost of the calorimeter by 150 k€, and the cost of the data acquisition system by 40 k€. In total, the cost for MICE summarized in Table 11.1 could decrease by as much as 5910 k€, or 24%.

If all cost savings were realised, the total hardware cost for MICE would be 19.2 M€. It is worth noting that the cost estimate of the Letter of Intent, made under similar assumptions, was 17.8 M€. It is encouraging to see that the cost estimate for the experiment has stayed nearly constant despite the additional technical understanding. Of the cost saving possibilities listed above, roughly half will happen with high likelihood. The main remaining uncertainty arises in the tracker costs, since the saving here is predicated on being able to handle the x-ray backgrounds with either a heavily multiplexed scintillating fibre tracker or with the less-expensive TPG. R&D to resolve this uncertainty is already under way, and a decision is planned, after careful external review of the progress, by the time of the collaboration meeting at the end of October 2003.

While it is not directly part of the MICE cost estimate, the decay solenoid for the muon beam line may be obtainable from PSI essentially for free. While there would still be costs associated with shipping, modifying, and installing the device, it is expected that the cost savings with respect to the estimate in Table 11.5 would be of order 2000 k€.

## 11.2 Schedule

A number of assumptions have been made in drawing up the overall schedule for MICE. In particular, it is assumed that sufficient funds to start work on the MICE beam and infrastructure in the hall at RAL will be available over UK financial years 2002/03 and 2003/04. In addition, to allow time to approach the appropriate funding agencies in each region, it is assumed that funding for the experiment itself will not start until six months after the experiment is approved. Given these assumptions, six milestones have been defined, corresponding to the six stages of the experiment described in Section 3. These are summarized in Table 11.6. Based upon this schedule, MICE as currently conceived will be completed in Q3 of 2007 and possible future extensions of MICE could commence in 2008.

**Table 11.6:** List of MICE milestones.

	<b>Milestone</b>	<b>Start date</b>
1	Characterization of muon beam	Q3 2004
2	Commissioning of first spectrometer	Q3 2005
3	Commissioning of both spectrometers	Q1 2006
4	Measurements with one absorber	Q2 2006
5	Measurements with two absorbers and one RF cavity	Q4 2006
6	Measurements with the full version of MICE	Q2 2007

The overall schedule for the construction and commissioning of MICE is shown in Figure 11.1. The most critical items in this schedule are i) the beam and the infrastructure at RAL and ii) the RF cavities for the experiment. Much of the work for the former can only take place during long shutdowns of the ISIS accelerator. The next such shutdown is currently scheduled for September 2003, and, to meet this, preparatory work has already started and must continue. Missing this shutdown would incur a substantial delay for the first three stages of MICE, as the next long shutdown will not be until the middle of 2005. Currently, only design work has been done on the 201 MHz RF cavities. About two years of R&D, including the construction of the first one-cell cavity, is required before production of the remaining seven can begin. This will be the longest-lead-time item in MICE.

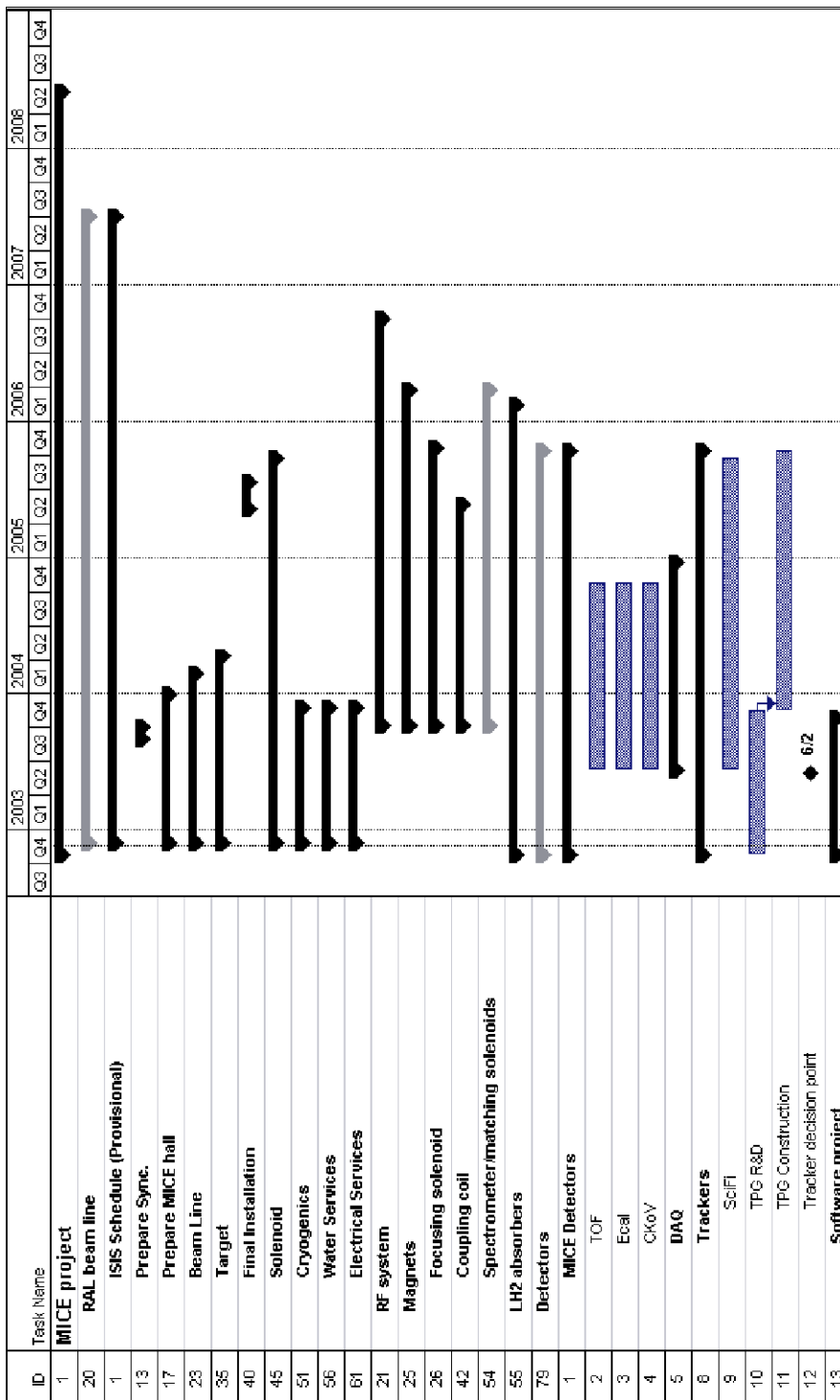


Figure 11.1: Summary of the construction schedule of MICE.

## 12 Summary and Conclusions

There is no doubt in the community that a Neutrino Factory would be a uniquely powerful facility. Not only would it be the ultimate tool for the study of the fascinating field of neutrino oscillations and leptonic CP violation, it would also offer opportunities for a large variety of smaller experiments for many years, while paving the way for future muon colliders. Detailed end-to-end studies have shown that indeed a Neutrino Factory could be built, but these remain largely paper simulations, leaving many to argue that the practical experience is lacking to ascertain the feasibility of a machine based on several new and untried concepts. Muon ionization cooling is probably the most striking of these new concepts, and it is of critical importance to the performance and cost of a Neutrino Factory.

The first challenge for MICE is thus to turn a new concept, which on paper *surely* works, into an apparatus that works *in practice*, supported by a community of experienced people capable of operating it, maintaining it and improving it. The next challenge is to do this in a significant way, from the combined points of view of precision, realism and relevance. The difficulty is quickly seen if one considers that a single cooling cell costs 5–10 M€ and provides 5% of transverse cooling, while the typical precision usually achieved on beam emittance measurements is of the order of 10%. (This problem cannot be avoided by reducing the size of the cooling cell, because only large beams are cooled.) Realism requires that the device be useable in a real Neutrino Factory design, and relevance requires that it address the issues that would influence the design, cost and reliability of the final accelerator complex; precision is important again here, since in a Neutrino Factory a muon beam would undergo a hundred or more of such cooling cells and imperfections would accumulate exponentially.

The MICE collaboration unites over 130 physicists from the world's accelerator and particle physics communities to tackle these challenges. Together, they have designed an experiment to demonstrate the feasibility of muon cooling and, with enthusiastic support from the UK particle physics community, shown that it can be carried out at Rutherford Appleton Laboratory. The MICE experiment uses a realistic cooling apparatus developed in the US Feasibility Study-II of a Muon-Based Neutrino Source, deployed between two precision muon spectrometers. By measuring the parameters of each muon individually, MICE will allow the  $\approx 10\%$  reduction in muon-beam transverse emittance (in each transverse plane) to be determined with an absolute precision of  $10^{-3}$ . The proposed two-cell cooling section will be operable with a variety of optical settings and absorber materials, allowing the cooling performance to be mapped out for a range of cooling-channel parameters and beam momenta and compared with the predictions of detailed simulations. By demonstrating that the technology of muon ionization cooling is not only technically feasible, but that its cost and performance are well understood, MICE will pave the way for the start of a Neutrino Factory construction project somewhere in the world during the next decade, and will point the way to muon colliders in the longer term.

Much has already been learned in the design process. In the MICE cooling section, the muon beam is ionization-cooled within liquid hydrogen absorbers, since this material largely outperforms any other as a cooling medium. These absorbers are enclosed by superconducting solenoids to provide focusing and interspersed with radio frequency accelerating cavities to replace the longitudinal momentum lost by the muons in the hydrogen. The proposed design for absorbers and their windows, supports and services reflects great attention paid to safety requirements. A redundant set of windows separates the absorber insulation vacuum from the

surrounding vacuum. Leakage of oxygen that might be cryo-pumped on cold surfaces is prevented by jacketing the exterior of the apparatus with a layer of argon gas at positive pressure.

The RF cavities are normal-conducting copper cavities operated at 201 MHz and closed electrically by a thin conducting layer at each end to obtain a high accelerating gradient at reasonable operating power. The MICE cooling section contains eight such cavities, in two groups of four separated by an absorber. Each four-cavity assembly is surrounded by a superconducting ‘coupling’ solenoid to provide the appropriate guide field within the cooling channel. Operating cavities at high gradient within a magnetic field is a non-trivial task and is the subject of ongoing study. The baseline design for the cavity closures is thin beryllium windows. Grids of gas-cooled thin-walled aluminium tubing could be cheaper and present less material to the beam, and are also under investigation.

The cavities are sources of electron dark currents and x-rays, via mechanisms that are critically sensitive to electric and magnetic fields. These mechanisms, and ways of suppressing them, are under intensive study. The electrons are stopped in the absorbers, and could cause excessive heating in a real Neutrino Factory design. For MICE itself, the resulting x-rays are penetrating and will cause background counts in the detectors of the spectrometers. These background rates have been measured in 2002 using 805 MHz cavities and detector prototypes; the extrapolation to MICE conditions seems well manageable being below 100 MHz per detector plane at the normally available RF power of 1 MW per RF cavity. Investigation of higher gradients might even be possible.

To allow precision measurement of transmission and emittance, one muon at a time will be tracked through the apparatus and detected using standard particle-physics techniques, which are much more precise than the detectors typically used in beam line instrumentation. A ‘virtual bunch’ formed in offline analysis will be used to demonstrate how an actual bunch would have behaved had the beam intensity been orders of magnitude higher.

The two spectrometers are composed of identical tracking devices placed inside superconducting solenoids providing a homogeneous magnetic field of 4 T. The baseline design for the tracking detectors is five sets of scintillating fibre planes per spectrometer, deployed in three stereo views, with the fibres individually read out using cryogenic VLPC photodetectors. An alternative design is also under investigation in which each spectrometer contains a time projection chamber with triple-GEM readout (TPG). Additional detectors will provide redundant particle identification to eliminate from the sample any residual pions in the incoming beam or muons that decay within the apparatus. These include time-of-flight scintillation counters, Cherenkov detectors and a calorimeter. While these are standard enough ingredients for particle-physics experiments, measuring an emittance ratio with  $10^{-3}$  precision has never been done and will require careful design of diagnostics and careful attention to system integration and calibration.

MICE will be housed in Building R5.2 at RAL and employ an upgraded muon beam produced using an internal target in the ISIS proton synchrotron. Two designs are under study for the beam line, one (the baseline) employing a 5 m superconducting solenoid and the other a set of quadrupoles. The solenoid design is much to be preferred. It gives a very clean beam and a high beam rate of about 3000 muons at 200 MeV/c per 1 ms burst. Given a 1 Hz repetition rate (to meet the duty factor requirement of the 201 MHz RF power supplies), a  $10^{-3}$  measurement of emittance, which will require a few  $\times 10^6$  muons in total, will thus

require about an hour of beam time. With the planned programme of studies at a variety of muon momenta and cooling-section settings, as well as the need for extensive systematic studies, the actual need for beam time will exceed this by two to three orders of magnitude. With the quadrupole-focused beam line the time per data point would be 10 times longer, putting greater demands on stability of the apparatus and limiting the possibilities of the experiment. The impact of the internal target on the rest of the ISIS programme is expected to be minimal.

MICE will reside at RAL for about five years and will proceed, starting with the beam line upgrade work, through several experimental stages. The gradual build-up of the MICE apparatus is mainly funding-driven, but has the useful consequence that it will lead to a valuable series of systematic studies being completed before the actual emittance reduction measurement commences.

Technical needs from RAL include the upgraded beam line, experimental hall, cryogenic refrigeration, water cooling, electrical power, conventional and radiation safety systems and oversight, RF power supply components, and engineering and technical support. These have been detailed in their respective sections of this proposal.

The proposed schedule for the commissioning and operation of MICE will establish the technical feasibility of muon ionization cooling by 2007; we are seeking funding from agencies around the world to allow this schedule to be achieved. By that year, the next generation of long-baseline experiments (CNGS and JPARC-SK) – sensitive to the ‘missing link’ in neutrino oscillations,  $\theta_{13}$  – will be starting up, and the LHC construction should have been completed. As the nations of the world then contemplate what the *next* big steps should be in high energy physics and in long-baseline neutrino studies, it will be crucial that the new technologies required for a stored-muon-beam Neutrino Factory have been demonstrated and the expertise built up. The path will then be clear to proceed with Neutrino Factory detailed design and construction. The recent results from SNO and KamLAND establishing the large mixing angle neutrino oscillation scenario confirm the likely ability of the Neutrino Factory to make ground-breaking measurements of leptonic CP violation. The proposed MICE programme is thus a timely and crucial step towards this exciting physics programme, which will probe the processes that occurred shortly after the Big Bang and led to the matter-filled Universe we observe today.

## References

- [88-vs-201] While 44 or 88-MHz cavities have certain advantages, compared to 201-MHz cavities they occupy a larger volume, provide less gradient, and require more power. Moreover, while 201-MHz power-supply components are available from CERN, 44- or 88-MHz supplies would need to be newly purchased or fabricated.
- [Adi02] M. Adinolfi et al. (KLOE Collaboration), Nucl. Instrum. Meth. A 478 (2002) 138
- [Adinolfi] M. Adinolfi et al., Nucl. Instrum. Meth. A482 (2002) 364
- [Albright00] C. Albright et al., *Physics at a Neutrino Factory*, Fermilab-FN-692, May 10, 2000, <http://arXiv.org/ps/hep-ex/0008064>
- [Aleksa02] M. Aleksa et al, Beam Dynamics Study of a Muon Ionization Cooling Experiment, Neutrino Factory Note 108 (2002), <http://nicewww.cern.ch/~molat/neutrino/nf108.pdf>
- [Alt02] C. Altunbas et al., Nucl. Instrum. Meth. A 490 (2002) 177
- [Anken99] C. Ankenbrandt et al., Phys. Rev. ST Accel. Beams **2**, 081001 (1999).
- [Antonelli] Antonelli et al., Nucl. Instrum. Meth. A354 (1995) 352
- [Apollonio02] M. Apollonio et al, *Oscillation Physics with a Neutrino Factory*, hep-ph/0210192 October 2002 (ed. M. Campanelli) <http://arXiv.org/ps/hep-ph/0210192>
- [Aprili02] P. Aprili et al., ICARUS Coll., CERN-SPSC-2002-027, CERN-SPSC-P-323, Aug 2002.
- [ASME80] 'ASME Boiler and Pressure Vessel Code', ANSI/ASME BPV-VIII-1 (American Society of Mechanical Engineers, New York, 1980), part UG-32.
- [ATEX Web-site] <http://europa.eu.int/comm/enterprise/atex/>
- [Aut99] B. Autin, A. Blondel and J. Ellis eds, CERN yellow report CERN 99-02, ECFA 99-197
- [Aysto01] J. Aysto et al: Physics with Low-Energy Muons at a Neutrino Factory Complex, hep-ph/0109217
- [Bac02] S. Bachmann et al., Nucl. Instrum. Meth. A 478 (2002) 104
- [Balbekov00] V. Balbekov et al., The Single Field Flip Cooling Channel for a Neutrino Factory, MUCOOL Note 125 (2000) and The Double Flip Cooling Channel (Study II version), MUCOOL Note 203 (2001), both available from <http://www-mucool.fnal.gov/notes/notes.html>
- [Ball00] R. D. Ball, D. A. Harris, K. S. McFarland, hep-ph/0009223.
- [Barger02] V. Barger, S. Geer, R. Raja, K. Whisnant, Phys. Rev. D63 (2001) 033002.
- [Bartlett] D. Bartlett et al., Nucl. Instrum. Meth. A260 (1987) 55.
- [BeamTools] V. D. Elvira, P. Lebrun, P. Spentzouris, <http://www-cpd.fnal.gov/geant4/G4BeamTools/>
- [BESS] BESS Collaboration, Nucl. Instrum. Meth. A455 (2000) 596; S. Geier et al., Proceedings of the 26th ICRC, Salt Lake City, 1999, 3, 117.
- [Blondel01] A. Blondel et al., hep-ph-0105297.
- [Blundell99] S. J. Blundell, Contemp. Phys. 40, 175 (1999).
- [Bre98] A. Bressan et al., Nucl. Instrum. Meth. A 423 (1998) 119
- [Bud69] G.I. Budker, in Proc. of the 7th Int. Conf. on High Energy Accelerators, Yerevan, 1969.
- [Borget02] J. Borget-Castell et al., hep-ph/0207080.
- [Cat02] G. Catanesi, Hit reconstruction, pattern identification and track measurements in the MICE-TPG, <http://gabri.home.cern.ch/gabri/MICE/>
- [Chevalier02] L. Chevalier, B0 Magnetic field measurement, Saclay Muon Software Group, internal report
- [Corlett2001] J. Corlett et al., in Proceedings of the 2001 Particle Accelerator Conference, Chicago, Editors P. Lucas, S. Webber (IEEE, Piscataway, NJ, 2001), p 500
- [Cox87] S. F. J. Cox, J. Phys. C20, 3187 (1987).
- [Cummings02] M. A. Cummings et al., 'Current LH<sub>2</sub>-Absorber R&D in MUCOOL', to appear in Proc. Nufact'02 Workshop.

- [D0] S. Abachi et al. 'The D0 Upgrade', Nucl. Instrum. and Meth., A408, pg. 103-109,1998; A. Bross et. al., 'Characterization and Performance of Visible Light Photon Counters (VLPCS) For The Upgraded D0 Detector at The FERMILAB Tevatron', Nucl. Instrum. and Meth., A477, pg. 172-178,2002.
- [Dalmas97] P. Dalmas de Reotier and A. Yaouanc, J. Phys. C9, 9113 (1997).
- [Donini02] A. Donini, D. Meloni and P. Migliozi, hep-ph/0206034.
- [EMCOG02] C. Wyss et al., <http://muonstoragerings.web.cern.ch/muonstoragerings/emcog/workingplan.doc>
- [Farinon02] S. Farinon and P. Fabbriatore, 'First Thoughts about the Design of the Spectrometer Solenoids for the MICE Experiment', a Power Point presentation by S. Farinon at the MICE workshop at LBNL, 23 to 25 October 2002
- [Fernow99] R. Fernow, 'ICOOL, A Simulation Code for Ionization Cooling of Muons Beams', Proc. 1999 Particle Accelerator Conference, A. Lucio and W. MacKay, eds. (IEEE, Piscataway, NJ, 1999), p. 3020.
- [Franchetti02] G. Franchetti et al., 'Muon phase rotation and cooling: simlution work at CERN], CERN/PS 2002-076(AP) CERN NUFACT Note 119 (2002) to appear in the proceedings of NUFACT02.
- [Fukuda98] Y. Fukuda *et al.* (SuperKamiokande Collab.), Phys. Lett. **B433**, 9 (1998); Phys. Lett. **B436**, 33 (1998); Phys. Rev. Lett. **81**, 1562 (1998); Phys. Rev. Lett. **82**, 2644 (1999)
- [Gas 02] U. Gastaldi, TPG, a cylindrical imaging gas detector with high transparency in the axial direction, INFN-LNL MICE-Legnaro Note01/02 May 2002, <http://proj-bdl-nice.web.cern.ch/proj-bdl-nice/cool/gastalditpgdraft.pdf> and <http://hep04.phys.iit.edu/cooldemo/gastaldi32002.pdf>
- [GDD 02] The CERN Gas Detector Development group page: <http://gdd.web.cern.ch/GDD>
- [Geant4] The Geant4 Tool Kit is available at <http://wwwinfo.cern.ch/asd/geant4/geant4.html>
- [Geer98] S. Geer, PRD 57, 6989 (1998)
- [Gorodetzky02] P. Gorodetzky et al., HELLAZ Coll., Nucl.Instrum.Meth.A471:131-135,2000.
- [Green00] M. A. Green, J. Y. Chen and S. T. Wang, 'The Design, and Construction of a Gradient Solenoid for the High Power RF Cavity Experiment for the Muon Collider', Institute of Physics Conference Series 167, p 1199, (2000),
- [Green02] M. A. Green and J. M. Rey, 'Superconducting Solenoids for an International Muon Cooling Experiment', to be published in IEEE Transactions on Applied Superconductivity 13, No. 2
- [Green02-1] M. A. Green, 'The Cryogenic Refrigeration System for MICE', LBNL Report LBNL-51751, November 2002
- [Gru02] The Study of a European Neutrino Factory Complex, P. Gruber ed., Neutrino Factory Note 103(2002) CERN/PS/2002-080(PP) [http://tilde-pgruber.home.cern.ch/~pgruber/docs/nf\\_report/nf\\_report\\_draft4.doc](http://tilde-pgruber.home.cern.ch/~pgruber/docs/nf_report/nf_report_draft4.doc)
- [Guler01] M. Guler et al., OPERA Coll., CERN-SPSC-2001-025, CERN-SPSC-M-668, LNGS-EXP-30-2001-ADD-1, Aug 2001.
- [Hanke00] K. Hanke, *Muon Front-End without Cooling*, NuFact Note 59 (2000).
- [HAR02] [http://harp.web.cern.ch/harp/Classified/Sub\\_detectors/TPC/index.html](http://harp.web.cern.ch/harp/Classified/Sub_detectors/TPC/index.html)
- [HARPlaser] SYLP0 by Quanta Systems srl, Milano, Italy
- [HARPTOF] G. Barichello et al., 'The HARP TOF Wall Construction and Test', INFN/AE-02/02.
- [Hol03] E. B. Holzer: Figure of merit for muon cooling, CERN Nufact Note 111 (2003)
- [Hol03a] E. B. Holzer: Simulation of the 88MHz cooling experiment with ICOOL, CERN Nufact Note 124 (2003)
- [Janot01] P. Janot, Workshop on an International Muon Ionization Cooling Experiment, CERN, October 2001, <http://muonstoragerings.cern.ch/October01WS/oct01ws.html>
- [Japnufact] *A Feasibility Study of A Neutrino Factory in Japan*, Y. Kuno, ed., <http://www-prism.kek.jp/nufactj/index.html>
- [JPARC] Japan Proton Accelerator Research Complex J-PARC <http://jkj.tokai.jaeri.go.jp/>
- [KamLAND02] K. Eguchi et al., KamLAND Coll., *First Results from KamLAND: Evidence for Reactor Anti-Neutrino Disappearance*, submitted to Phys. Rev. Lett. (6 Dec. 2002).

- [Kaplan01] D. M. Kaplan, 'Introduction to Muon Cooling', in Proc. APS/DPF/DPB Summer Study on the Future of Particle Physics (Snowmass 2001), N. Graf, ed. (2002), physics/0109061.
- [Kaplan-NuFact01] D. M. Kaplan et al., 'Progress in Absorber R&D for Muon Cooling', to appear in Proc. 3rd International Workshop on Neutrino Factory based on Muon Storage Rings (NuFACT'01), Tsukuba, Japan, 24–30 May 2001, arXiv:physics/0108027.
- [Kaplan-PAC01] D. M. Kaplan et al., 'Progress in Absorber R&D 2: Windows', in Proc. 2001 Particle Accelerator Conference, P. Lucas and S. Webber, eds. (IEEE, Piscataway, NJ, 2001), p 3888 (arXiv:physics/0108028).
- [KLOE] The KLOE Collaboration, *The KLOE Detector Technical Proposal*, LNF-92/019 (1992)
- [Kubik02] D. Kubik et al., to be submitted to Nucl. Instrum. Meth.
- [Lang01] K. Lang et al., MINOS Coll., Nucl. Instrum. Meth. A461, 290 (2001).
- [Lap71] P. M. Lapostolle, IEEE Trans. Nucl. Sci. NS-18, No 3, 1101 (1971)
- [LASA] Acerbi et al., INFN/TC-92/23, October 1992, M. Bonesini et al., INFN/AE-94/14, May 1994
- [Laser] M. Bonesini et al., 'Construction of a Fast Laser-based Calibration System for the HARP TOF Counters Wall', INFN/AE-02/02.
- [Lasserre02] T. Lasserre et al, LENS Coll., Prog. Part. Nucl. Phys. 48, 231 (2002).
- [Lindner02] M. Lindner, *The physics potential of future long baseline neutrino oscillation experiments*, to appear in Neutrino Mass, Springer Tracts in Modern Physics, ed. G. Altarelli and K. Winter, hep-ph/0209083 (2002)
- [Lombardi01] A 40-80 MHz system for phase rotation and cooling, NUFAC Note 20 (2001), available from <http://molat.home.cern.ch/molat/neutrino/nfnotes.html>
- [Mangano01] M. L. Mangano et al., CERN-TH/2001-131 (hep-ph/0105155).
- [Meek78] J. M. Meek and J. D. Craggs, *Electrical Breakdown in Gases*, John Wiley & Sons, 1978, p. 557.
- [MICE01] MICE Letter of Intent to the Paul Scherrer Institute and Rutherford Appleton Laboratory, available from <http://hep04.phys.iit.edu/cooldemo/micepsiloi.pdf>
- [MICEreview02] Joint CLRC/PPARC Panel to Review the MICE Proposal (A. Astbury *et al.*), 'Report of The 1st Panel Meeting', 25 March 2002, available from <http://hep04.phys.iit.edu/cooldemo/micenotes/public/doc/MICE0002/MICE0002.doc>
- [MICEweb] See the MICE web site <http://hep04.phys.iit.edu/cooldemo>
- [Mikhail01] Mikhail, E. M., Bethel, J. S., and McGlone, J. C., 2001, *Introduction to Modern Photogrammetry*, New York, John Wiley & Sons, Inc.
- [MUCOOL98] MUCOOL expt. (Muon Ionization Cooling R&D), FNAL Proposal P904 [http://www.fnal.gov/projects/muon\\_collider/cool/cool.html](http://www.fnal.gov/projects/muon_collider/cool/cool.html)
- [Murayama02] H. Murayama, Int. J. Mod. Phys. A17, 3403 (2002).
- [MUTAC01] H. Edwards et al., [http://www.cap.bnl.gov/mumu/polit/Mutac\\_Report\\_2001.pdf](http://www.cap.bnl.gov/mumu/polit/Mutac_Report_2001.pdf).
- [NA49] NA49 Collaboration, Nucl. Instrum. Meth. A430 (1999) 210; Nucl. Instrum. Meth. A451 (2000) 406; NA52 Collaboration, Nucl. Phys. A 590 (1995) 347C; PAMELA Collaboration, 27th International Cosmic Rays Conference, OG
- [Neuffer83] D. Neuffer, Part. Acc. **14**, 75 (1983);
- [Neuffer87] D. Neuffer, in *Advanced Accelerator Concepts*, F. E. Mills, ed., AIP Conf. Proc. 156 (American Institute of Physics, New York, 1987), p. 201; R. C. Fernow, J. C. Gallardo, Phys. Rev. E 52, 1039 (1995).
- [Neuffer99] D. Neuffer, 'mu+ mu- Colliders', CERN Yellow Report 99-12 (1999).
- [Nor01] J. Norem, A. Moretti and M. Popovic, Nucl. Instr. and Meth in Phys. Res. A 472 (2001) 600
- [Nor02] J. Norem, V. Wu, A. Moretti, M. Popovic, Z. Qian, L. Ducas, Y. Torun, and N. Solomey, *Dark Current, Breakdown and B Field effects in a Multicell, 805 MHz Cavity*, Submitted to Phys. Rev. ST Accel. Beams, MUCOOL Note #235.

- [NuFactPhys] S. Geer, PRD 57, 6989 (1998); B. Autin, A. Blondel and J. Ellis eds, CERN yellow report CERN 99-02, ECFA 99-197; C. M. Ankenbrandt et al., Phys. Rev. ST Accel. Beams 2, 081001 (1999); A. Blondel et al., Nucl. Instrum. Methods Phys. Res., A 451 (2000) 102; C. Albright et al., FERMILAB-FN-692, hep-ex/0008064; D. Harris et al., Snowmass 2001 Summary, hep-ph/0111030; A. Cervera et al., Nucl. Phys. B579, 17 (2000), Erratum-ibid.B593:731-732,2001; M. Koike and J. Sato, Phys. Rev. D62 (2000) 073006.
- [NUMIOffAxis] <http://www-off-axis.fnal.gov/loi.ps>, *Letter of intent to build an off-axis detector to study  $\nu_{\mu} \rightarrow \nu_e$  oscillations with the NuMI neutrino beam*, August 2002.
- [Palmer02] See e.g. R. B. Palmer, 'Ring Coolers: Status and prospects', presented at NuFact '02 Workshop, London, England, 1-6 July 2002, available from [http://www.hep.ph.ic.ac.uk/NuFact02/Scientific-programme/files/Friday/plenary/A09\\_palmer.ps](http://www.hep.ph.ic.ac.uk/NuFact02/Scientific-programme/files/Friday/plenary/A09_palmer.ps)
- [Palmer02-2] R. B. Palmer, and R. Fernow, '200 MHz Cooling Experiment Design Version 5', MICE Note 18, November 20, 2002, available from <http://hep04.phys.iit.edu/cooldemo/notes/notes.html>.
- [PATH] A. Perrin, PATH reference manual, unpublished.
- [PDG02] K. Hagiwara et al., *Review of Particle Properties*, Phys. Rev. D66, 010001 (2002), also available at <http://pdg.lbl.gov>
- [PED97] Pressure Equipment Directive 97/23/EC.
- [Pereved84] E. A. Perevedentsev, A. N. Skrinsky, Proc. 12th Int. Conf. on High Energy Accelerators, F. T. Cole, R. Donaldson, eds. (Fermilab, 1984), p. 485.
- [Pilaftsis99] A. Pilaftsis, Int. J. Mod. Phys. **A14**, (1999)
- [Poiss] Reference Manual for the POISSON/SUPERFISH Codes, report LA-UR-87-115.
- [POL] <http://village.flashnet.it/users/polhitec/index.htm>
- [Prael89] Richard E. Prael and Henry Lichtenstein, 'User Guide to LCS: The LAHET Code System', Los alamos National Laboratory report LA-UR-89-3014, Revised (September 15, 1989).
- [PSI] Design of the PSI muon beam lines with solenoid decay channel are described in <http://www.psi.ch>
- [Rad02] E. Radicioni, TPG readout, <http://proj-bdl-nice.web.cern.ch/proj-bdl-nice/cool/tpgemiliomarch2002.pdf>
- [RALHSN20] RAL Health and Safety Notice No. 20, Protection Against Ionizing Radiation.
- [RALHSN8] RAL Health and Safety Notice No. 8, New Regulations on Pressure Systems and Transportable Gas Containers.
- [RALHSN9] RAL Health and Safety Notice No. 9, The Biological Effects of Magnetic Fields.
- [RALSC1] Rutherford Appleton Laboratory safety Code No. 1, Hydrogen and Deuterium.
- [RALSC6] Rutherford Appleton Laboratory safety Code No. 6, Precautions to Avoid Ignition of Flammable Gases by Static Electricity.
- [RIKEN] The RIKEN-RAL pulsed muon facility, T. Matsuzaki, K. Ishida, K. Nagamine, I. Watanabe, G. H. Eaton, W. G. Williams, Nucl. Instrum. Meth. A465, 65 (2001).
- [Ruj99] A. De Rujula, M.B. Gavela, P. Hernandez, Nucl. Phys. B547 (1999) 21, arXiv: hep-ph/9811390.
- [Sanders] D. Sanders et al., IEEE Trans. Nucl. Sci. **49** (2002) 1834.
- [Sau01] F. Sauli, Nucl. Instrum. Meth. A461 (2001) 47
- [Sau97] F. Sauli, Nucl. Instrum. Meth. A 461 (1997) 531
- [SIREN] See <http://www.shef.ac.uk/uni/academic/N-Q/phys/research/pa/SIREN.html>.
- [Skrinsky81] A. N. Skrinsky, V. V. Parkhomchuk, Sov. J. Part. Nucl. 12, 223 (1981); D. Neuffer, Part. Acc. 14, 75 (1983); E. A. Perevedentsev, A. N. Skrinsky, in Proc. 12th Int. Conf. on High Energy Accelerators, F. T. Cole, R. Donaldson, eds. (Fermilab, 1984), p. 485.
- [Skrinsky81] A. N. Skrinsky, V. V. Parkhomchuk, Sov. J. Part. Nucl. **12**, 223 (1981)
- [SNO01] Q. R. Ahmad et al., SNO Coll, Phys. Rev. Lett. 87, 071301 (2001)
- [SNO02] Q. R. Ahmad et al., SNO Coll., nucl-ex/0204008.

- [Study I] *Feasibility Study on a Neutrino Source Based on a Muon Storage Ring*, D. Finley, N. Holtkamp, eds. (2000), [http://www.fnal.gov/projects/muon\\_collider/reports.html](http://www.fnal.gov/projects/muon_collider/reports.html)
- [Study II] 'Feasibility Study-II of a Muon-Based Neutrino Source', S. Ozaki, R. Palmer, M. Zisman, and J. Gallardo, eds. BNL-52623, June 2001, available at <http://www.cap.bnl.gov/mumu/studyii/FS2-report.html>.
- [Suda] R. Suda et al. (Belle), *Nucl. Instrum. Meth.* **A406** (1998) 213.
- [TBF] <http://www.lnf.infn.it/acceleratori/btf/>
- [TRIUMF] The TRIUMF muon beam lines, <http://musr.triumf.ca/equip/mubeamlines/node3.html>
- [Turner99] M. S. Turner et al., *Rev. Mod. Phys.* 71, S145 (1999)
- [Welford] W. T. Welford, R. Winston, *The optics of non-imaging concentrators*, Academic Press, New York, 1978, H. Hinterberger, R. Winston, *Rev. Sci. Instr.* 37 (1966) 1094
- [Work0001] Mini-Workshop on Beam Instrumentation, CERN, 13-14 July 2000; 2nd Workshop on Instrumentation for Muon Cooling Studies, IIT Chicago, Nov. 10-11, 2000; Workshop on Instrumentation for Muon Cooling Studies, Blackett Laboratory, Imperial College, 23-24 February 2001; Workshop on a Muon Ionization Cooling Experiment, 25-27 October 2001, CERN. Talks presented at these workshops can be accessed through the CERN muonstoragerings web page: <http://muonstoragerings.cern.ch>